Stony Brook University

Cellular Interactions with Tissue-engineered Microenvironments and Nanoparticles

A Dissertation Presented

by

Zhi Pan

to

The Graduate School

in Partial Fulfillment of the

Requirements

for the Degree of

Doctor of Philosophy

in

Materials Science and Engineering

Stony Brook University

August 2009

Stony Brook University

The Graduate School

Zhi Pan

We, the dissertation committee for the above candidate for the

Doctor of Philosophy degree,

hereby recommend acceptance of this dissertation.

Miriam H. Rafailovich, Ph.D., Advisor
Professor, Department of Materials Science and Engineering

Jonathan C. Sokolov, Ph.D.
Professor, Department of Materials Science and Engineering

Yizhi Meng, Ph.D.
Assistant Professor, Department of Materials Science and Engineering

Richard A.F. Clark, M.D.
Professor, Department of Biomedical Engineering

This dissertation is accepted by the Graduate School.

Lawrence Martin
Dean of the Graduate School

Abstract of the Dissertation

Cellular Interactions with Tissue-engineered Microenvironments and Nanoparticles

by

Zhi Pan

Doctor of Philosophy

in

Materials Science and Engineering

Stony Brook University

2009

Tissue-engineered hydrogels composed of intermolecularlly crosslinked hyaluronan (HA-DTPH) and fibronectin functional domains (FNfds) were applied as a physiological relevant ECM mimic with controlled mechanical and biochemical properties. Cellular interactions with this tissue-engineered environment, especially physical interactions (cellular traction forces), were quantitatively measured by using the digital image speckle correlation (DISC) technique and finite element method (FEM). By correlating with other cell functions such as cell morphology and migration, a comprehensive structure-function relationship between cells and their environments was identified. Furthermore, spatiotemporal redistribution of cellular traction stresses was time-lapse measured during cell migration to better understand the dynamics of cell mobility. The results suggest that the reinforcement of the

traction stresses around the nucleus, as well as the relaxation of nuclear deformation, are critical steps during cell migration, serving as a speed regulator, which must be considered in any dynamic molecular reconstruction model of tissue cell migration. Besides single cell migration, *en masse* cell migration was studied by using agarose droplet migration assay. Cell density was demonstrated to be another important parameter to influence cell behaviors besides substrate properties. Findings from these studies will provide fundamental design criteria to develop novel and effective tissue-engineered constructs.

Cellular interactions with rutile and anatase TiO_2 nanoparticles were also studied. These particles can penetrate easily through the cell membrane and impair cell function, with the latter being more damaging. The exposure to nanoparticles was found to decrease cell area, cell proliferation, motility, and contractility. To prevent this, a dense grafted polymer brush coating was applied onto the nanoparticle surface. These modified nanoparticles failed to adhere to and penetrate through the cell membrane. As a consequence, the coating effectively decreased reactive oxygen species (ROS) formation and protected the cells. Considering the broad applications of these nanoparticles in personal health care products, the functionalized polymer coating will likely play an important role in protecting cells and tissue from damage.

Dedicated to my family

for their love and support

Table of Content

List of Figures

List of Abbreviations

AHDF	Adult human dermal fibroblast
BSA	Bovine serum albumin
C	Cell binding domain or $FNIII_{8-11}$
DMEM	Dulbecco's modified eagle's medium
DIC	Differential interference contrast
DISC	Digital image speckle correlation
ECM	Extracellular matrix
FEM	Finite element method
FN	Fibronectin
FNIII	Type III repeats of FN
FNfds	Fibronectin functional domains
FNfd-SH	Cysteine-tagged fibronectin functional domains
G'	Shear storage modulus
H	Heparin binding domain or $FNIII_{12-15}$
HA	Hyaluronan
HA-DTPH	Thiol-functionalized hyaluronan
HLDS	High ligand density surface
HV	Heparin binding and variably spliced domains in one contiguous piece or $FNIII_{12-v15}$
LLDS	Low ligand density surface

PDGF	Platelet derived growth factor
PEGDA	Poly(ethylene)glycol diacrylate
RGD	Arginine-Glycine-Asparatic
ROS	Reactive oxygen species
SDS-PAGE	Polyacrylamide gel electrophorsis
SF-DMEM	Serum-free dulbecco's modified eagle's medium
UV	Ultraviolet
V	Variably spliced domain or FN_{IIICS}

Acknowledgements

This dissertation would not have been possible without the support of many people. I would like to acknowledge all those who have helped me during my doctoral study and research, beginning with my advisor, Professor Miriam Rafailovich. She is always full of energy and amazing ideas. I especially thank her for continually encouraging me to explore the physics behind biological phenomena. I would also like to thank Dr. Richard Clark who has not only been an enthusiastic collaborator but also a great co-mentor. It is him who led me into a fantastic world of tissue engineering with all the passion and motivated me to pursue a promising research career. I always feel so lucky to work on their collaboration projects and be supervised by both of them. Many thanks to them for their patience and trust in me and the enjoyable research experience in both groups.

I would like to thank my fantastic collaborators, Dr. Kaustabh Ghosh and Dr. Yajie Liu. Without their professional work and enthusiastic help, I can not finish my projects and get my results published. I also want to thank Professor Glenn Prestwich, Dr. Xiao Zheng Shu, and Dr. Wilson Lee for providing the materials (HA-DTPH and TiO_2 nanoparticles) for my research.

I am very grateful to Professor Jonathan Sokolov and Professor Yizhi Meng for serving on my dissertation committee and their constructive comments and persistent

attention on my research.

I would like to thank all my laboratory members and colleagues for their constant help with daily activities. My special thanks go to Dr. Fubao Lin, Dr. E Guan, Dr. Shouren Ge, Dr. Bingquan Li, Ms. Lourdes Collazo and Dr. Jim Quinn for their best technical training and support. I appreciate the co-working with Ying Liu, Lauren Macri, Lenny Slutsky, Chien-Hsu Lin and Divya Bhatnagar, and the discussion with Dr. Xiaohua Fang, Dr. Yantian Wang, Dr. Yuan Sun, Dr. Yuan Ji, Dr. Mayu Si, Dr. Chunhua Li, Dr. Jaseung Koo, Seongchan Pack, Xiaolan Ba, Chungchueh Chang and Jason Yang. Thank everyone in Garcia Center, including my high school students in the summer program and Mr. Allen Sachs, for giving me memorable five years at Stony Brook.

Finally, I would like to express my deepest gratitude to my family and my best friends at Stony Brook. I thank my Mom and Dad for their endless love, my parents-in-law for their understanding and self-giving help, my husband Zhenguo Wang for always being supportive, and my son Leo who is the best gift I have ever gotten in my life. I love you all so much that I will do my best to let you be proud of me. Sincere thanks go to Wei Zhang, Qing Jie, Meng Qu, Bob and Jeanette Scully. Your friendship will be my lifetime precious.

Chapter 1

Introduction

1.1 Background

The development of tissue engineering is highly dependent on the technologies to construct novel and effective extracellular matrix (ECM)-mimicking scaffolds (1-3), which can reproduce the chemical and physical environment of cells and provide the support or even control of cell functions. During the last several decades, various artificial scaffolds have been engineered with different structures from porous sponge to nano-fibers by using different natural or synthetic polymeric biomaterials (4-11). Many questions and topics have been addressed regarding their biocompatibility and their ability to support certain cell functions, such as cell growth and proliferation. Among these topics, one is of particular interest due to its fundamental importance: how cells interact with their microenvironments and how these interactions in turn regulate cell functions.

Cells explore and adapt to their environments in a feedback loop though focal adhesions (12). These adhesion sites serve as a micromechanical sensor which is sensitive to mechanical stimuli (13-15) as well as a bidirectional signal transmitter in response to biochemical stimuli (16, 17). Therefore, not only the ligand-induced biochemical properties but also the mechanics of the substrate can modulate tissue cell phenotype and functions in a physiological environment (18). Current studies

even show that tissue cells have type-specific response to the stiffness of substrates due to their distinct environments in real tissue (19), and substrate stiffness can induce stem cell differentiation by itself (20).

Complicated chemical-mechanical signal transductions occur in these interactions (21-23). A critical step is that cells transmit myosin-based contractile forces to substrates through adhesion sites and induce different mechanical responses through cytoskeleton rearrangement (24-26). These physical interactions at the cell-substrate interface, termed cellular traction forces, in turn regulate many cell behaviors, such as how strong cells adhere, how cells spread, and where and how fast cells migrate (21, 25, 27). Therefore, the measurement of cellular traction forces provides a meaningful evaluation of the interaction between cells and their environment.

So far, different approaches have been applied to estimate the cellular traction forces. Numerous quantitative assays employing a controlled detachment force, such as hydrodynamic fluid flow (28, 29) and micromanipulation (30-32), have been used to evaluate the overall adhesion strength of a cell on a substrate. Meanwhile, the receptor/ligand interactions at the molecular level have been explored by directly measurement using optical tweezers (33), micropipette (34) and atomic force microscopy (35, 36). However, none of them can provide both global and local information. In order to obtain a more comprehensive understanding of how traction forces are related to cell function, it is desirable to directly measure and calculate the quantitative distribution of traction forces applied through individual adhesion sites beneath the entire surface of whole living cells in real time (37).

Although it is difficult to directly measure cellular traction forces, the substrate exerts an equal and opposite force on the cell via the same adhesion sites, which enlightens people to study the cellular traction forces though the analysis of the substrate deformation generated by the adhesion of cells. Harris et al. (38) first qualitatively visualized cellular traction forces as visible wrinkles on a deformable silicone substrate. Later, using fluorescent beads to track local deformation, Dembo et al. achieved quantitative analysis of cellular traction forces on elastic substrate (39, 40). Using linear elasticity theory for thin elastic films and numerical algorithms for solving inverse problems, the forces exerted by cells on flexible substrate can be reconstructed (41, 42). However, due to the complexity of the algorithms, only few groups have reported their results solved in either real space (DW method) (41) or Fourier space (Fourier transform traction cytometry: FTTC method) (43), but both of them were based on Fredolm convolution. They simulated the traction force fields which induce the same displacements as those from the experimental data. Such inverse solved problems are ill-posed and the accuracy of these methods is strongly dependent on the precision and spatial resolution of displacement measurement. A small error in the displacement measurement would generate large uncertainties in the simulated traction force field. Moreover, these approaches are very computation intensive and can only be implemented by super computers.

In this dissertation, a novel approach is developed to measure the traction forces using the technique of digital image speckle correlation (DISC) and finite element method (FEM) (44). DISC technique is applied to quantify the substrate deformation

generated by cell attachment with a high spatial resolution (45). And then, the traction stresses (force per area) exerted by the cell can be quantitatively determined based on the DISC results by using finite element method (FEM) in a simple linear elastic model. With known distribution of stress and strain, the mechanical work done by the cell can also be calculated as strain energy stored in the elastic substrate. Comparing with existing methods, this method straightforwardly calculates the stress field with complete displacement boundary conditions. It is independent of the perceived cell boundary and no Fourier transformation is needed. Especially, because the ill-posed Fredholm integral is avoided, which is traditionally involved in the calculation of traction forces from measured deformation in previous methods, both the stress field and the strain energy are calculated in a more precise manner and with a higher spatial resolution. Standard finite element software (ABAQUS) can be run on a regular PC workstation.

1.2 Summary

In the first part of this dissertation (Chapter 2 — Chapter 4), we employed a tissue-engineered hydrogels composed of intermolecularly crosslinked hyaluronan (HA-DTPH) and fibronectin functional domains (FNfds) (46) to study structure-function relationship between cells and their microenvironments. Because both HA and FN are important components of ECM for cell migration and tissue organization during tissue repair (47, 48), this hydrogel is an excellent agent for in

vivo applications, including promoting granulation tissue formation and speeding healing process in punched porcine wounds (46). Meanwhile, it provides an ideal system for in vitro studies at cell level because the mechanical and the biochemical properties of this hydrogel can be independently controlled by varying the crosslinking ratio and ligand (FNfds) type/bulk density respectively (44).

During the repair of acute and chronic cutaneous wounds, the healing process is always triggered by the migration of dermal fibroblasts into wound site (49). Adult human dermal fibroblasts (AHDFs) were used to investigate how tissue cells sense and respond to hydrogel properties in the present study. Specifically, cellular traction forces were evaluated as well as the mechanical work done by the cell with DISC technique and FEM on the flexible substrates (44). The former directly determine where and how fast cells migrate (21, 25, 50-52) and the latter is a quantitative evaluation of the strength of whole cell adhesion. Together they provide both local and global mechanical information to analyze the correlation between the cellular mechanical responses and consequent cell migration. And we achieved a comprehensive platform to study the mechanism of cell migration in a tissue-like environment.

In Chapter 2, we studied how cell migration is regulated by substrate mechanics and adhesiveness. With an appropriate stiffness to support the organization of normal cytoskeleton and generation of robust traction forces, we studied cell morphology, cell migration and cellular traction forces as a function of different ligand types and densities. The results indicated that although cellular traction forces increase

consistently with rising substrate stiffness or adhesiveness, the migration speed is more intricately linked with traction forces. Specifically, these findings quantitatively demonstrated that it is the traction "gradient" over the whole cell, rather than the absolute magnitude of traction forces or the strength of cell adhesion that directly determines migration speed.

It is well known that cell migration is a highly dynamic process under physiological conditions (23, 52). To better understand the precise dynamics of cell migration, we measured the time-lapse cellular traction stresses as well as nuclear translocation and distortion during cell migration on HA/FNfds substrates with optimized stiffness and controlled adhesiveness in Chapter 3. We found that the nuclear translocation occurred in pulses whose magnitude was larger on the low ligand density surfaces (LLDS) than on the high ligand density surfaces (HLDS). Large nuclear translocations only occurred on LLDS when the rear traction stresses completely relocated to a posterior nuclear location, while such relocation took much longer time on HLDS, probably due to the greater magnitude of traction stresses. Nuclear distortion was also observed as the traction stresses redistributed. Our results suggest that the reinforcement of the traction stresses around the nucleus, as well as the relaxation of nuclear deformation, are critical steps during cell migration, serving as a speed regulator, which must be considered in any dynamic molecular reconstruction model of tissue cell migration. A traction gradient foreshortening model was proposed to explain how the relocation of rear traction stresses leads to pulsed fibroblast migration.

During many key physiological processes such as embryonic development and wound repair, it is *en masse* cell behavior instead of single cells (47). In Chapter 4, e*n masse* cell migration was evaluated using agarose droplet migration assay and compared with single cell migration on HA/FNfds hydrogels. The results indicated that migrating cells respond differentially to substrate stiffness and adhesiveness depending on whether they move as unicellular or multicellular units, with the preferential phenotype being mediated greatly by the size and distribution of focal adhesions. We also measured the deformation generated by *en masse* migrating cells to investigate how *en masse* cells influence the behavior of neighboring cells by altering local substrate mechanics.

In the first part of the dissertation, we have investigated how cells (human dermal fibroblasts) functionally adapt to their microenvironment by altering their physical state (e.g. level of contractility/traction) at the whole-cell level, and how these interactions in turn regulate cell function, especially cell migration. The findings from these studies provide insights into the fundamental design criteria to develop novel and effective tissue-engineered constructs.

In the second part of this dissertation (Chapter 5), we investigated the effects of exposure of human dermal fibroblasts to rutile and anatase TiO_2 nanoparticles as a supplementary study on cell interaction with its inorganic environment. We found that these particles can penetrate easily through the cell membrane and impair cell function, with the latter being more damaging. The exposure to nanoparticles decreases cell area, cell proliferation, motility, and contractility. To prevent this, a

dense grafted polymer brush coating was applied onto the nanoparticle surface. These modified nanoparticles failed to adhere to and penetrate through the cell membrane. As a consequence, the coating effectively decreased reactive oxygen species (ROS) formation and protected the cells. Considering the broad applications of these nanoparticles in personal health care products, the functionalized polymer coating will likely play an important role in protecting cells and tissue from damage.

1.3 References

1. Langer, R., and J. P. Vacanti. 1993. Tissue Engineering. Science 260:920-926.
2. Freed, L. E., G. Vunjaknovakovic, R. J. Biron, D. B. Eagles, D. C. Lesnoy, S. K. Barlow, and R. Langer. 1994. Biodegradable Polymer Scaffolds for Tissue Engineering. Bio-Technology 12:689-693.
3. Rosso, F., A. Giordano, M. Barbarisi, and A. Barbarisi. 2004. From cell-ECM interactions to tissue engineering. J. Cell. Physiol. 199:174-180.
4. Hubbell, J. A. 1995. Biomaterials in Tissue Engineering. Bio-Technology 13:565-576.
5. Lee, K. Y., and D. J. Mooney. 2001. Hydrogels for tissue engineering. Chem. Rev. 101:1869-1879.
6. Yang, S. F., K. F. Leong, Z. H. Du, and C. K. Chua. 2001. The design of scaffolds for use in tissue engineering. Part 1. Traditional factors. Tissue Eng. 7:679-689.
7. Yang, S. F., K. F. Leong, Z. H. Du, and C. K. Chua. 2002. The design of scaffolds for use in tissue engineering. Part II. Rapid prototyping techniques. Tissue Eng. 8:1-11.
8. Drury, J. L., and D. J. Mooney. 2003. Hydrogels for tissue engineering: scaffold design variables and applications. Biomaterials 24:4337-4351.
9. Shin, H., S. Jo, and A. G. Mikos. 2003. Biomimetic materials for tissue engineering. Biomaterials 24:4353-4364.

10. Lutolf, M. P., and J. A. Hubbell. 2005. Synthetic biomaterials as instructive extracellular microenvironments for morphogenesis in tissue engineering. Nat. Biotechnol. 23:47-55.

11. Pham, Q. P., U. Sharma, and A. G. Mikos. 2006. Electrospinning of polymeric nanofibers for tissue engineering applications: A review. Tissue Eng. 12:1197-1211.

12. Discher, D. E., P. Janmey, and Y. L. Wang. 2005. Tissue cells feel and respond to the stiffness of their substrate. Science 310:1139-1143.

13. Pelham, R. J., and Y. L. Wang. 1997. Cell locomotion and focal adhesions are regulated by substrate flexibility. Proc. Natl. Acad. Sci. U. S. A. 94:13661.

14. Balaban, N. Q., U. S. Schwarz, D. Riveline, P. Goichberg, G. Tzur, I. Sabanay, D. Mahalu, S. Safran, A. Bershadsky, L. Addadi, and B. Geiger. 2001. Force and focal adhesion assembly: a close relationship studied using elastic micropatterned substrates. Nat. Cell Biol. 3:466-472.

15. Wang, N., J. P. Butler, and D. E. Ingber. 1993. Mechanotransduction across the Cell-Surface and through the Cytoskeleton. Science 260:1124-1127.

16. Couchman, J. R., and A. Woods. 1999. Syndecan-4 and integrins: combinatorial signaling in cell adhesion. J. Cell Sci. 112:3415-3420.

17. Woods, A., R. L. Longley, S. Tumova, and J. R. Couchman. 2000. Syndecan-4 binding to the high affinity heparin-binding domain of fibronectin drives focal adhesion formation in fibroblasts. Arch. Biochem. Biophys. 374:66-72.

18. Engler, A., L. Bacakova, C. Newman, A. Hategan, M. Griffin, and D. Discher.

2004. Substrate compliance versus ligand density in cell on gel responses. Biophys. J. 86:617-628.

19. Georges, P. C., and P. A. Janmey. 2005. Cell type-specific response to growth on soft materials. Journal of Applied Physiology 98:1547-1553.

20. Engler, A. J., S. Sen, H. L. Sweeney, and D. E. Discher. 2006. Matrix elasticity directs stem cell lineage specification. Cell 126:677-689.

21. Galbraith, C. G., and M. P. Sheetz. 1998. Forces on adhesive contacts affect cell function. Curr. Opin. Cell Biol. 10:566-571.

22. Choquet, D., D. P. Felsenfeld, and M. P. Sheetz. 1997. Extracellular matrix rigidity causes strengthening of integrin-cytoskeleton linkages. Cell 88:39.

23. Ridley, A. J., M. A. Schwartz, K. Burridge, R. A. Firtel, M. H. Ginsberg, G. Borisy, J. T. Parsons, and A. R. Horwitz. 2003. Cell migration: Integrating signals from front to back. Science 302:1704-1709.

24. Wehrle-Haller, B., and B. A. Imhof. 2003. Actin, microtubules and focal adhesion dynamics during cell migration. Int. J. Biochem. Cell Biol. 35:39-50.

25. Sheetz, M. P., D. P. Felsenfeld, and C. G. Galbraith. 1998. Cell migration: Regulation of force on extracellular-matrix-integrin complexes. Trends Cell Biol. 8:51-54.

26. Alenghat, F. J., and D. E. Ingber. 2002. Mechanotransduction: All Signals Point to Cytoskeleton, Matrix, and Integrins. Science's STKE 119:pe6.

27. Elson, E. L., S. F. Felder, P. Y. Jay, M. S. Kolodney, and C. Pasternak. 1999. Forces in cell locomotion. In Cell Behaviour: Control and Mechanism of

Motility. Portland Press Ltd, London. 299-314.

28. Truskey, G. A., and J. S. Pirone. 1990. The Effect of Fluid Shear-Stress Upon Cell-Adhesion to Fibronectin-Treated Surfaces. J. Biomed. Mater. Res. 24:1333-1353.

29. Garcia, A. J., P. Ducheyne, and D. Boettiger. 1997. Quantification of cell adhesion using a spinning disc device and application to surface-reactive materials. Biomaterials 18:1091-1098.

30. Berk, D., and E. Evans. 1991. Detachment of Agglutinin-Bonded Red-Blood-Cells .3. Mechanical Analysis for Large Contact Areas. Biophys. J. 59:861-872.

31. Evans, E., D. Berk, and A. Leung. 1991. Detachment of Agglutinin-Bonded Red-Blood-Cells .1. Forces to Rupture Molecular-Point Attachments. Biophys. J. 59:838-848.

32. Evans, E., D. Berk, A. Leung, and N. Mohandas. 1991. Detachment of Agglutinin-Bonded Red-Blood-Cells .2. Mechanical Energies to Separate Large Contact Areas. Biophys. J. 59:849-860.

33. Knight, A. E., C. Veigel, C. Chambers, and J. E. Molloy. 2001. Analysis of single-molecule mechanical recordings: application to acto-myosin interactions. Prog. Biophys. Mol. Biol. 77:45-72.

34. Chesla, S. E., P. Selvaraj, and C. Zhu. 1998. Measuring two-dimensional receptor-ligand binding kinetics by micropipette. Biophys. J. 75:1553-1572.

35. Willemsen, O. H., M. M. E. Snel, A. Cambi, J. Greve, B. G. De Grooth, and C.

G. Figdor. 2000. Biomolecular interactions measured by atomic force microscopy. Biophys. J. 79:3267-3281.

36. Yip, C. M. 2001. Atomic force microscopy of macromolecular interactions. Curr. Opin. Struct. Biol. 11:567-572.

37. Ingber, D. E. 2003. Mechanosensation through integrins: Cells act locally but think globally. Proc. Natl. Acad. Sci. U. S. A. 100:1472.

38. Harris, A. K., P. Wild, and D. Stopak. 1980. Silicone-rubber substrata - New wrinkle in the study of cell locomotion. Science 208:177-179.

39. Dembo, M., T. Oliver, A. Ishihara, and K. Jacobson. 1996. Imaging the traction stresses exerted by locomoting cells with the elastic substratum method. Biophys. J. 70:2008-2022.

40. Oliver, T., K. Jacobson, and M. Dembo. 1998. Design and use of substrata to measure traction forces exerted by cultured cells. In Molecular Motors and the Cytoskeleton, Pt B. 497-521.

41. Dembo, M., and Y. L. Wang. 1999. Stresses at the cell-to-substrate interface during locomotion of fibroblasts. Biophys. J. 76:2307.

42. Oliver, T., M. Dembo, and K. Jacobson. 1999. Separation of propulsive and adhesive traction stresses in locomoting keratocytes. J. Cell Biol. 145:589-604.

43. Butler, J. P., I. M. Tolic-Norrelykke, B. Fabry, and J. J. Fredberg. 2002. Traction fields, moments, and strain energy that cells exert on their surroundings. Am. J. Physiol.-Cell Physiol. 282:C595.

44. Ghosh, K., Z. Pan, E. Guan, S. R. Ge, Y. J. Liu, T. Nakamura, X. D. Ren, M. Rafailovich, and R. A. F. Clark. 2007. Cell adaptation to a physiologically relevant ECM mimic with different viscoelastic properties. Biomaterials 28:671-679.

45. Guan, E., S. Smilow, M. Rafailovich, and J. Sokolov. 2004. Determining the mechanical properties of rat skin with digital image speckle correlation. Dermatology 208:112-119.

46. Ghosh, K., X. D. Ren, X. Z. Shu, G. D. Prestwich, and R. A. F. Clark. 2006. Fibronectin functional domains coupled to hyaluronan stimulate adult human dermal fibroblast responses critical for wound healing. Tissue Eng. 12:601-613.

47. Clark, R. A. F. 1996. The Molecular and Celluar Biology of Wound Repair. Plenum Press, New York.

48. Clark, R. A. F., K. Ghosh, and M. G. Tonnesen. 2007. Tissue engineering for cutaneous wounds. J. Invest. Dermatol. 127:1018-1029.

49. Clark, R. A. F., F. B. Lin, D. Greiling, J. Q. An, and J. R. Couchman. 2004. Fibroblast invasive migration into fibronectin/fibrin gels requires a previously uncharacterized dermatan sulfate-CD44 proteoglycan. J. Invest. Dermatol. 122:266-277.

50. Mitchison, T. J., and L. P. Cramer. 1996. Actin-based cell motility and cell locomotion. Cell 84:371-379.

51. Geiger, B., and A. Bershadsky. 2001. Assembly and mechanosensory function

of focal contacts. Curr. Opin. Cell Biol. 13:584-592.

52. Lauffenburger, D. A., and A. F. Horwitz. 1996. Cell migration: A physically integrated molecular process. Cell 84:359-369.

Chapter 2

Cell migration regulated by substrate mechanics and adhesiveness

Preface

A portion of this chapter has been reproduced from:

*Ghosh, K., Z. Pan, E. Guan, S.R. Ge, Y. Liu, T. Nakamura, X.D. Ren, M. Rafailovich, and R.A.F. Clark. 2007. Cell adaptation to a physiologically relevant ECM mimic with different viscoelastic properties. Biomaterials 28: 671-679,

with permission from Elsevier.

Main body of this chapter is in preparation for submission as:

Pan, Z., K. Ghosh, Y. Liu, R.A.F. Clark, and M.H. Rafailovich. Cell migration regulated by the adhesiveness of a physiologically relevant ECM mimic.

Original contribution: Data for Figure 2.4 - 2.10

In collaboration: Data for Figure 2.1, 2.3

Adapted from manuscript*: Figure 2.2

2.1 Introduction

Cell migration plays an important role in many normal and pathological processes, such as embryonic development, tissue morphogenesis and regeneration, wound healing, and tumor metastasis. Cell-substrate adhesiveness can regulate cell migration by directly adjusting the interactions between cell surface receptors and extracellular matrix (ECM) molecules (1, 2). So far, several variables related to the strength of the adhesion between the cell and its surrounding environment have been implicated to be important regulators of cell migration speed, including the number and spatial organization of receptors, the concentration of ligands, and the receptor-ligand affinity (3). A biphasic correlation between migration speed and surface adhesiveness is well-known with convincing supports in both experiments (4) and theoretical model (5), where maximal cell migration is predicted to occur at intermediate cell-substrate adhesiveness. However, all these previous studies are based on protein coated glass coverslips and polystyrene cell culture dishes which have very different mechanical properties from in vivo conditions. Furthermore, cell lines or transfected cells are commonly used. Recent studies showed that substrate mechanics can also modulate tissue cell behaviors in a way similar to biochemical signals (6-8). Georges and Janmey even pointed out that tissue cells have type-specific responses to the stiffness of substrates due to their distinct environments in real tissue (9). Further, Ghosh et al. showed that primary tissue cells are more sensitive to binding sites than cell lines (10). For instance, RGD can support NIH 3T3 fibroblast attachment, spreading and proliferation, while it fails to induce the same functions of adult human dermal

fibroblasts (AHDFs). Therefore, to exactly identify the structure-function relationship between cells and their microenvironment for real applications in tissue engineering, primary tissue cells should be investigated on a more physiologically relevant elastic substrate which can best mimic in vivo conditions with both appropriate mechanical properties and optimized adhesiveness.

A tissue-engineered hydrogel was recently developed as an ideal ECM mimic, which is composed of PEGDA crosslinked hyaluronan (HA-DTPH) and fibronectin functional domains (FNfds) (10). Since both HA and FN are important components of ECM at times of cell migration and tissue organization during tissue repair (11, 12), this hydorgel is practical for in vivo applications. It has been applied to promote granulation tissue formation and speed healing in punched porcine wounds (10). Meanwhile, because the mechanical and the biochemical properties of this hydrogel can be independently controlled, respectively, as a function of the crosslinking ratio (defined as the molar ratio of thiols on HA-DTPH: acrylate groups on PEGDA) and ligand (FNfds) type/bulk density, it also provides an ideal system for in vitro studies at cell level (13).

Here, by changing the crosslinking ratio from 2:1 to 6:1 and 12:1, we obtained flexible substrates with three different stiffness (14) and investigated how the migration of AHDFs is regulated by the substrate stiffness. Then, fixing the crosslinking ratio at 2:1 where AHDFs can form normal cytoskeleton organization and generate robust traction forces, we also studied the effects of variables of ligand type/density on cell migration. Under each condition, cell migration speed was

time-lapse measured in one hour, and cellular traction forces and mechanical work done by the cell were evaluated by using digital image speckle correlation (DISC) technique and finite element method (FEM) (13) on the flexible substrates. The mechanism of cell migration was explored by identifying the correlation between cell migration and related cellular mechanical responses.

2.2 Materials and Methods

2.2.1 Purification of fibronectin functional domains

We constructed different cysteine-tagged recombinant human FNfds (denoted by FNfd-SH in general, and C-SH, H-SH in particular) as ligands tethered to hydrogel. A detailed protocol for the cloning and purification of the FNfds was recently published (15). Briefly, the FNfds were cloned in pETCH, a modified pCal-n vector (Stratagene, La Jolla, CA), which codes for a carboxyl-terminal six-histidine affinity tag followed by a cysteine. These FNfd-SH have three extra amino acids (MetGlySer) at the amino-terminus and nine extra (ThrSerHisHisHisHisHisHisCys) at the carboxyl-terminus. FNfd-SH expression was induced in the BL21DE3LysS strain of E. coli by the addition of 0.5 mM IPTG (Fisher Scientific, Fair Lawn, NJ) to the L-Broth (FisherBiotech, NJ) and affinity-purified using the Ni-NTA agarose (Qiagen, Valencia, CA) according to the manufacturer's protocol. The purity of these recombinant FNfd-SHs was verified by SDS-PAGE analysis. The synthetic CRGD (Cysteine-Arginine-Glycine-Aspartic Acid) peptide at >98% purity was purchased from SynPep Corp., Dublin, CA. After purification, the FNfd-SH were concentrated

and then conjugated with 4.5% (w/v) PEG-divinylsulfone (PEGDVS) (Nektar Therapeutics, Huntsville, AL) in 0.1N distilled phosphate-buffered saline (PBS) and prepared as 5:1000 (moles FNfd-SH: moles PEGDVS) stock solutions of PEGDVS-C, and PEGDVS-H, respectively.

2.2.2 Preparation of HA/FNfds substrates

HA/FNfd hydrogel susbstrate were synthesized as reported previously (10). Briefly, the PEGDVS-FNfds stock solutions were coupled to the crosslinker poly(ethylene glycol) diacrylate (PEGDA) (Nektar Therapeutics, Huntsville, AL) in PBS to form PEGDA-FNfd conjugates with different FNfd type and density. Then these conjugates were mixed with 1.25%(w/v) thiol-functionalized HA (HA-DTPH) in serum free-DMEM (SF-DMEM, Sigma, St. Louis, MO) at volume ratio of 1:4 to obtain HA/FNfd hydrogels that were seeded in 35-mm tissue culture dishes. Final concentration of HA-DTPH was always 1%(w/v) in the hydrogels. The stiffness of these hydrogels was modulated by altering the concentration of PEGDA solutions from 4.5% to 1.5% and 0.75% (w/v) which resulted in crosslinking ratio from 2:1 to 6:1 and 12:1 and shear storage moduli of 4270 Pa, 550 and 95 Pa, respectively, as measured by oscillatory shear rheometry (14). For the stiffness study, the adhesiveness was maintained constant by using all three FNfds, C/HV/H, required for optimal fibroblast migration at the optimal bulk density of 0.26 μM (16). Then for the the adhesiveness study, the stiffness was fixed at shear modulus G'= 4270 Pa by maintaining crosslinking ratio of 2:1, while the ligand type and bulk density were

varied. All substrates were stored at 4 ^{o}C for more than 18 hours to stabilize hydrogel crosslinking before cells were seeded on (14). Due to the requirement of substrate deformation measurement, fluorescent beads (40 nm diameter, Molecular Probes, Eugene, OR) were sonicated and suspended uniformly at a concentration of 5%(w/v) in HA solution prior to gelation, serving as trackers. The bead concentration was optimized to achieve a best density of speckles for the DISC technique, while at the same time remaining sufficiently dilute to prevent clustering.

2.2.3 Cell culture and seeding

Primary AHDFs obtained from a 31 year old Caucasian Female (Clonetics, San Diego, CA) were used between passages 5 and 13. The cells were routinely cultured in Dulbecco's Modified Eagle's Medium (DMEM), supplemented with 10% fetal bovine serum and 1% Penicillin, Streptomycin and L-glutamine, in a 37°C, 5% CO2, 95% humidity incubator (Napco Scientific Company, Tualatin, OR). Cells were seeded onto HA substrate in serum-free DMEM at low cell density (~500 /cm^2) to avoid cell-cell contact. Then all the samples were incubated at 37 °C for 6 hours prior to all measurement to maximize cell adhesion and spreading. Only single cells were chosen to measure migration speed and traction forces.

2.2.4 Measurement of cell area, aspect ratio and migration speed

Time-lapse phase images of the cells were recorded every 15 min for up to 60 min with a MetaMorph®-operated CoolSNAP™ HQ camera (Universal Imaging Corporation, Downingtown, PA) attached to a Nikon Diaphot-TMD inverted

microscope fitted with a 37 ^{o}C stage incubator and a 10x objective lens. Using MetaMorph software, aspect ratio of cells and projected cell area were obtained from phase images by measuring major and minor length of each cell or area covered by the outline of each cell, respectively. Migration speed was determined from the time-lapse images by tracking the distance covered by the center of a cell nucleus every 15 minutes over one hour. For these studies, n = 5~10 cells/field x 5 fields/replicate x 3 replicates.

2.2.5 Measurement of cellular traction forces and mechanical work done by the cell using DISC and FEM

Our novel technique of measuring cellular traction forces and mechanical work has been report recently (13). To track the surface deformations induced by cellular traction forces, 5% (v/v) fluorescent beads were pre-embedded in the substrate as described above. Digital images of the field of interest are taken before and after detaching cells from the substrate by the treatment with trypsin+EDTA. Using optimized DISC technique (17), the displacements of the substrate surface can be quantitatively determined by comparing the distribution change of the embedded beads. We then applied the surface displacements as the boundary conditions in our finite element model, a simple linear elastic model of 8-node 3 dimensional solid elements with known mechanical properties. In this model, cellular traction fields were calculated as the shear stresses on the substrate surface; the mechanical work done by the cell (W) was estimated by the strain energy (E)stored in the elastic substrate using the equation as below:

$$W = E = \frac{1}{2}\int \sigma_{ij}(\vec{r}) \cdot \varepsilon_{ij}(\vec{r}) dV \qquad i, j = 1, 3.$$

Phase contrast images of living cells and fluorescence images of embedded fluorescent beads in the substrate were recorded simultaneously with a differential interference contrast (DIC) lens and a 63x, aperture 0.9 water objective lens on a Leica TCS SP2 laser scanning confocal microscope (Leica microsystem Inc., Bannockburn, IL). Because optimal pinhole size was automatically chosen as optimal state, only the beads in this top narrow layer of the substrate were recorded. All images were recorded with a CCD camera with the same resolution of 1024x1024 in pixel.

2.2.6 Data analysis

The number of replicates for each experiment was adjusted according to the variance obtained. Data is expressed as mean $\pm$ standard error and evaluated for differences by ANOVA followed by Tukey post-hoc analysis. Differences were considered significant when $p < 0.05$.

2.3 Results and Discussion

2.3.1 Cell migration regulated by the substrate stiffness

Using the substrates with different stiffness, we first time-lapse imaged the migration of cells with 15 min intervals over an hour and found that the average speed of AHDF migration decreased noticeably with increasing substrate stiffness (Fig. 2.1). This result is consistent with a previous study where cells migrated slower on stiff

polyacrylamide substrates (6).

In order to understand this phenomenon, we measured and calculated distributions of cellular traction stresses on substrates with different stiffness. After AHDFs were seeded on substrates prepared as above but with 5% (v/v) fluorescent beads and incubated for 6 hours at 37 ^{o}C, digital images of the field of interest were taken before/after separating cells from the substrate by using trypsin+EDTA. DISC technique was used to compare the distribution of all beads between undeformed and deformed images and to produce a displacement map of the substrate surface as shown in Fig. 2.2(A), corresponding to the cell-induced deformation on substrates with different stiffness. Applying these displacement maps as surface boundary conditions in FEM, cellular traction fields were calculated as the shear stress maps on the substrate surface in Fig. 2.2(B). In these figures, arrows show the relative magnitude and the direction of displacement and traction vectors, and colors show the absolute magnitude of displacements and tractions with unit: μm and Pa, respectively. Superposed on these images are the outlines of cell boundaries and nuclei obtained from the phase contrast images of the same field recorded by DIC lens.

Results of cellular traction stresses show that cells are very sensitive to substrate stiffness. Since cells generate higher traction forces in larger area on stiffer substrates, stiffer substrates can support stronger cell adhesion evaluated by the mechanical work done by the cell as shown in Fig. 2.2(C). However, strong cell adhesion to some extent impairs cell migration probably due to the difficulty to detach the cell rear (18). We further explored this issue by the study of cell migration as a function of substrate

adhesiveness.

2.3.2 Cell migration regulated by the substrate adhesiveness

While others have transfected cell lines with integrin genes to manipulate the expression level of receptors on cell surface (4), we controlled cell-substrate interactions here only by substrate adhesiveness through altering affinity and number of receptor-ligand bindings. Specifically, binding affinity was controlled by using four different FN functional domains: the central cell-binding domain ($FN_{III8-11}$ or C), the major heparin-binding domain ($FN_{III12-15}$ or H), the variably spliced domain (FN_{IIICS} or V) and the heparin-binding domain including the variably spliced domain ($FN_{III12-V15}$ or HV) (Fig. 2.3). These FNfds can be functionally recognized by distinct receptors on fibroblast surface and form adhesive bindings with different affinities. Particularly, C includes the RGD sequence, a specific tripeptide sequence (Arg-Gly-Asp) which is a cell binding site for integrin α5β1 and αvβ3; H has binding sites for integrin α4β1, Syndecan-4 and CD44; and V has binding sites for integrin α4β1 and Syndecan-4. C, H and V are known to be the three major functional domains in fibronectin required for optimized fibroblast migration (16). However, so far, there is not uniform agreement on whether these domains work together or support cell adhesion and migration independently. The answer to this quandary is at least partially elucidated here by the comparison of cell adhesion and migration on substrates with C, HV, H and V.

2.3.2.1 Cellular responses to substrate adhesiveness as a function of ligand type

After AHDFs were seeded on the substrates at the same density (~500 cells/cm^2) with different FN functional domains as C, HV, H or V respectively at the same bulk density of 0.26 μM and incubated for 6 hours at 37 ^{o}C, direct observations using optical microscopy were performed. Cells appeared to attach well on the substrate with C or HV as the ligand, a few cells failed to attach onto the substrate with H as the ligand and were found floating in the media, and most of the cells were floating in the media on the substrate with V as the ligand. By staining the F-actin filaments using Alexa Fluor 488 Phalloidin (Molecular Probes), we found that the cells adhering on the substrate with C or HV domain had more stress fibers and spread better than those cells on substrate with H or V (Fig. 2.4). Detailed evaluation of cell spreading and polarity was provided by measuring cell area and aspect ratio as shown in Fig. 2.5(A) and (B). Cells spread better with larger cell area and show greater polarity on C and HV compared to H. Furthermore, cells migrate faster on C and HV than H at the density of 0.26 μM (Fig. 2.5(C)). No result of V was obtained at this density, since V domain was so weak that very few cells were attached and those that did failed to move. When these few cells tried to migrate over one hour observation period, most of them lost their attachment and became rounded.

Different cell morphology and migration implicated differential cellular traction forces induced by these FNfds. Thus, the distributions of cellular traction stresses on the substrate with different ligand types, C/HV/H respectively, were measured and shown in Fig. 2.6(A). Too few cells attached on the substrate to which V had been tethered therefore no result was obtained for V at this density.

Comparing the distributions of cellular traction stresses with related cell and nucleus boundaries, we found that on substrates with C or HV domain, well spreading cells generated maximum cellular tractions at about 10~20 μm behind leading edges. These findings are consistent with previous studies (19-21) and consonant with the idea that mature focal adhesions formed behind the leading edge apply strong rearward tractions to drive cell migration. By presenting the magnitude of cellular tractions in the third dimension, apparent traction gradients between the front and the rear of the cell were shown on substrates with C or HV domain rather than on those with H domain (Fig. 2.6(B)). This imbalance explained why these attached cells have different abilities to migrate. There is another interesting finding shown in these traction fields that all of these attached cells exert obvious tractions around the nuclei, which indicates that the generation of tractions around the nuclei is not only important for cell attachment as in the case of H but also during cell migration as in the case of C and HV. Actually, it is difficult for a migrating cell to resistant the traction gradients between the front and the rear and maintain instantaneous stable cell adhesion without these tractions around the nucleus. This issue will be further explored in Chapter 3.

As shown in Fig. 2.6(C), the mechanical work done by the cell on substrates with C or HV is significantly higher than that on substrates with H. Because the mechanical work done by the cell on the substrate evaluates the strength of cell adhesion at the whole cell level, this result demonstrated that both C and HV play a dominant role in cell adhesion, nether H and V domain can support strong cell adhesion at this density. Correlated with cell migration as shown in Fig. 2.5(C), it

shows that cell migration requires enough cell adhesion.

Briefly, at the density of 0.26 μM, cells can generate apparent traction gradients along its long axis and perform stronger adhesion as well as faster migration on high affinity FN domains such as C and HV than on low affinity domains as H and V. This observation implicated that: 1) both C and HV play a dominant role in cell adhesion and migration, which is consistent with the previous reports that they contribute to optimal adult human dermal fibroblast migration at this density (16) and C domain can support focal adhesion formation by itself (15); 2) H and V cooperate together in HV and neither can work alone, which experimentally supports the suggestion in previous report that V may regulate the activities of H (22).

2.3.2.2 Cellular responses to substrate adhesiveness as a function of ligand density

For each different ligand type, cellular mechanical responses and cell migration were studied as the function of ligand density. Increases in ligand density presumably provide more binding sites on the surface of substrates to form bindings with cells, resulting in rising cellular traction stresses and stronger cell adhesion. This was confirmed in our experiments, which showed that both the magnitude of cellular tractions and mechanical work done by the cell always increase as the density rises for each ligand type. However, cell morphology and migration on substrates with different ligand types showed unique correlations with ligand density.

In the case of C domain, which forms high affinity bindings with cell surface receptors, cell area did not significantly change as the bulk densities was increased

from 0.052 μM to 1.04 μM (Fig. 2.7(A)). However, the aspect ratio of cells decreased more than 35 % as the ligand density increased from 0.052 μM to 0.26 μM and then did not show much change as the ligand density was further increased (Fig. 2.7(B)). This trend is consistent with cell migration speed, which decreased from ~0.61 μm/min to ~0.28 μm/min along with stronger cell adhesion and also had a similar asymptotic plateau at high ligand densities (Fig. 2.7(C)). This predicted that: 1) C domain can support good cell adhesion and fast cell migration when the density is as low as 0.052 μM; 2) when the density increased, stronger cell adhesion impaired cell polarity and induced slower cell migration; 3) when the density increased up to a potential "saturation" point, cell migration speed dropped to a minimum as the cell-substrate adhesiveness (evaluated as mechanical work done by the cell) rose to its maximum, which is probably limited by receptor expression level on the cell surface.

These issues were quantitatively confirmed by the distribution of cellular traction stresses and the mechanical work done by the cell. Shear stress maps for C domain as a function of bulk density are shown as an example in Fig. 2.8(A). In this figure, the upper three are the traction fields on substrates with C domain at 0.26 μM, 0.52 μM and 1.04 μM on different scales where it is clear to see the maximum value of the tractions increases along with rising densities. By showing the same traction fields on one fixed scale as the bottom three, we also found that with rising densities, the traction stresses distributed in larger areas. All these implicated stronger cell adhesion with rising densities, which is illustrated in Fig. 2.8(B) where the mechanical work done by the cell is dose-dependent. Additionally, we also noticed that the mechanical

work curve is not a simple linear plot. As the exterior ligand density continued to increase, mechanical work done by the cell achieved a maximum value probably limited by the receptor expression level on cell surface. As previously shown by others (4, 18) and confirmed here, the strength of cell adhesion develops a negative correlation with cell migration on high adhesive surfaces.

Additionally, a second detailed examination of the tractions represented in a 3D manner (Fig. 2.8(C)) shows that the cell produced a clear traction gradient at a relative low density of C domain (0.26 μM). As the density of C domain rose, higher tractions were also generated at the cell rear or other directions which resulted in decreased traction gradients across the cell. Comparing these different mechanical responses with cell migration, it becomes clear that traction gradients across the cell are best correlated with cell migration.

Although cells exert stronger tractions in larger areas and generate higher strain energy as the ligand density rises, which is the same with every ligand type, we found that cell migration has differential function relationship with ligand density for different FN domains which is probably due to their different affinity to cell surface receptors. HV domain with comparable affinity as C domain at the same density shows similar results, while different from the situation of C domain, cell spreading, polarity and migration were all improved by the increasing density of H domain (Fig. 2.9).

Actually, the results in Fig. 2.10(A) presented that H domain is so weak that cells can not generate comparable cellular tractions on substrate with H as high as those on

substrate with HV until the bulk density of H increased to 1.04 μM which is four times of HV domain density at 0.26 μM. Due to its poor affinity, H domain needs more binding sites to support better cell adhesion and generate distinct traction gradients (Fig. 2.10(B)). The mechanical work done by the cell on H domain increased as ligand density increased from 0.26 μM to 1.04 μM (Fig. 2.10(C)), which is positive related to cell migration speed as shown in Fig. 2.9(C). The situation of V domain is worse due to its poorest affinity. AHDFs can not stably attach and migrate on HA substrate with only V domain even when tethered at a much higher density (2.60 μM).

All together, although the strength of cell adhesion is dose-dependent for each ligand type, cells migrate slower on substrates with more high affinity ligands such as C domain and do faster on substrates with more low affinity ligands such as H domain. This is consistent with the notion that high affinity receptors showed maximal migration at lower concentrations than low affinity receptors (4). Furthermore, a detailed examination of cellular traction distribution presented that when the density of C domain increased, cells began to generate high traction at the cell rear or other directions which actually decreased the traction gradient across the cell, while on substrate with H domain, increased ligand density provided more binding sites for the cell to generate higher traction behind the leading edge which resulted improved traction gradients. These findings experimentally proved the concept that detachment at cell rear can be predicted to limit cell migration speed in situation of high cell-substrate adhesiveness with attachment at the cell front limiting migration speed

in situation of low adhesiveness (18). We finally demonstrated the traction gradient across the cell a direct correlation with cell migration. This notion can also explain why cells can easily migrate across the boundary from the soft side to the stiff side of the substrate while they turn around or retracted as they reach the boundary from the stiff side (6). Because cells can generate much higher traction forces on stiff side which induce huge traction gradients over the boundary and guide cells migrate toward to the stiff side.

Although we did not gain a biphasic relationship between the adhesion strength and cell migration speed for each ligand type as previous literature (4), which probably due to different substrate and different cells used in the experiment, our results of low and high affinity ligands, H and C, together implicated the existence of such relationship. Because we used normal AHDFs in this study and no transfection was applied to control the expression level of receptors on cell surface. This reasonably resulted in a potential “saturation” point as the ligand density increases where both cell migration speed and mechanical work done by the cell close to an asymptotic value which is limited by the certain receptor expression level on the cell surface.

Because HV is composed of H and V, and it is known that both H and V have bonding sites for integrin α4β1, they are supposed to have similar adhesive mechanism. Another important finding covered within the results above is that cells can not generate comparable cell adhesion on substrates with neither H nor V alone even at a much higher density which ensures more binding sites for integrins as that

on substrates with HV. This means that H and V domain functionally cooperate together in HV to support robust cell adhesion and migration, which is consistent with previous reports that the H and V need to present at the same time for strong cell attachment (23) and V may regulate the activities of H in cell spreading (22).

2.4 Conclusion

Using a physiologically relevant ECM mimic with well controlled stiffness and adhesiveness, we show that cell migration can be regulated by both the mechanical and biochemical properties of the substrate. We also measured the related cellular traction forces under each condition. The results indicated that although cellular traction forces increase consistently with rising substrate stiffness or adhesiveness, the migration speed is more intricately linked with traction forces. Specifically, these findings demonstrated, in an explicitly quantitative manner, that it is the traction "gradient" over the whole cell, rather than the absolute magnitude of traction forces or the strength of cell adhesion that directly determines migration speed. Cell migration is improved whenever apparent traction gradients can be generated. Increasing the traction gradients of cells will be a clear criterion for any artificial tissue design aiming maximum cell migration.

We also showed that both C and HV domain play a dominant role in cell adhesion and migration. H and V domain functionally cooperate together in HV to generate robust cell adhesion and migration, and neither of them can support comparable cell functions alone.

2.5 References

1. Geiger, B., and A. Bershadsky. 2001. Assembly and mechanosensory function of focal contacts. Curr. Opin. Cell Biol. 13:584-592.
2. Schmidt, C. E., A. F. Horwitz, D. A. Lauffenburger, and M. P. Sheetz. 1993. Integrin cytoskeletal interactions in migrating fibroblasts are dynamic, asymmetric, and regulated. J. Cell Biol. 123:977-991.
3. Huttenlocher, A., M. H. Ginsberg, and A. F. Horwitz. 1996. Modulation of cell migration by integrin-mediated cytoskeletal linkages and ligand-binding affinity. J. Cell Biol. 134:1551-1562.
4. Palecek, S. P., J. C. Loftus, M. H. Ginsberg, D. A. Lauffenburger, and A. F. Horwitz. 1997. Integrin-ligand binding properties govern cell migration speed through cell-substratum adhesiveness. Nature 385:537-540.
5. Dimilla, P. A., K. Barbee, and D. A. Lauffenburger. 1991. Mathematical-Model for the Effects of Adhesion and Mechanics on Cell-Migration Speed. Biophys. J. 60:15-37.
6. Lo, C. M., H. B. Wang, M. Dembo, and Y. L. Wang. 2000. Cell movement is guided by the rigidity of the substrate. Biophys. J. 79:144-152.
7. Engler, A., L. Bacakova, C. Newman, A. Hategan, M. Griffin, and D. Discher. 2004. Substrate compliance versus ligand density in cell on gel responses. Biophys. J. 86:617-628.
8. Discher, D. E., P. Janmey, and Y. L. Wang. 2005. Tissue cells feel and respond

to the stiffness of their substrate. Science 310:1139-1143.

9. Georges, P. C., and P. A. Janmey. 2005. Cell type-specific response to growth on soft materials. Journal of Applied Physiology 98:1547-1553.

10. Ghosh, K., X. D. Ren, X. Z. Shu, G. D. Prestwich, and R. A. F. Clark. 2006. Fibronectin functional domains coupled to hyaluronan stimulate adult human dermal fibroblast responses critical for wound healing. Tissue Eng. 12:601-613.

11. Greiling, D., and R. A. F. Clark. 1997. Fibronectin provides a conduit for fibroblast transmigration from collagenous stroma into fibrin clot provisional matrix. J. Cell Sci. 110:861-870.

12. Clark, R. A. F. The Molecular and Celluar Biology of Wound Repair. Plenum Press, New York and London.

13. Ghosh, K., Z. Pan, E. Guan, S. R. Ge, Y. J. Liu, T. Nakamura, X. D. Ren, M. Rafailovich, and R. A. F. Clark. 2007. Cell adaptation to a physiologically relevant ECM mimic with different viscoelastic properties. Biomaterials 28:671-679.

14. Ghosh, K., X. Z. Shu, R. Mou, J. Lombardi, G. D. Prestwich, M. H. Rafailovich, and R. A. F. Clark. 2005. Rheological characterization of in situ cross-linkable hyaluronan hydrogels. Biomacromolecules 6:2857-2865.

15. Wang, R. X., R. A. F. Clark, D. F. Mosher, and X. D. Ren. 2005. Fibronectin's central cell-binding domain supports focal adhesion formation and rho signal transduction. J. Biol. Chem. 280:28803-28810.

16. Clark, R. A. F., J. Q. An, D. Greiling, A. Khan, and J. E. Schwarzbauer. 2003. Fibroblast migration on fibronectin requires three distinct functional domains. J. Invest. Dermatol. 121:695-705.

17. Guan, E., S. Smilow, M. Rafailovich, and J. Sokolov. 2004. Determining the mechanical properties of rat skin with digital image speckle correlation. Dermatology 208:112-119.

18. Palecek, S. P., A. Huttenlocher, A. F. Horwitz, and D. A. Lauffenburger. 1998. Physical and biochemical regulation of integrin release during rear detachment of migrating cells. J. Cell Sci. 111:929-940.

19. Dembo, M., and Y. L. Wang. 1999. Stresses at the cell-to-substrate interface during locomotion of fibroblasts. Biophys. J. 76:2307.

20. Pelham, R. J., and Y. L. Wang. 1999. High resolution detection of mechanical forces exerted by locomoting fibroblasts on the substrate. Mol. Biol. Cell 10:935-945.

21. Harris, A. K., P. Wild, and D. Stopak. 1980. Silicone-rubber substrata - New wrinkle in the study of cell locomotion. Science 208:177-179.

22. Santas, A. J., J. A. Peterson, J. L. Halbleib, S. E. Craig, M. J. Humphries, and D. M. P. Peters. 2002. Alternative splicing of the IIICS domain in fibronectin governs the role of the heparin II domain in fibrillogenesis and cell spreading. J. Biol. Chem. 277:13650-13658.

23. Mostafavi-Pour, Z., J. A. Askari, J. D. Whittard, and M. J. Humphries. 2001. Identification of a novel heparin-binding site in the alternatively spliced IIICS

region of fibronectin: roles of integrins and proteoglycans in cell adhesion to fibronectin splice variants. Matrix Biol. 20:63-73.

2.6 Figure Captions

Figure 2. 1 Average cell migration speed on HA/FNfds hydrogels with different stiffness.

Figure 2. 2 Cellular mechanical responses to different substrate stiffness. Displacement (A) and shear stress (B) generated by AHDFs on HA hydrogel with shear storage moduli of 95 Pa, 550 and 4270 Pa, respectively. Displacement maps were obtained using DISC technique with color bar unit: μm. By applying the displacement field as boundary conditions in FEM, corresponding shear stress maps were gained on different scales (upper three) or one fixed scale (bottom three) with color bar unit: Pa. (C) Mechanical work done by AHDFs on HA hydrogel with different stiffness. It was stored in elastic substrate as strain energy calculated by FEM. Absolute value for 4270 Pa hydrogel =2.9 $\pm$ 0.1 pJ (n=3). * indicates $p<0.05$.

Figure 2. 3 Schematic of human plasma fibronectin showing the four functional domains of interest: C, HV, H and V.

Figure 2. 4 Actin organization of cells on HA hydrogels with different fibronectin functional domains at the same bulk density of 0.26 uM. Scale bar = 20 μm.

Figure 2. 5 Cell spreading area (A), aspect ratio (B), and average migration speed (C) as a function of ligand types. AHDFs spread better, show larger polarity and migrate significantly faster on substrate with C and HV domain than those on substrate with H domain. * indicates $p<0.05$.

Figure 2. 6 Cellular mechanical responses to different ligand type at the same density

of 0.26 uM. (A) Displacement and shear stress generated by AHDFs on HA hydrogel with C/HV/H domain respectively. Upper three are displacement maps obtained using DISC technique with color bar unit: μm. By applying the displacement field as boundary conditions in FEM, corresponding shear stress maps were gained as bottom three with color bar unit: Pa. (B) Traction fields represented in a 3D manner to show traction gradients across the whole cell. (C) Mechanical work done by AHDFs on HA hydrogel with different FNfds. It was stored in elastic substrate as strain energy calculated by FEM. Absolute value for C domain =16.4 $\pm$ 0.71 pJ (n=4). * indicates $p<0.05$.

Figure 2. 7 Cell spreading area (A), aspect ratio (B), and average migration speed (C) as a function of density of C domain.

Figure 2. 8 Cellular mechanical responses to C domain at different bulk density. (A) Shear stress generated by AHDFs on HA hydrogel with C at 0.26 μM, 0.52 μM, and 1.04 μM, shown on different and same scales as the upper and bottom three respectively with color bar unit: Pa. (B) Mechanical work done by AHDFs on HA hydrogel with C as function of bulk density. It was stored in elastic substrate as strain energy calculated by FEM and plotted against bulk density of C domain. Absolute value at 0.26 μM = 15.7 $\pm$ 0.44 pJ (n=3). (C) Traction fields represented in a 3D manner to show traction gradients across the whole cell.

Figure 2. 9 Cell spreading area (A), aspect ratio (B), and average migration speed (C) as a function of density of H domain. They were all improved by increasing the bulk

density of H. Especially, migration speed was repaired a lot when the density of H domain increased from 0.26 μM to 1.04 μM, but further increase up to 2.60 μM did not induce obvious improvement any more.

Figure 2. 10 Cellular mechanical responses to H domain at 1.04 μM compared with HV domain at 0.26 μM. (A) Shear stress generated by AHDFs on HA hydrogel. (B) Traction fields represented in a 3D manner to show traction gradients across the whole cell. (C) Mechanical work done by AHDFs on HA hydrogel with H as function of bulk density. Absolute value at 1.04 uM = 13.5 $\pm$ 0.40 pJ (n=3).

2.7 Figures

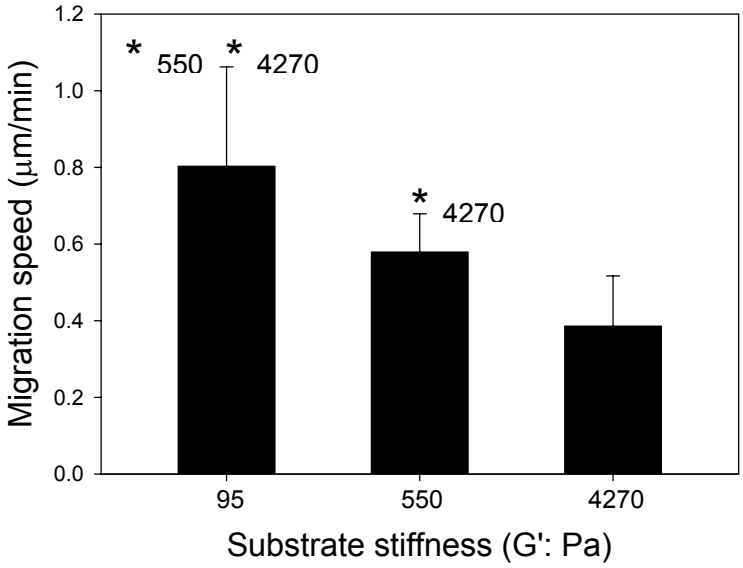

Figure 2.1

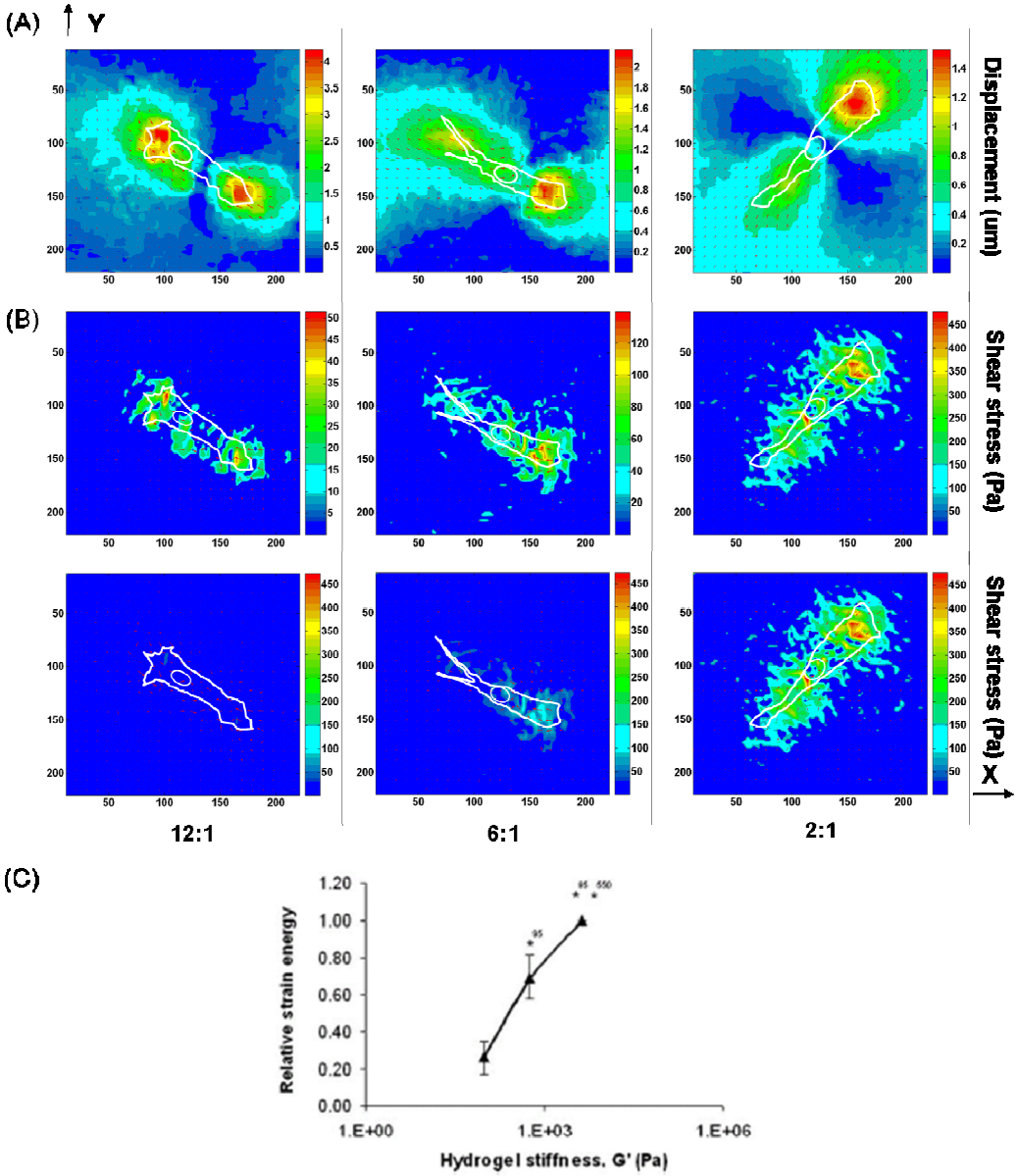
(A)
Y
Displacement (um)
(B)
Shear stress (Pa)
Shear stress (Pa)
X
12:1
6:1
2:1
(C)
Relative strain energy
1.20
1.00
0.80
0.60
0.40
0.20
0.00
1.E+00
1.E+03
1.E+06
Hydrogel stiffness, G' (Pa)

Figure 2.2

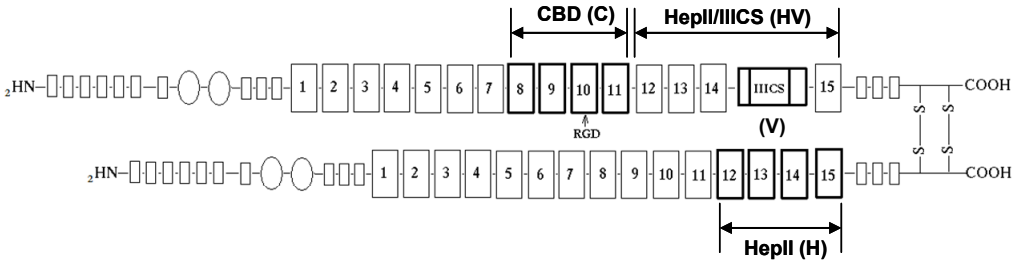
CBD (C)
HepII/IIICS (HV)
2HN
1
2
3
4
5
6
7
8
9
10
11
12
13
14
IIICS
15
COOH
RGD
(V)
S
S
S
S
2HN
1
2
3
4
5
6
7
8
9
10
11
12
13
14
15
COOH
HepII (H)

Figure 2.3

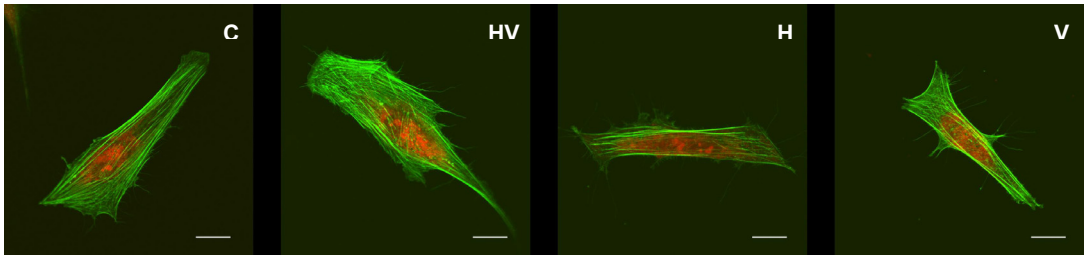

Figure 2.4

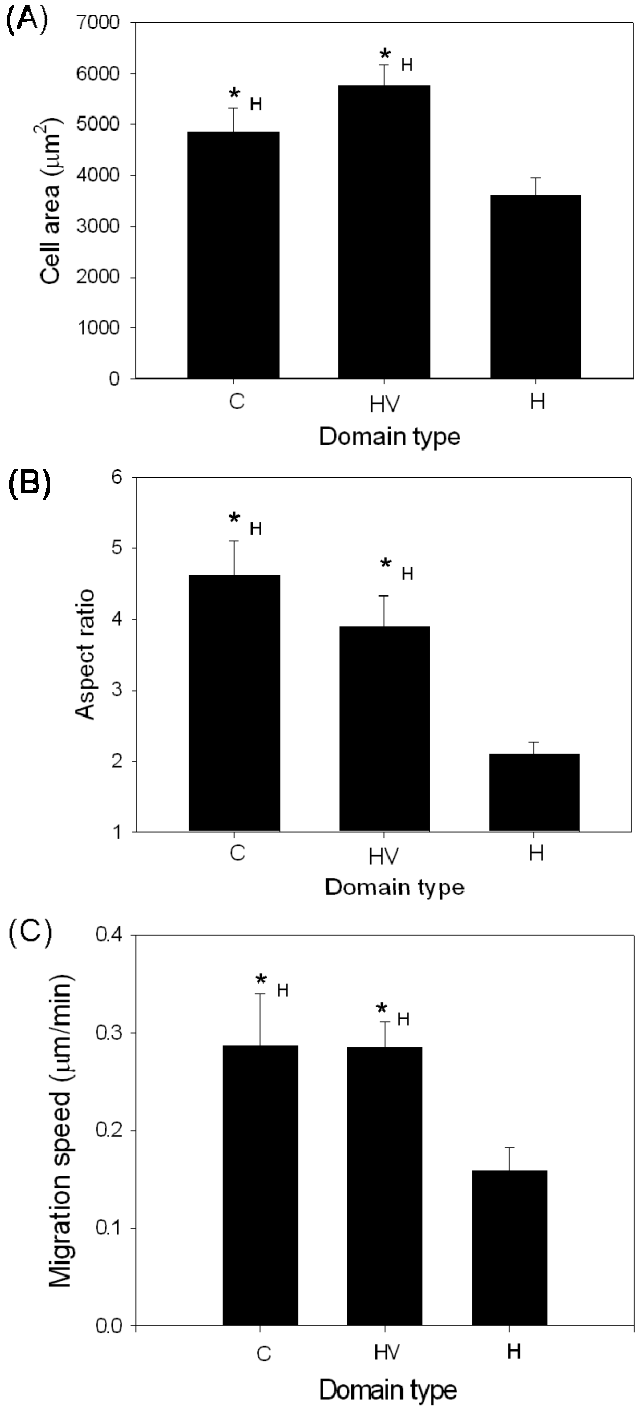
(A)
Cell area (μm²)
7000
6000
5000
4000
3000
2000
1000
0
* H
* H
C
HV
H
Domain type
(B)
Aspect ratio
6
5
4
3
2
1
* H
* H
C
HV
H
Domain type
(C)
Migration speed (μm/min)
0.4
0.3
0.2
0.1
0.0
* H
* H
C
HV
H
Domain type

Figure 2.5

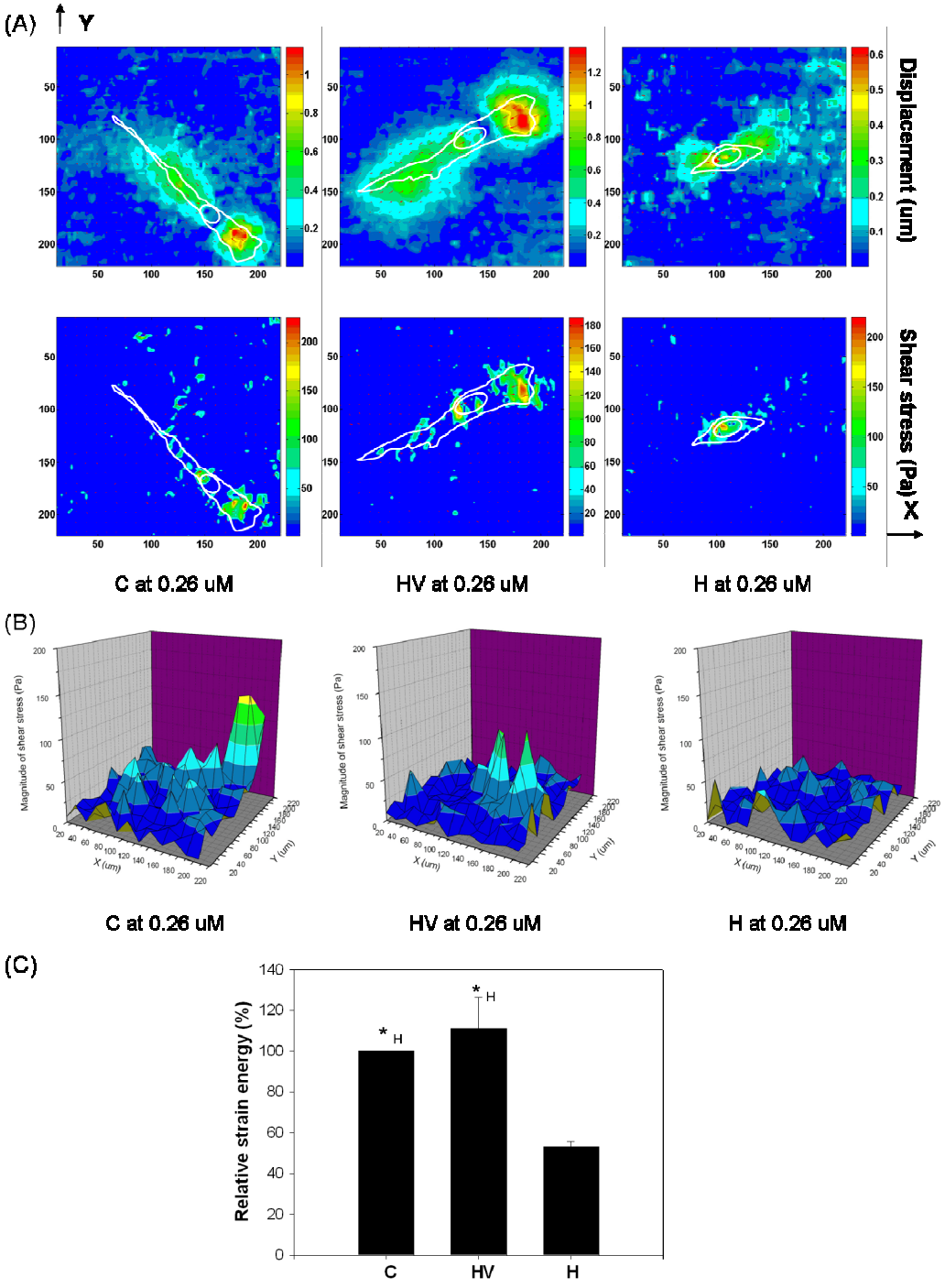
(A)
Y
Displacement (um)
Shear stress (Pa)
X
C at 0.26 uM
HV at 0.26 uM
H at 0.26 uM
(B)
Magnitude of shear stress (Pa)
X (um)
Y (um)
C at 0.26 uM
HV at 0.26 uM
H at 0.26 uM
(C)
Relative strain energy (%)
* H
* H
C
HV
H

Figure 2.6

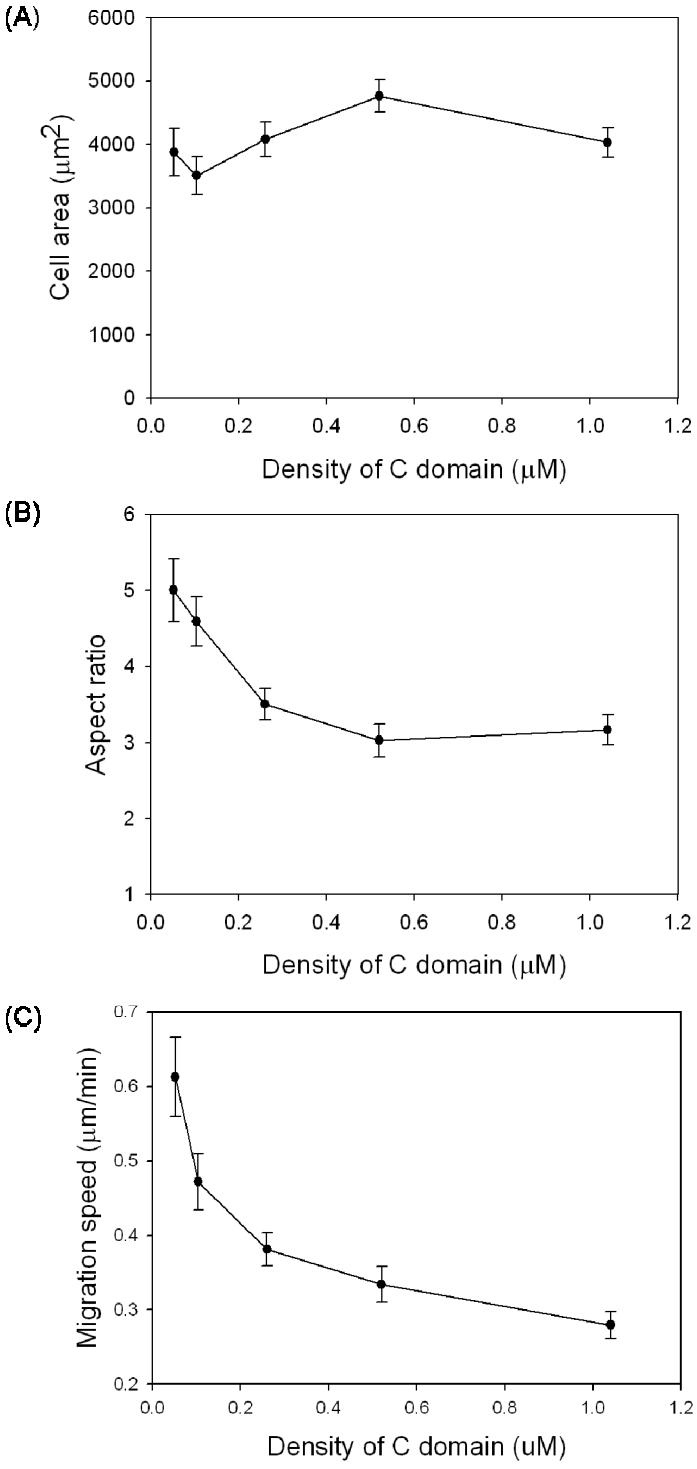
(A)
Cell area (μm2)
6000
5000
4000
3000
2000
1000
0
0.0
0.2
0.4
0.6
0.8
1.0
1.2
Density of C domain (μM)
(B)
Aspect ratio
6
5
4
3
2
1
0.0
0.2
0.4
0.6
0.8
1.0
1.2
Density of C domain (μM)
(C)
Migration speed (μm/min)
0.7
0.6
0.5
0.4
0.3
0.2
0.0
0.2
0.4
0.6
0.8
1.0
1.2
Density of C domain (uM)

Figure 2.7

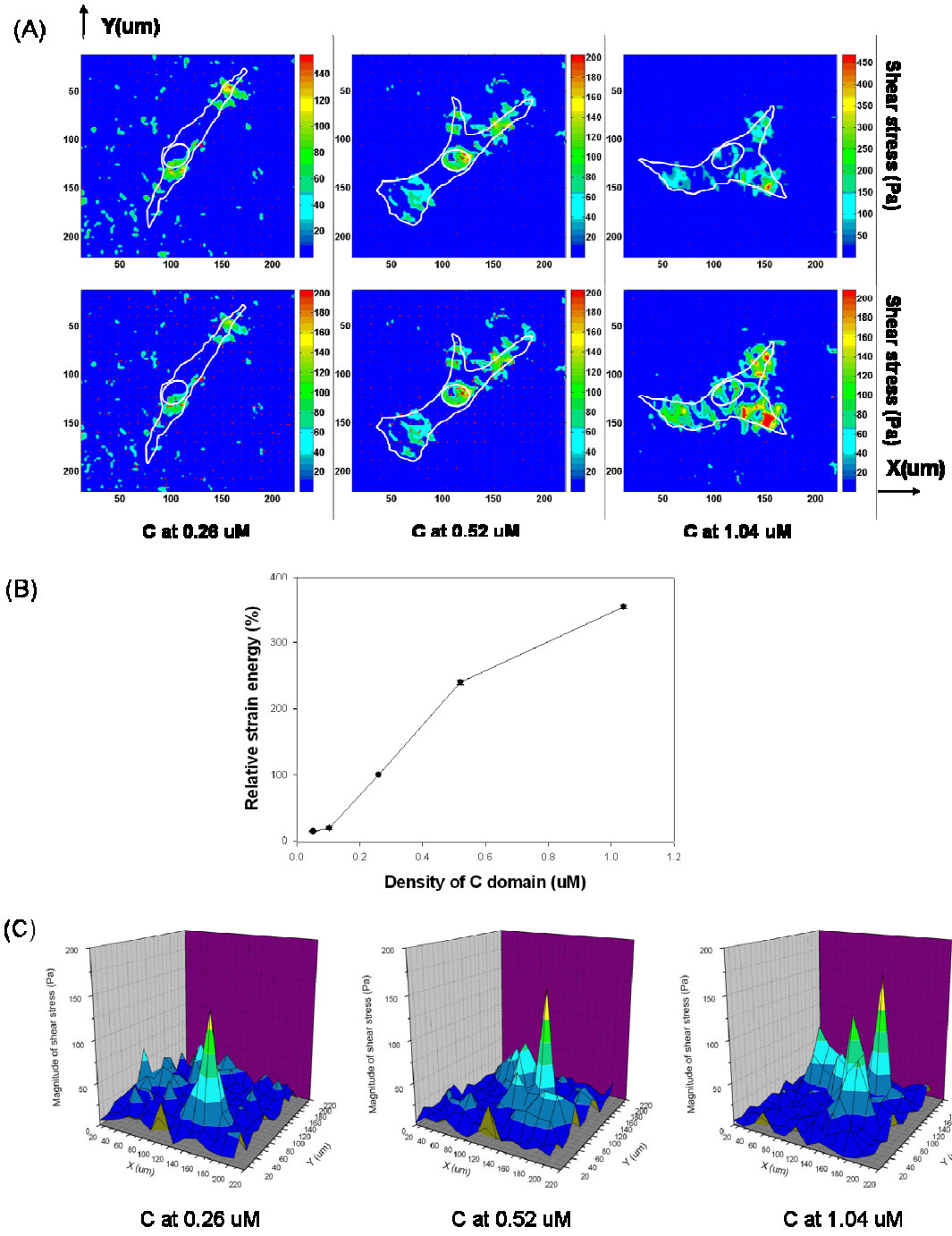
(A)
Y(um)
X(um)
Shear stress (Pa)
Shear stress (Pa)
C at 0.26 uM
C at 0.52 uM
C at 1.04 uM
(B)
Relative strain energy (%)
Density of C domain (uM)
(C)
Magnitude of shear stress (Pa)
X (um)
Y (um)
C at 0.26 uM
C at 0.52 uM
C at 1.04 uM

Figure 2.8

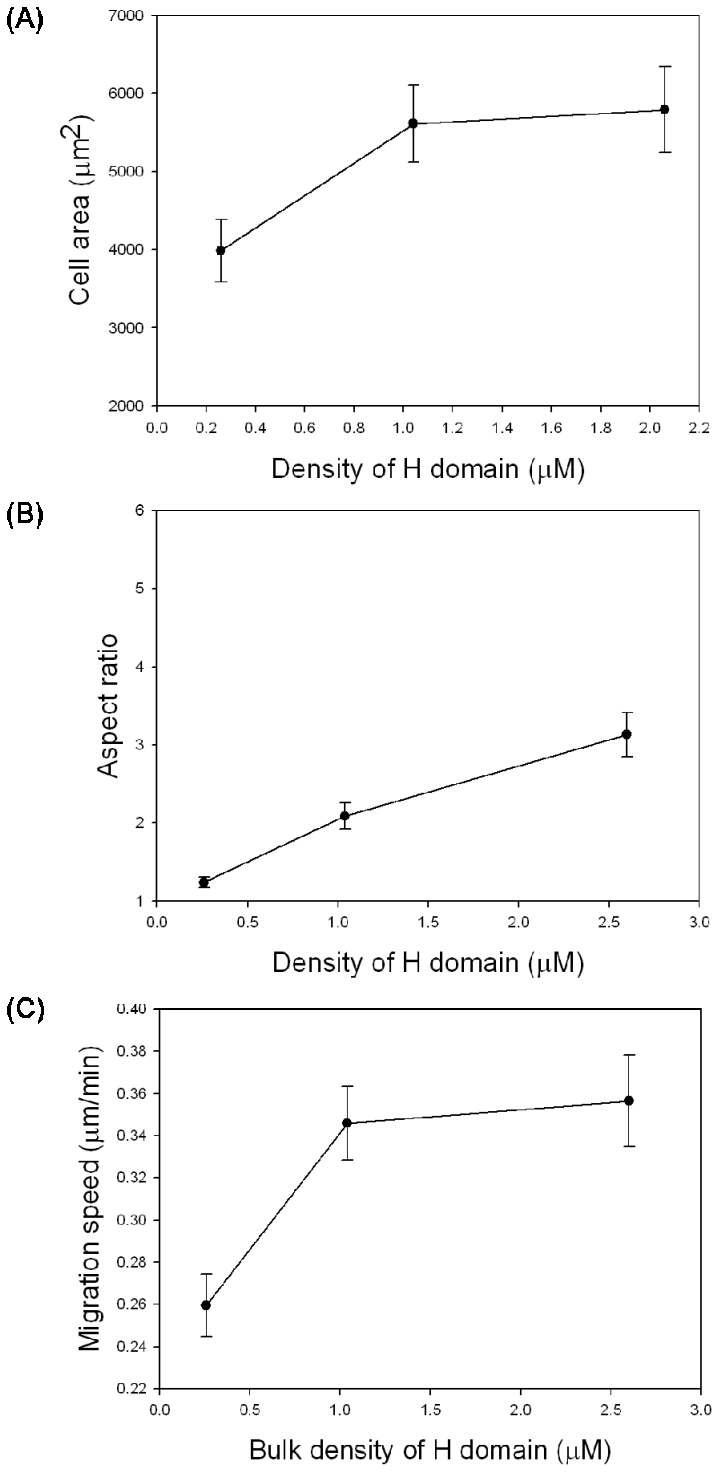
(A)
Cell area (μm2)
7000
6000
5000
4000
3000
2000
0.0 0.2 0.4 0.6 0.8 1.0 1.2 1.4 1.6 1.8 2.0 2.2
Density of H domain (μM)
(B)
Aspect ratio
6
5
4
3
2
1
0.0 0.5 1.0 1.5 2.0 2.5 3.0
Density of H domain (μM)
(C)
Migration speed (μm/min)
0.40
0.38
0.36
0.34
0.32
0.30
0.28
0.26
0.24
0.22
0.0 0.5 1.0 1.5 2.0 2.5 3.0
Bulk density of H domain (μM)

Figure 2.9

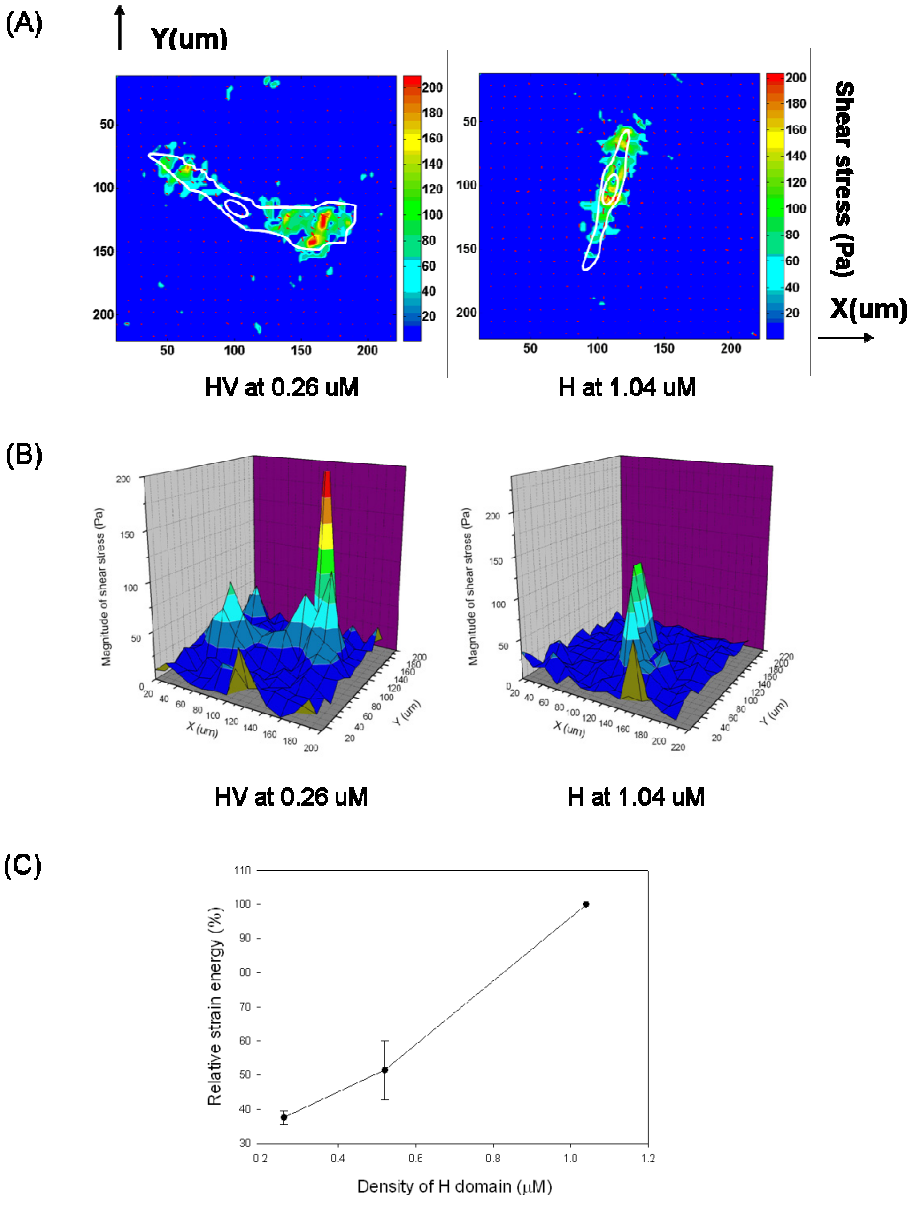
(A)
Y(um)
Shear stress (Pa)
X(um)
HV at 0.26 uM
H at 1.04 uM
(B)
Magnitude of shear stress (Pa)
X (um)
Y (um)
HV at 0.26 uM
H at 1.04 uM
(C)
Relative strain energy (%)
Density of H domain (μM)

Figure 2.10

Chapter 3

Spatiotemporal redistribution of cellular traction stresses during cell migration

Preface

This chapter has been reproduced from:

Pan, Z., K. Ghosh, Y. Liu, R.A.F. Clark, and M.H. Rafailovich. 2009. Traction stresses and translational distortion of the nucleus during fibroblast migration on a physiologically relevant ECM mimic. Biophys. J. 96: 4286-4298,

with permission from Elsevier.

Original contribution: Data for Figure 3.1 - 3.10 & Table 3.1

In collaboration: Data for Figure 3.4 - 3.6

3.1 Introduction

Cell migration plays an important role in many normal and pathological processes, ranging from tissue morphogenesis and regeneration to wound healing and tumor metastasis. As a result, a great deal of research has already been done trying to understand the process. There is general agreement that cell migration consists of a series of coordinated steps: lamellipodium extension at the leading edge, adhesion site

formation behind the leading edge, and disruption of older adhesion sites at the trailing edge with concomitant retraction of the cell rear (1, 2). Cellular traction forces are exerted or dissipated as these focal adhesion sites assemble or disassemble (3, 4). Real-time imaging of fluorescent focal adhesion components has shown that the distribution of focal adhesions occurs mostly at the trailing edge, while it remains constant at the front of the cell (5, 6). It was postulated that the cells undergo a "clutch" type of motion, with the focal adhesions at the cell rear dictating when motion would occur. Although such studies have successfully revealed the critical role of focal adhesion dynamics in cell migration, they have essentially been qualitative in nature. To unequivocally confirm such models of cell migration, it is crucial to obtain rigorous and direct measurements of the dynamics of cellular traction forces that result from the redistribution of focal adhesions.

With fluorescent beads or micro-patterned posts serving as randomly distributed or uniform arrays of markers on the surface of flexible substrates (7), traction force distribution of individual cells can be measured by quantifying the reversible substrate deformation (8-10) or post defection (11, 12) caused by cell attachment. Using these techniques, several groups have measured the static distribution of traction forces involved in cell adhesion. However, fewer studies have been performed where the dynamics of traction forces were measured. Using time-lapse analysis of the deformation of collagen coated polyacrylamide gels (13) produced by NIH 3T3 fibroblasts, Munevar et al. were able to correlate changes in the traction stress distribution pattern with changes in the direction of cell migration (14). But, since the

cell mobility in their cell-substrate system was very small, they were not able to resolve actual temporal redistribution of the individual traction forces that eventually leads to cell motion. du Roure et al. imaged, as a function of time, the deformation of posts imprinted in a PDMS gel, by epithelial cells (15). In this study the resolution was limited by the position of the posts, and the fact that the cells were forced to adhere in the areas of the posts. Hence in contrast to previous studies on planar surfaces (9, 10, 16), they found that the maximum traction forces were always localized on the edge of the cell. Even though each of these studies addressed a different fundamental aspect of cell migration, neither imaged the coordinated sequence of events that ultimately result in the locomotion of the entire cell.

In this study, we use a functionalized hydrogel, which was developed to be a physiologically relevant ECM mimic (17), and tuned to achieve large cellular traction forces with significant cell locomotion during a convenient observation time window. We also show that it is possible to apply the digital image speckle correlation (DISC) technique combined with finite element method (FEM), to analyze the redistribution of cellular traction stresses, using standard software. This technique allows us to observe in real time the redistribution of cellular traction stresses during cell migration with high spatial resolution. Furthermore, since our technique can be adapted to any hydrogel or other flexible substrates, a wide variety of physiologically-relevant constructs can be studied to obtain fundamental insights into cell dynamics on different types of tissues.

Here we chose to use intermolecularly cross-linked thiol-modified hyaluronan

(HA-DTPH) functionalized with specific fibronectin functional domains (FNfds) (18) to study the migration mechanics of primary adult human dermal fibroblasts (AHDFs). Using this system, Ghosh et al. had previously shown that the traction stresses exerted by cells were a sensitive function of the modulus of the substrate (17), which in turn was controlled by the crosslinking density. Furthermore, significant cell migration occurred on these substrates within our observation time. Hence in this study, with appropriate substrate stiffness for AHDFs, we focused on elucidating the sequence of traction stresses that lead to nuclear translocation, an indicator of cell migration. These experiments were performed as a function of ligand density, which governs cell adhesion to the substrate and consequently influences cell mobility (19) associated with other cell responses on the gel, such as cell morphology and focal adhesion distribution (20). Low ligand density surfaces (LLDS) and high ligand density surfaces (HLDS) reflective of bulk ligand densities of 0.26 μM and 0.52 μM, respectively, were investigated. These densities allowed sufficient motilities and traction forces to clearly establish the correlation between them.

3.2 Materials and Methods

3.2.1 Preparation of HA/FNfds substrates

Cysteine-tagged FNfds, C-SH and HV-SH at equal proportions, were coupled to 4.5%(w/v) crosslinker PEGDA (Nektar Therapeutics, Huntsville, AL) in PBS to form PEGDA-FNfd conjugates with different total ligand density, 0.26 μM and 0.52 μM for low ligand density surface (LLDS) and high ligand density surface (HLDS),

respectively. Then these conjugates were mixed with 1.25%(w/v) HA-DTPH(gift from Glenn D. Prestwich's lab, University of Utah, Salt Lake City, UT), in SF-DMEM (Sigma, St. Louis, MO) with volume ratio 1:4. The mixtures were seeded in 35 mm tissue culture dishes to gel. Fluorescent beads with 40 nm diameter (Molecular Probes, Eugene, OR) were sonicated and suspended uniformly at a concentration of 5%(v/v) in HA solution prior to gelation and served as markers for substrate deformation measurements. All the substrates were stored at 4 ^{o}C for >18 hours to stabilize PEGDA-mediated crosslinking before cells seeding.

3.2.2 Characterization of substrates

In the final gel, HA-DTPH and cysteine-tagged FNfds were crosslinked to PEGDA which ensure stable mechanical and adhesive properties of the substrate. The mechanical property of the substrate was adjusted to be physiologically relevant as used in previous in vivo experiment to promote wound healing (18) with a shear storage modulus G'= 4.27 kPa (21) measured by an AR2000 rheometer (TA Instruments Inc.). This stiffness was also shown as the optimal rigidity for AHDFs to form normal cytoskeleton organization, and to generate robust tractions for cell proliferation and migration (17). The central cell binding domain ($FNIII_{8-11}$ or C) and the Heparin II binding domain including the type III connecting strand ($FNIII_{12-V15}$ or HV) of fibronectin, which together are sufficient for optimal AHDF migration (22), were tethered in equal proportions to the HA hydrogel as ligands for cell adhesion. Substrate adhesiveness could be varied by changing the total ligand density without

changing the stiffness of the gel (17).

3.2.3 Cell culture and seeding

Primary dermal fibroblasts obtained from a 31 year old Caucasian female (Clonetics, San Diego, CA) were used between passages 5 and 13. The cells were routinely cultured in DMEM, supplemented with 10% fetal bovine serum and 1% Penicillin, Streptomycin and L-glutamine (P/S/G), in a 37 ^{o}C, 5% CO_2, 95% humidity incubator (Napco Scientic, Tualatin, OR). To avoid cell-cell interactions, a low density of cells (~500 /cm^2) was seeded onto HA/FNfds substrate in SF-DMEM with 1% P/S/G and followed by 6 hours incubation in the incubator. Prior to all the experiments done in atmospheric conditions, SF-DMEM was changed to CO_2-independent media (Gibco, Carlsbad, CA) with 1% P/S/G at 37 ^{o}C. Only single cells were chosen to measure traction fields and nuclear translocation.

3.2.4 Measurement of cellular/nuclear aspect ratio, cell area and migration speed

Time-lapse phase images of the cells were recorded every 15 minutes over a one-hour time window with a MetaMorph-operated CoolSNAP^{TM} HQ camera (Universal Imaging, Downingtown, PA) attached to a Nikon Diaphot-TMD inverted microscope fitted with a 37 ^{o}C stage incubator and a 10x objective lens. Using MetaMorph software, aspect ratio of cells and nuclei and projected cell area were obtained from phase images by measuring both major and minor length of each cell and its nucleus or area covered by the outline of each cell. The migration speed was determined from the time-lapse images by tracking the distance covered by the center of a cell nucleus

over every 15 minutes in one hour. This was a carefully chosen observation window where notable fibroblast migration was observed and no corrections for instrumental stability on the microscope had to be made. In order to determine whether cell migration speed was a function of the observation time, it was also measured with an observation window of two hours, and no significant difference was observed. The sample size n used was 5x10 cells/field x 3~5 fields. Results shown in Fig. 3.1 and 3.3 are representative of 3 independent experiments.

3.2.5 Vinculin staining and visulization

Since immunouorescent staining of vinculin-containing focal adhesions was difficult to perform in cells plated on the hydrogels (owing to non-specific absorption of antibodies within hydrogels that led to a high fluorescence background), we coated tissue culture dishes with low and high densities of FN, which produced surfaces that induced cell motility similar to the LLDS and HLDS of hydrogels, respectively. 35 mm tissue culture dishes filled with 2 ml 15 μg/ml or 30 μg/ml FN solutions were maintained overnight at room temperature, and then blocked using 2% (w/v) bovine serum albumin (BSA) at room temperature for 2 hours. Each dish was rinsed three times with PBS, and then cells were seeded at low density in serum-free DMEM and incubated at 37 ^{o}C for 6 hours. The cells were then fixed with 4% paraformaldehyde in PBS for 15 minutes, permeabilized with 0.4% Triton in PBS for 5 minutes, and blocked with 2% BSA in PBS for 30 minutes at room temperature. Focal adhesions were visualized by immunostaining for vinculin, where anti-vinculin primary

antibody (Sigma, V9131) was incubated with cells at 1:600 dilution for 1 hour at room temperature , followed by incubation with Oregan Green 488 goat anti-mouse secondary antibody (Invitrogen, O11033) at a 1:800 dilution for 1 hour. After washing, cells were kept in PBS at 4 ^{o}C and imaged using a Leica TCS SP2 laser scanning confocal microscope Leica Microsystems) using a 63x NA 0.9 water objective lens. The number of vinculin-positive focal adhesions at the cell front and rear as well as across the entire cell area were quantified using ImageJ.

3.2.6 Measurement and calculation of cellular tractions using DISC and FEM

Quantification of cellular traction forces was accomplished by using the DISC technique combined with FEM as previously described (17), which can provide rapid and accurate measurements of cellular traction distribution with high spatial resolution. Briey, in order to track deformations induced by the migrating cell, fluorescent beads were embedded in HA/FNfds hydrogel with an optimized density of 5% (v/v). After AHDFs were seeded on the substrate and incubated in SF-DMEM at 37 ^{o}C for 6 hours, the media was changed to CO_2-independent media prior to microscopy and the whole sample was placed on a 37 ^{o}C heated platform during observation. Phase contrast images of a single migrating cell and fluorescence images of the underlying (substrate-embedded) beads were recorded simultaneously every 15 minutes over an hour with a differential interference contrast (DIC) lens and a 63x, NA 0.9 water objective lens on a Leica TCS SP2 laser scanning confocal microscope (Leica Microsystems). The former provided the outline of the cell and the position of

its nucleus, while the latter recorded the redistribution of the embedded fluorescent beads. Then images of bead positions in non-stressed gels were taken after completely detaching the cell from the substrate with the treatment of trypsin-EDTA. The confocal pinhole size was always set at optimal state so that only the beads in the top narrow layer of the substrate were recorded, and all images were recorded with a CCD camera at the same resolution of 1024x1024 in pixels. DISC technique was applied to compare the bead distribution change between each stressed and non-stressed image. It divided stressed image into small subsets and searched for a best match in the non-stressed image, following the equation as below:

$$S\left(x, y, u, v, \frac{\partial u}{\partial x}, \frac{\partial u}{\partial y}, \frac{\partial v}{\partial x}, \frac{\partial v}{\partial y}\right) = 1 - \frac{\sum I(x,y) * I^*(x^*, y^*)}{\sqrt{\sum I(x,y)^2 * \sum I^*(x^*, y^*)^2}}$$

$$x^* = x + u$$

$$y^* = y + v$$

Where (x, y) and (x^*, y^*) are the coordinates of matched subset pair, I and I^* are the intensity in corresponding subsets, and (u, v) is the coordinate difference between them which provides the displacement vector from the position in non-stressed image to the stressed image with the best match, $S \sim 0$. The size of subset and the distance for the matched pair searching were empirically determined. The density of fluorescent beads was optimized to make sure that there are always several beads in each subset in order to avoid the error in calculation. Since DISC technique utilizes the total intensity in each subset, I and I^*, to minimize the cross-correlation function (S), its resolution has nothing to do with individual beads. Because the position of initial subset can be moved pixel by pixel, DISC technique can produce displacement

data with high spatial resolution which is only limited by the resolution and size of the digital image.

The time sequence of displacement data with sufficient spatial resolution was then used as the top surface boundary conditions in a long vertical cube (209 × 209 × 518 μm^3) FEM model composed of 8-node 3 dimensional solid elements. Standard finite element software (ABAQUS Inc., Providence, RI) was employed to perform FEM calculation. The shear stress map on top surface determined by FEM represented the cellular traction field at each time point. Different from previous method which utilizes Tikhonov regularization with a particular choice and intensity of smoothing functional (9), FEM uses no smoothing and yields an exact traction field directly based on the given displacement map. The spatial resolution is carefully chosen by considering both FEM model accuracy and its computation complexity. In this case, considering the size of the field of interest, traction fields over the whole cell were calculated from each element with nodes in every 2.3 μm along each dimension to achieve a high calculation speed, and tractions in localized regions were done at nodes in every 0.70 μm (see inset in Fig. 3.5) along each dimension to gain higher resolution. The maximal traction stresses in each field did not change at different resolutions, demonstrating the reliability of this method. However, higher resolution allowed better localization of the traction distribution in smaller areas. Because high precise DISC data elucidated any displacement on the substrate surface and no hand-drawn cell boundaries were necessary in this algorithm, all shear stresses occurring over the whole field were obtained including the background noise. Nevertheless, to

emphasize the cellular tractions of interest, the background was removed from the final displayed traction field by filtering the values below a threshold defined by the average noise in each field. Because the examined cell was randomly chosen, results are representative of at least three migrating cells on LLDS and HLDS, respectively.

To revalue the strength of cell-substrate adhesion, the mechanical work done by the cell (W) was estimated by the strain energy (E) stored in the elastic substrate and calculated in the same FEM model using the equation as below:

$$W = E = \frac{1}{2}\int \sigma_{ij}(\vec{r}) \cdot \varepsilon_{ij}(\vec{r}) dV \qquad \text{i, j =1, 3.}$$

The net stress in each subregion and the total stress over the entire cell were calculated by summing all the stress vectors in certain area of interest. These sums are proportional to the net force in subregions and the total net force, which are utilized to explain the cell motion in this paper.

3.3 Results

3.3.1 Cell migration on HA/FNfds substrates with different ligand densities

The average migration speed of single cells, cultured on LLDS or HLDS substrates for 6 hours in serum free DMEM (SF-DMEM), was measured by time-lapse photography over a period of one hour and plotted as a histogram in Fig. 3.1(A). We found that the migration speed is nearly three times faster on LLDS than on HLDS. In Fig. 3.1(B) shows the morphology of typical cells on both surfaces. In Fig. 3.1(C) we plot the average aspect ratio calculated from the ratio of the major to the minor length of the cells and the nuclei shown in Fig. 3.1(B), together with the cell area. From the

figure we can see that the aspect ratios of the cells and their nuclei are 40% and 23% higher, and the cell area is approximately 20% smaller, on LLDS than on HLDS, indicating that cell morphology and migration speed are correlated.

Since the dynamics of focal adhesions is known to influence cell polarization and migration, we monitored the number and distribution of vinculin-positive focal adhesions in cells cultured on the low and high FN density 2D surfaces. Fig. 3.2(A) shows fluorescent images of vinculin-positive focal adhesions in a typical cell on each substrate, while Fig. 3.2(B) is a plot showing the quantitative comparison of the focal adhesion number and distribution between the weaker and stronger adhesive surfaces. The total number of focal adhesions per cell is an indicator of cell-substrate adhesion, while the ratio of focal adhesion numbers between the front and rear of a cell indicates its degree of polarization. From Fig. 3.2(B), we observe that the cells on the high FN density surface have nearly 30% more focal adhesions on average than on the low FN density surface, which scales directly with the differences in ligand density between the two surfaces. The distribution of focal adhesions on the other hand, appears to be more asymmetric, on the low FN density surface, with more focal adhesion points at the front of the cell than at the rear (Fig. 3.2(C)). Since the locus of these focal adhesions is also associated with cellular traction forces exerted on the substrate, the imbalance may also be an indicator of larger total traction stresses on the low density surface, which is consistent with the higher migration speed observed on LLDS.

In a previous report, it was shown that the locus of the focal adhesions at the rear

of the cell migrated towards the interior, with a time interval of approximately 10 minutes, while the complexes at the front remained stationary (5). This indicates that the traction forces are readjusting over that time interval, and hence information is lost when averaging the migration speed over a period of one hour. We therefore divided the hour into 15 minute time intervals, and measured the nuclear translocation of the cells in the ensemble at the end of each interval. We then classified the nuclear translocations in every 15 minute interval into three different groups, large: > 10 um, medium: 5~10 um, and small: < 5 um. In Fig. 3.3(A) we plot the percentage of the cells which undergo small, medium, and large translocations during every 15 minute interval, over a period of one hour. From the figure we see that the population is bimodal on the LLDS, with the percentage of cells having large translocations nearly equal to the percentage of cells having small translocations. On the HLDS though, most cells undergo small translocations. Looking further into the distribution of cells having large nuclear translocations (Fig. 3.3(B)), we find that the number of large translocations in every 15 minute interval over an hour has a normal distribution for cells on LLDS, while most cells on HLDS have no large translocation. The average numbers of large nuclear translocation are 1.61 ± 0.17 on LLDS and 0.16 ± 0.03 on HLDS. Furthermore, we also tried to determine whether there was a specific time point in the one hour sequence when the large translocations were most likely to occur. The results are plotted in Fig. 3.3(C) where we see that the probability of any cell in the population undergoing a large translocation is the same, within experimental error, for each of the time intervals. These results clearly indicate that (a) cells do not move

continuously on either surface. Rather, the cells move in a pulsed manner with short pulse intervals. (b) The size of nuclear translocations in a given pulse is a function of the surface ligand density, which in turn regulates the cell polarization and focal adhesion distribution.

Different distribution profiles of nuclear translocations on LLDS and HLDS also suggest that the cellular traction forces redistribute in different ways during cell migration. Thus, we decided to investigate the spatiotemporal redistribution of cellular traction forces on both surfaces within these 15 minute intervals, taken over a period of one hour. In this case, rather than obtaining an ensemble average, we studied individual cells where the traction stress distribution across the cell could be directly correlated with the nuclear translocation, rather than a statistical average.

3.3.2 Traction stress distribution during cell migration

Imaging the traction force distribution:

The substrate deformation induced by cell attachment was analyzed using a previously established DISC technique (23). Fig. 3.4(A) shows a displacement vector map generated by a typical migrating cell on LLDS with distinct front and rear ends. The outline of the cell and its nucleus obtained from the DIC image is superimposed. The resolution of DISC technique is only limited by the resolution of digital images taken by confocal microscope recording the fluorescent bead distribution, from which displacement data for each pixel point (1024×1024 in this study) can be obtained. Here, vector density is diluted by 1: 160 to make the map clear. From the vector map

we can see that the largest displacements occur in well defined loci along the protrusion of the cell, and all the displacements are radially distributed from the nuclear region, which is consistent with previous reports (10).

The DISC results are then input into the FEM which then calculates the stress and strain fields associated with the given displacements. We assume that the modulus of the gel is uniform and isotropic, and the stress and strain fields are linearly related. In Fig. 3.4(B), we show the corresponding stress field generated by the cell attachment on LLDS. With high spatial resolution, we imaged where these stresses are applied relative to the cell membrane and the locus of nucleus. Since the cell is not a rigid body, the stresses that are exerted in different subregions can vary greatly. We therefore subdivided the cell into three regions, the front, the nuclear and the rear, where we found the largest stress concentrations. The traction forces behind leading edge and at trailing edge of the cell are usually known as propulsive and resistant forces (14). Forces in the vicinity of the nucleus have been reported previously (24), but their function has not been known. In order to determine the role of these forces in the migration of cells, time sequence data were obtained for each of the different substrates with either LLDS or HLDS.

Low Ligand Density Substrates:

Time sequences of the displacement and traction fields induced by a migrating cell on LLDS are shown in Fig. 3.5. In each image, the perimeter of the cell and its nucleus are outlined by highlighting the phase contrast images. From this figure, we see that propulsive traction stresses were concentrated behind the cell leading edges along two

directions (labeled as a and b in Fig. 3.5), while resistant tractions were at the trailing edge (labeled as e in Fig. 3.5), which strategically balance the traction stresses at the front. The inset in Fig. 3.5 is a high resolution plot of the cell's initial leading edge, where the individual vectors corresponding to the locus of each traction stress are clearly resolved. With high spatial resolution at 0.70 μm determined by the element size in the FEM model, these rearward stresses were shown to localize within a narrow band, no more than 1~2 μm, positioned approximately 10~20 μm behind the leading edge, in agreement with previous reports (9, 10, 16). However, this traction stress loci at the initial leading edge disappeared 15 minutes later, which resulted in a retraction of this leading edge, while the traction stresses behind the other leading edge enhanced. More interestingly, after 30 minutes, two loci of traction forces in the perinuclear region appeared. The loci were near the front and the rear edges of the nucleus, respectively (labeled as c and d in Fig. 3.5).

In order to determine the role of individual cellular traction forces leading to cell migration, we carefully compared the redistribution of main traction stresses in the five subregions chosen (a-e) and correlated them to the nuclear translocation occurring during the observation time. The magnitude of the net stresses in each subregion (proportional to the localized force) is plotted as a function of time in Fig. 3.7(A), and the nuclear translocation during the same time plotted in Fig. 3.7(B). In Fig. 3.7(A), all rearward traction stresses (a,b and c) are plotted as being in the positive direction while the forward resistant traction stresses (d and e) are plotted as being in the negative direction. It was noticed that the magnitudes of the net stresses

at the cell front (a and b) remained fairly large and increased slowly over time. When the resistant traction stress (e) still existed at the trailing edge from t = 0 to t = 15 min, no nuclear motion was observed. Then, the nucleus moved slightly, to the upper left as a new set of traction stresses (c and d) were formed around the nucleus at t = 30 min which served as a "brake" for the peripheral traction stresses as the stress at the trailing edge of the cell (e) decreased. The rearward nuclear traction stress (c) at the front edge of the nucleus was relatively small and stable, while the forward one (d) at the rear edge of the nucleus kept growing to balance the large traction stresses behind the leading edges of the cell (a and b) instead of the decreasing traction stress at the rear of the cell (e), from t = 30 min to t = 60 min. When the rear traction stress (e) was completely dissipated, the tail of the cell retracted at t = 60 min. Therefore, the resulting pulse propelled the nucleus to abruptly move forward to the position shown in the last frame, where the equilibrium was reestablished and the cycle would begin again.

The large magnitude of pulsed nuclear translocation is consistent with the high mobility previously measured for the cell ensemble on the LLDS. Cells on LLDS presented large nuclear forward-translocations subsequent to retractions of the trailing edge. This phenomenon is accompanied with the relocation of resistant traction stresses from the trailing edge of the cell to the rear edge of the nucleus. These observations clearly demonstrate that the spatiotemporal redistribution of cellular traction stress not only dictates the direction but also the speed of cell migration.

The total stress over the entire cell, proportional to the total net force of the cell, is

plotted in Fig. 3.7(C) together with the mechanical work done by the cell (strain energy) during cell migration for each of the time intervals. From the figure we can see that even though the traction stresses in the individual domains vary significantly, the total stress on the cell appears to be constant, since the increase in the positive traction stress in the regions at the front of the cell is balanced by the increase in the traction stress at the rear of the nucleus, which acts as a braking force on the cell motion. No obvious correlation can be found between the total stresses with the instantaneous cell motion. Rather, the deformation of individual subregions, each subject to its own set of local stresses appears to determine the impulse that results in a nuclear translocation. The energy exerted by the cell (or the mechanical work done by the cell) does not occur in a pulsed manner either. From the figure we can see that the total energy exerted by cell in each time interval is constant, which is reasonable considering the time constant of the internal metabolic processes.

It is interesting to note that the nucleus not only undergoes translocations, but also deformation. This too can be seen to be a result of the stresses applied in its perimeter. In Fig. 3.7(D), we plot the aspect ratio of the nucleus as a function of time. We can see that the aspect ratio is largest before the nuclear traction stress is generated. Hence the nuclear deformation arises from stresses pulling the cell in opposite directions at the leading and trailing edges. As the nuclear traction stresses increase, they balance the stresses at the cell perimeter, causing the aspect ratio to decrease and assume a more relaxed shape. After the translocation occurs, the nuclear aspect ratios reach its smallest point. Since the translocation is also associated with a complex sequence of

events resulting in the retraction of the rear segment of the cell, it is possible that the nuclear deformation may have initiated the signaling pathways which regulate the distribution of the traction forces.

High ligand density substrates:

In Section 3.3.1, we established that the ligand density of the susbstrate determined the average migration speed. We showed in Fig. 3.1(A) that the migration speed on the LLDS was nearly three times larger than on the HLDS. While the cell area was somewhat larger on the HLDS, the aspect ratio was much smaller. In order to understand the relationship between the ligand density and these effects, we also measured the cellular traction redistribution on HLDS. The displacements and traction fields generated by a typical migrating cell on the HLDS are shown in Fig. 3.6. In this case we see that the cell appearance is triangulated with large traction stresses behind two leading edges (labeled as a and b in Fig. 3.6) and at the cell rear (labeled as e in Fig. 3.6). In addition, traction stresses are also present on opposite sides of the nucleus (labeled as c and d in Fig. 3.6) at all times. From the figure we can see that the amplitude of the traction stresses and the displacements are approximately twice as large on the HLDS as on the LLDS, which is consistent with the 2-fold increase in ligand density of the substrates.

During migration, the forward traction stress at the nuclear rear edge (d) still gradually replaced the rear traction stress (e) and worked as a regulator to control the nuclear translocation similar to LLDS as shown in Fig. 3.7(A). However, this relocation from the rear of cell to the rear edge of the nucleus seemed to take a much

longer time on the HLDS, probably due to the higher magnitude of traction stresses. Within the one hour observation time, these nuclear traction stresses are fairly balanced by the other traction stresses around the cell periphery and therefore the shape of the cell remains symmetric. The major consequence of the symmetric arrangement of the traction stresses is the small amplitude of the nuclear translocation (Fig. 3.7(B)). These observations are consistent with previous reports that rear retraction is dominant limitation for cell migration on a highly adhesive surface (25), and clearly explain why the overall cell mobility is much slower on HLDS from a mechanical point of view.

The total net stress over the entire cell and mechanical work done by the cell during migration is plotted in Fig. 3.7(C) as a function of time. In contrast to the cells on LLDS, we find that the total stress on HLDS is smaller even though the magnitudes of the local stresses are nearly an order of magnitude higher. The distribution of the stresses on the other hand, is far more balanced on HLDS, as can be seen from Figures 1 and 2, since their aspect ratios are smaller and there are more focal adhesions distributed over a broader area. This is also reflected in the mechanical work done by the cell (strain energy), which is much higher on HLDS than on LLDS. Hence we can see that the work done on a substrate is mostly a function of cell-substrate adhesion rather than the actual motion of the cells.

In Fig. 7(D), we also plot the aspect ratio of the nucleus at different times for the cell migrating on the HLDS. From the figure we can see that the ratio is much smaller than on the LLDS, and remains fairly constant through the motion cycle. The small

deformation of the nucleus is consistent with the presence of the large nuclear traction stress and the much smaller nuclear translocation observed on these surfaces.

Traction stress gradient:

In Fig. 3.8(A), we show 3D plots of the initial traction gradient for the cells on the LLDS and the HLDS. From the figure we can see that the individual stresses on the HLLDS are much larger than on the LLDS. However, those on the LLDS are weighted towards the front of the cell. Furthermore, the cell morphology is more elongated, enhancing the polarity of the cell. Three randomly selected cells on each substrate were analyzed in this manner, with very similar results. In Figure 3.8(B) and (C) we plot the mechanical work done by the cell and the total nuclear translocation over one hour observation period on each surface, averaged for the three cells studied. The translocations observed are consistent with those shown previously for the larger cell ensemble in Fig. 1(A). From the figure we see that it is not the cell-substrate adhesion but the traction gradient across the entire cell that directly determines the cell mobility.

The event which triggers the nuclear translocation of the cells on both surfaces is the detachment of the cell rear (25), and the relocation of the stresses from the rear of cell to the vicinity of the nucleus. In Fig. 3.9, we plot the ratio between the rear traction stresses and the nuclear rear traction stresses obtained over the observation period for individual cells on each surface described above. We find that the ratio is significantly larger at the beginning on the LLDS than on the HLDS and decrease in a much faster way, finally achieving zero at the end of the observation period. The

change in the stress gradient at the rear section of the cells is clearly correlated with the impulse that results in the nuclear translocation in each case. The maximal net stresses at rear and nuclear rear of three cells on each substrate are presented in Table 3.1. The maximal net stresses at rear and nuclear rear are comparable for each cell. This shows that although individual cells are different in their size, shape and traction distribution, the replacement of traction stresses from the cell rear to the posterior end of the nucleus is always observed.

3.4 Discussion

We developed a new system to image the spatiotemporal redistribution of cellular traction stresses during cell migration. The techniques of DISC combined with FEM, which have long been used to analyze mechanical defects of materials, were successfully applied to the dynamic measurement of cellular traction stresses. We designed a physiologically relevant ECM mimic, HA/FNfds hydrogel, and produced gels with a controlled modulus that allowed cells to generate a clear distribution of cellular traction stresses. We then imaged the sequence of these traction stresses during cell migration, and compared the process on substrates with different ligand density and cell adhesion. We found that fibroblast migration is a discontinuous process which occurs when a small imbalance of the local traction stresses occurs. We show that cell migration is the result of a spatiotemporal redistribution of cellular traction stresses, which readjust themselves continuously to maintain a constant total net stress. Motion occurs in a pulsed manner, when a large relocation of the stresses,

from the rear to the nucleus of the cells occurs. The sequence was similar on both LLDS and HLDS, but the magnitude of the pulses was found to correlate with the ligand density and the cell-substrate adhesion.

Our results showed that migrating cells are always polarized along certain directions with clear front and rear. Several loci of strong traction stresses are observed at the leading edge, which are invariably balanced by a concerted locus at the rear of the cell. Preparation of motion is usually signaled by a decrease in the magnitude of the rear stresses. A new traction is then observed to arise in the nuclear region which grows proportionally to the decrease of the rear traction and mainly along the same direction. This “braking” force prevents cell imbalance and motion. As the rear traction decreases, a point is reached where the rear region becomes completely detached from the substrate and contracts. At this point the rear traction is seen to abruptly disappear and a momentary imbalance in the traction forces occurs. This results in an imposed force to the cell, inducing a forward motion of the nucleus. The motion stops as the nuclear braking force increases even further to completely balance the front traction forces. The front of the cell then moves forward and the cycle begins again. When the ligand density is increased on the hydrogel, the cell-substrate adhesion is enhanced and much stronger traction forces form. The sequence of events is similar, but complete release of the rear edge is more difficult to achieve and takes longer. Consequently the total motion of the cell is slower.

Compared with previous studies, we found that the appearance of traction stresses around nuclei plays an important role to replace the resistant traction at the rear and

maintain a relatively steady movement of the entire cell body. Furthermore, we demonstrated that it is the redistribution of cellular traction stresses occurring among three discrete mechanical regions, the front, the rear and the nuclear region, rather than total traction stress across the entire cell, that leads to the pulsed manner of cell migration. This implied that although a cell can not be treated like a solid object, its behavior can still be explained by the net stresses in each subregion. Regardless of the magnitude of the traction stresses which is proportional to the ligand density, cells move faster when cellular tractions show clear asymmetry across the whole cell as in the case of LLDS. Large nuclear translocation only occurred on LLDS where the rear traction forces are completely relocated around the nuclear region. The relocation of tractions from the rear of the cell to the nuclear region also happened on HLDS, but it was slower due to the high magnitude of traction stresses. This provides a mechanical explanation of why cells migrate faster and in a clear pulsed manner on LLDS compared to HLDS. In addition to the redistribution of cellular traction stresses, we also noticed that, as the rear detached, the shape of nuclei changed from being ellipsoidal to circular. Such nuclear distortion may relate to the structural reorganization of nuclei (26) in response to the overall redistribution of cellular traction stresses. Together with dynamics of cytoskeleton and adhesion molecules, these cellular mechanical changes may stimulate cell migration in certain signalling pathways (27).

Based on all the detailed results, we proposed a traction gradient foreshortening model for fibroblast migration. As shown in Fig. 7, a large nuclear translocation

occurs when rear traction forces are relocated to a posterior nuclear location with concomitant foreshortening of the traction gradient across the cell. This process likely relates to the reorganization of the cytoskeleton, transmembrane adhesion molecules and the nucleus (28). More focal adhesions slide towards the nucleus from the rear (5) and the nucleus become less elongated. Our results suggested that the reinforcing of tractions around the nucleus is another critical step in fibroblast migration besides the active propulsive tractions behind the leading edges and passive resistance at the trailing edges (14).

This traction gradient foreshortening model revealed where fibroblasts reload the rear forces during cell migration, which does not contradict the previous cell migration models such as the frontal towing model (24), but further refines those models. Traction mapping around the nuclear region had, in fact, been shown previously when Munevar et al. presented the color rendering of the normalized shear of a migrating normal 3T3 fibroblast (24). However, it has failed to receive widespread attention, probably due to the lack of an exhaustive temporal dynamics of traction during cell migration. We have addressed these concerns in this report by obtaining high-resolution mapping of the spatiotemporal dynamics of both cellular and nuclear tractions and correlating them with cell motility. Our results are also consistent with previous qualitative studies that report the dynamics of focal adhesions during cell migration, which remain stationary at the leading edge while sliding toward the nucleus at the rear end (5, 6). Our rigorous quantitative analysis suggests that the focal adhesion motility (towards the nucleus) observed at the rear

end of a migrating cell correlates with the relocation of traction stresses from cell rear to a posterior nuclear location. Notably, we find that traction forces at the cell's leading edge remain unchanged, again in agreement with the observed stationary phenotype of focal adhesions at that location (5, 6). Our results also highlight the importance of the perinuclear region during cell migration, which should be considered more carefully in future studies. The sensing mechanism which determines the distribution of nuclear traction stresses may also play a role in nuclear function during mechnotransduction (28) and a number of other molecular events associated with cell migration (29).

This measuring system also affords a tool for detailed study of the effects of other pathological factors on cell migration such as diabetes which affect the chemistry of the binding ligands or the processes regulating focal adhesion assembly. The easily controlled spatial resolution, as illustrated by the inset, indicates that this is a promising method to measure the traction forces when cells are cultured on a surface with submicron-scale resolution, such as the electrospun three dimensional nanofibrous scaffolds (30) that better mimic the natural ECM architecture. The cells themselves can also be included in the FEM model with further understanding of their mechanical properties.

3.5 Conclusion

By using DISC and FEM, we measured the spatiotemporal redistribution of cellular traction stresses (force per area) during fibroblast migration at a submicron level and

correlated it with nuclear translocation, an indicator of cell migration, on a physiologically relevant ECM mimic. We found that nuclear translocation occurred in pulses whose magnitude was larger on the low ligand density surfaces (LLDS) than on the high ligand density surfaces (HLDS). Large nuclear translocations only occurred on LLDS where the rear traction forces completely relocated to a posterior nuclear location, while such relocation took a much longer time on HLDS, probably due to the greater magnitude of traction forces. Nuclear distortion was also observed as the traction stresses redistributed. Our results suggest that the reinforcement of the traction stresses around the nucleus, as well as relaxation of nuclear deformation, are critical steps during fibroblast migration, serving as a speed regulator, which must be considered in any dynamic molecular reconstruction model of tissue cell migration. A traction gradient foreshortening model was proposed to explain how the relocation of rear traction forces leads to pulsed fibroblast migration.

3.6 References

1. Lauffenburger, D. A., and A. F. Horwitz. 1996. Cell migration: A physically integrated molecular process. Cell 84:359-369.
2. Mitchison, T. J., and L. P. Cramer. 1996. Actin-based cell motility and cell locomotion. Cell 84:371-379.
3. Sheetz, M. P., D. P. Felsenfeld, and C. G. Galbraith. 1998. Cell migration: Regulation of force on extracellular-matrix-integrin complexes. Trends Cell Biol. 8:51-54.
4. Geiger, B., and A. Bershadsky. 2001. Assembly and mechanosensory function of focal contacts. Curr. Opin. Cell Biol. 13:584-592.
5. Smilenov, L. B., A. Mikhailov, R. J. Pelham, E. E. Marcantonio, and G. G. Gundersen. 1999. Focal adhesion motility revealed in stationary fibroblasts. Science 286:1172-1174.
6. Wehrle-Haller, B., and B. A. Imhof. 2003. Actin, microtubules and focal adhesion dynamics during cell migration. Int. J. Biochem. Cell Biol. 35:39-50.
7. Beningo, K. A., and Y. L. Wang. 2002. Flexible substrata for the detection of cellular traction forces. Trends Cell Biol. 12:79-84.
8. Dembo, M., T. Oliver, A. Ishihara, and K. Jacobson. 1996. Imaging the traction stresses exerted by locomoting cells with the elastic substratum method. Biophys. J. 70:2008-2022.
9. Dembo, M., and Y. L. Wang. 1999. Stresses at the cell-to-substrate interface

during locomotion of fibroblasts. Biophys. J. 76:2307.

10. Pelham, R. J., and Y. L. Wang. 1999. High resolution detection of mechanical forces exerted by locomoting fibroblasts on the substrate. Mol. Biol. Cell 10:935-945.

11. Tan, J. L., J. Tien, D. M. Pirone, D. S. Gray, K. Bhadriraju, and C. S. Chen. 2003. Cells lying on a bed of microneedles: An approach to isolate mechanical force. Proc. Natl. Acad. Sci. U. S. A. 100:1484-1489.

12. Buguin, A., P. Chavrier, B. Ladoux, O. du Roure, A. Saez, and P. Silberzan. 2005. An array of microfabricated pillars to study cell migration. M S-Med. Sci. 21:765-767.

13. Pelham, R. J., and Y. L. Wang. 1997. Cell locomotion and focal adhesions are regulated by substrate flexibility. Proc. Natl. Acad. Sci. U. S. A. 94:13661.

14. Munevar, S., Y. L. Wang, and M. Dembo. 2001. Distinct roles of frontal and rear cell-substrate adhesions in fibroblast migration. Mol. Biol. Cell 12:3947-3954.

15. du Roure, O., A. Saez, A. Buguin, R. H. Austin, P. Chavrier, P. Siberzan, and B. Ladoux. 2005. Force mapping in epithelial cell migration. Proc. Natl. Acad. Sci. U. S. A. 102:2390-2395.

16. Harris, A. K., P. Wild, and D. Stopak. 1980. Silicone-rubber substrata - New wrinkle in the study of cell locomotion. Science 208:177-179.

17. Ghosh, K., Z. Pan, E. Guan, S. R. Ge, Y. J. Liu, T. Nakamura, X. D. Ren, M. Rafailovich, and R. A. F. Clark. 2007. Cell adaptation to a physiologically

relevant ECM mimic with different viscoelastic properties. Biomaterials 28:671-679.

18. Ghosh, K., X. D. Ren, X. Z. Shu, G. D. Prestwich, and R. A. F. Clark. 2006. Fibronectin functional domains coupled to hyaluronan stimulate adult human dermal fibroblast responses critical for wound healing. Tissue Eng. 12:601-613.

19. Palecek, S. P., J. C. Loftus, M. H. Ginsberg, D. A. Lauffenburger, and A. F. Horwitz. 1997. Integrin-ligand binding properties govern cell migration speed through cell-substratum adhesiveness. Nature 385:537-540.

20. Engler, A., L. Bacakova, C. Newman, A. Hategan, M. Griffin, and D. Discher. 2004. Substrate compliance versus ligand density in cell on gel responses. Biophys. J. 86:617-628.

21. Ghosh, K., X. Z. Shu, R. Mou, J. Lombardi, G. D. Prestwich, M. H. Rafailovich, and R. A. F. Clark. 2005. Rheological characterization of in situ cross-linkable hyaluronan hydrogels. Biomacromolecules 6:2857-2865.

22. Clark, R. A. F., J. Q. An, D. Greiling, A. Khan, and J. E. Schwarzbauer. 2003. Fibroblast migration on fibronectin requires three distinct functional domains. J. Invest. Dermatol. 121:695-705.

23. Guan, E., S. Smilow, M. Rafailovich, and J. Sokolov. 2004. Determining the mechanical properties of rat skin with digital image speckle correlation. Dermatology 208:112-119.

24. Munevar, S., Y. L. Wang, and M. Dembo. 2001. Traction force microscopy of

migrating normal and H-ras transformed 3T3 fibroblasts. Biophys. J. 80:1744-1757.

25. Palecek, S. P., A. Huttenlocher, A. F. Horwitz, and D. A. Lauffenburger. 1998. Physical and biochemical regulation of integrin release during rear detachment of migrating cells. J. Cell Sci. 111:929-940.

26. Dahl, K. N., A. J. Engler, J. D. Pajerowski, and D. E. Discher. 2005. Power-law rheology of isolated nuclei with deformation mapping of nuclear substructures. Biophys. J. 89:2855-2864.

27. Ingber, D. E. 2003. Mechanosensation through integrins: Cells act locally but think globally. Proc. Natl. Acad. Sci. U. S. A. 100:1472.

28. Maniotis, A. J., C. S. Chen, and D. E. Ingber. 1997. Demonstration of mechanical connections between integrins cytoskeletal filaments, and nucleoplasm that stabilize nuclear structure. Proc. Natl. Acad. Sci. U. S. A. 94:849-854.

29. Ridley, A. J., M. A. Schwartz, K. Burridge, R. A. Firtel, M. H. Ginsberg, G. Borisy, J. T. Parsons, and A. R. Horwitz. 2003. Cell migration: Integrating signals from front to back. Science 302:1704-1709.

30. Ji, Y., K. Ghosh, X. Z. Shu, B. Q. Li, J. C. Sokolov, G. D. Prestwich, R. A. F. Clark, and M. H. Rafailovich. 2006. Electrospun three-dimensional hyaluronic acid nanofibrous scaffolds. Biomaterials 27:3782-3792.

3.7 Figure Captions

Figure 3. 1 The effects of ligand density (cell-substrate adhesion) on fibroblast migration and morphology. (A) Mean migration speed of cells on low ligand density surfaces (LLDS, n = 26) and on high ligand density surfaces (HLDS, n =24). (B) Phase images of a typical cell on LLDS (left) and HLDS (right). The white solid lines show the major and the minor length of each cell and its nucleus. (C) Aspect ratio (defined as the ratio of the major to the minor length) of cells and their nuclei, and cell area on LLDS (n = 19) and HLDS (n = 23). Error bars represent s.e.m.

Figure 3. 2 Focal adhesion distributions as a function of FN density. (A) Focal adhesions in cells grown on tissue culture dishes coated with low and high densities of FN, as visualized by vinculin staining. (B) Total number of vinculin-positive focal adhesions per cell. (C) The front to rear ratio of the number of vinculin-positive focal adhesions in a cell. n = 7 and 9 for low and high FN density surfaces, respectively. Error bars represent s.d.

Figure 3. 3 The distribution of nuclear translocation as a function of ligand density. (A) Magnitude distributions of nuclear translocations in every 15 min interval over an hour, divided into three groups of different size: large: > 10 μm, medium: 5~10 μm, and small: < 5 μm. (B) Number distribution of large nuclear translocation for each cell over an hour, from minimum 0 to maximum 4 in an hour. (C) Time distribution of large nuclear translocation in 15 min interval over an hour. n = 26 and 24 for LLDS

and HLDS, respectively. Error bars represent s.e.m.

Figure 3. 4 Displacement map and traction field obtained by using DISC technique and FEM. (A) Vector map determined using DISC technique, representing the displacement generated by a typical migrating cell on LLDS. Vector density is diluted by 1: 160 to make the map clear. Arrows show the direction and relative magnitude of the displacement field of the hydrogel surface beneath the attached fibroblast. The phase contrast image from DIC is superimposed to provide the outline of the cell and its nucleus. (B) Traction field calculated by FEM based on the displacement data from DISC. In the color map, arrows show the direction and relative magnitude of the stress field exerted by the attached fibroblast; colors show the absolute magnitude of the stress field in Pa (see color bar). Cellular traction stresses concentrate in three distinct regions, the front, the nuclear and the rear of the cell.

Figure 3. 5 Time sequence of displacement and traction fields generated by a migrating fibroblast on LLDS. The left column is displacement maps quantified by DISC. Arrows show the direction and relative magnitude of the displacement field exerted by the attached fibroblast; colors show the absolute magnitude of the displacements in μm (see color bar).The intersection of dashed lines shows the initial position of the nucleus. The right column is traction stress distributions obtained from FEM. The directions of net stresses in five subregions exerted by the cell on LLDS are represented by the white arrows, including rearward traction stresses (a) and (b) behind the leading edges, rearward and forward traction stresses around the front and

the rear edges of the nucleus (c and d), and forward traction stress near the trailing edge (e). Colors show the absolute magnitude of the stress field in Pa (see color bar). Inset: high resolution image of traction stresses near the initial leading edge.

Figure 3. 6 Time sequence of displacement and traction fields generated by a migrating fibroblast on HLDS. The left and right columns are displacement maps and traction fields calculated by DISC and FEM, respectively. Arrows in displacement maps show the direction and relative magnitude of the displacement field exerted by the attached fibroblast; colors show the absolute magnitude of the displacements in μm (see color bar). The intersection of dashed lines in displacement maps shows the initial position of the nucleus. White arrows a-e in traction field indicate directions of net stress in five sub-regions similar to those in LLDS. Colors in traction fields show the absolute magnitude of the stress field in Pa (see color bar).

Figure 3. 7 (A) and (B) are the temporal redistribution of net stresses in each subregion and corresponding nuclear translocation on LLDS and HLDS. Net stresses in the five subregions (a-e in Figure 5 and 6) are plotted as a function of Nuclear Traction Stresses and Distortion during Cell Migration 24 time for either LLDS (left) or HLDS (right) in (A), where +/- respectively denotes rearward and forward stresses which propel or resist forward motion. Nuclear translocation distances in every 15 min interval are plotted as a function of time for either LLDS (left) or HLDS (right) in (B). (C) Total net stress and mechanical work done by the cell evaluated by stain energy stored in the substrate are plotted as a function of time for either LLDS (left)

or HLDS (right). (D) Aspect ratio of the nucleus as a function of time for either LLDS (left) or HLDS (right).

Figure 3. 8 (A) Magnitude distributions of cellular traction stresses on LLDS and HLDS plotted in 3D. The blue arrows show the traction gradients across the entire cells. (B) and (C) are the average mechanical work done by the cell and total nuclear translocation over an hour observation period on LLDS and HLDS, averaged from 3 cells. Error bars represent s.d.

Figure 3. 9 The ratio of the net rear stress to the net nuclear rear stress as a function of time.

Figure 3. 10 Traction gradient foreshortening model for fibroblast migration. The cell stretches out when the parallel stress fibers pull laterally on the confined nucleus from both front and rear sides, inducing the nuclear elongation. As the focal adhesions slide from the cell rear to the nuclear rear, the rear traction stresses relocate at a posterior nuclear location, resulting in the relaxation and translocation of the nucleus. Red arrows show the traction stresses exerted on the substrate through focal adhesions and red curves show their magnitude. The green arrow shows the traction gradient across the cell which becomes shorter as the rear traction stresses relocate around the nucleus.

3.8 Figures

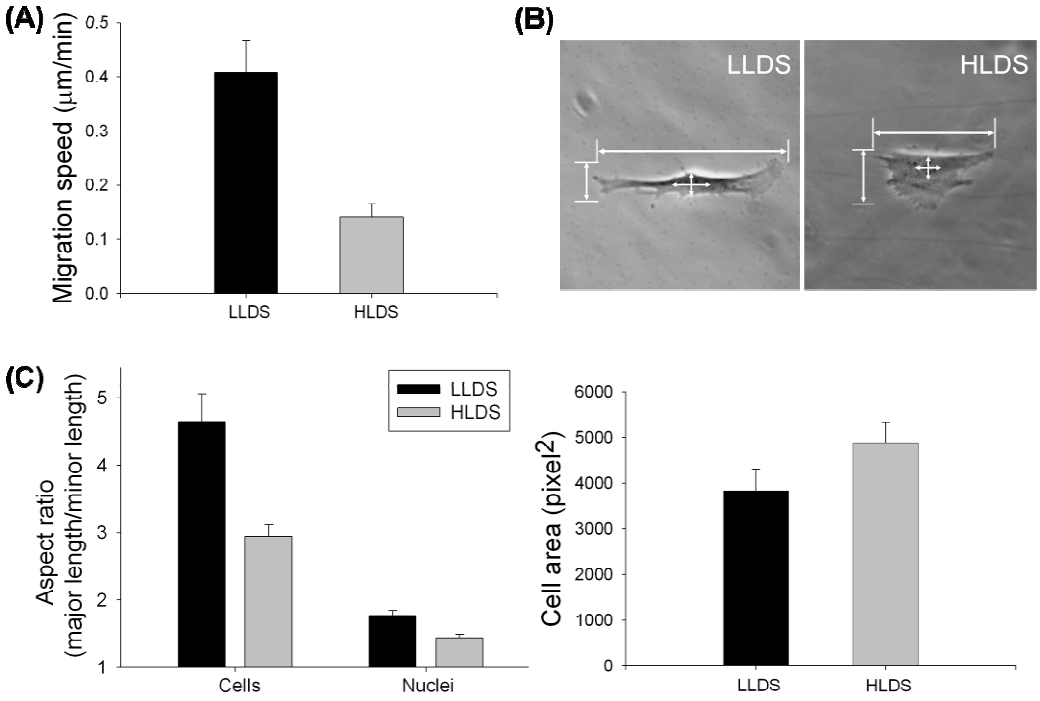

Figure 3.1

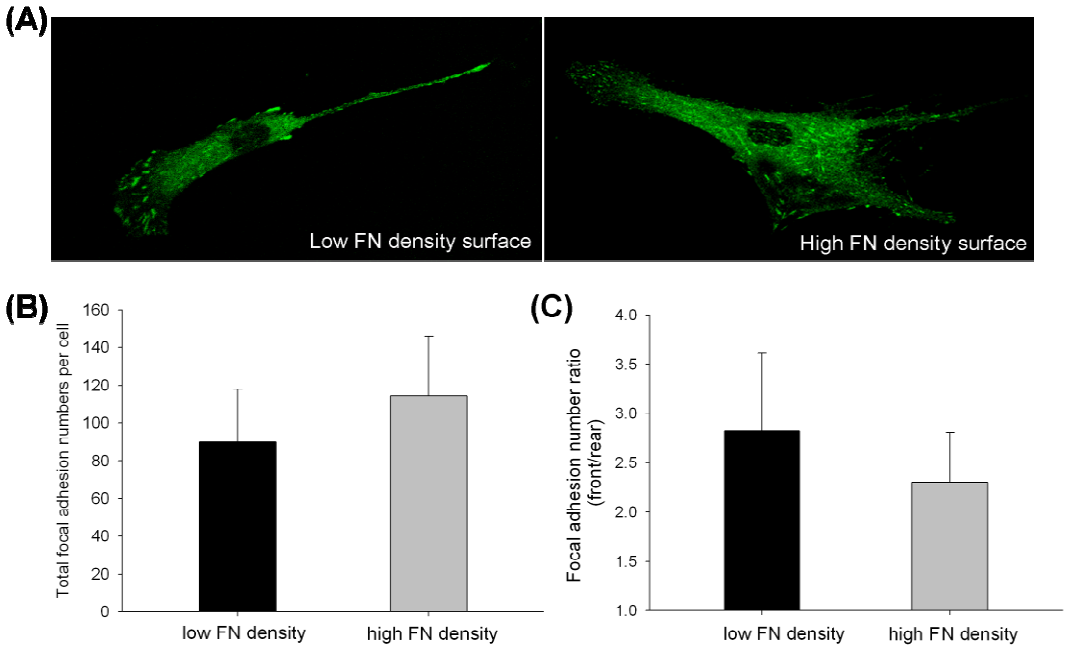
(A)
Low FN density surface
High FN density surface
(B)
Total focal adhesion numbers per cell
160
140
120
100
80
60
40
20
0
low FN density
high FN density
(C)
Focal adhesion number ratio (front/rear)
4.0
3.5
3.0
2.5
2.0
1.5
1.0
low FN density
high FN density

Figure 3.2

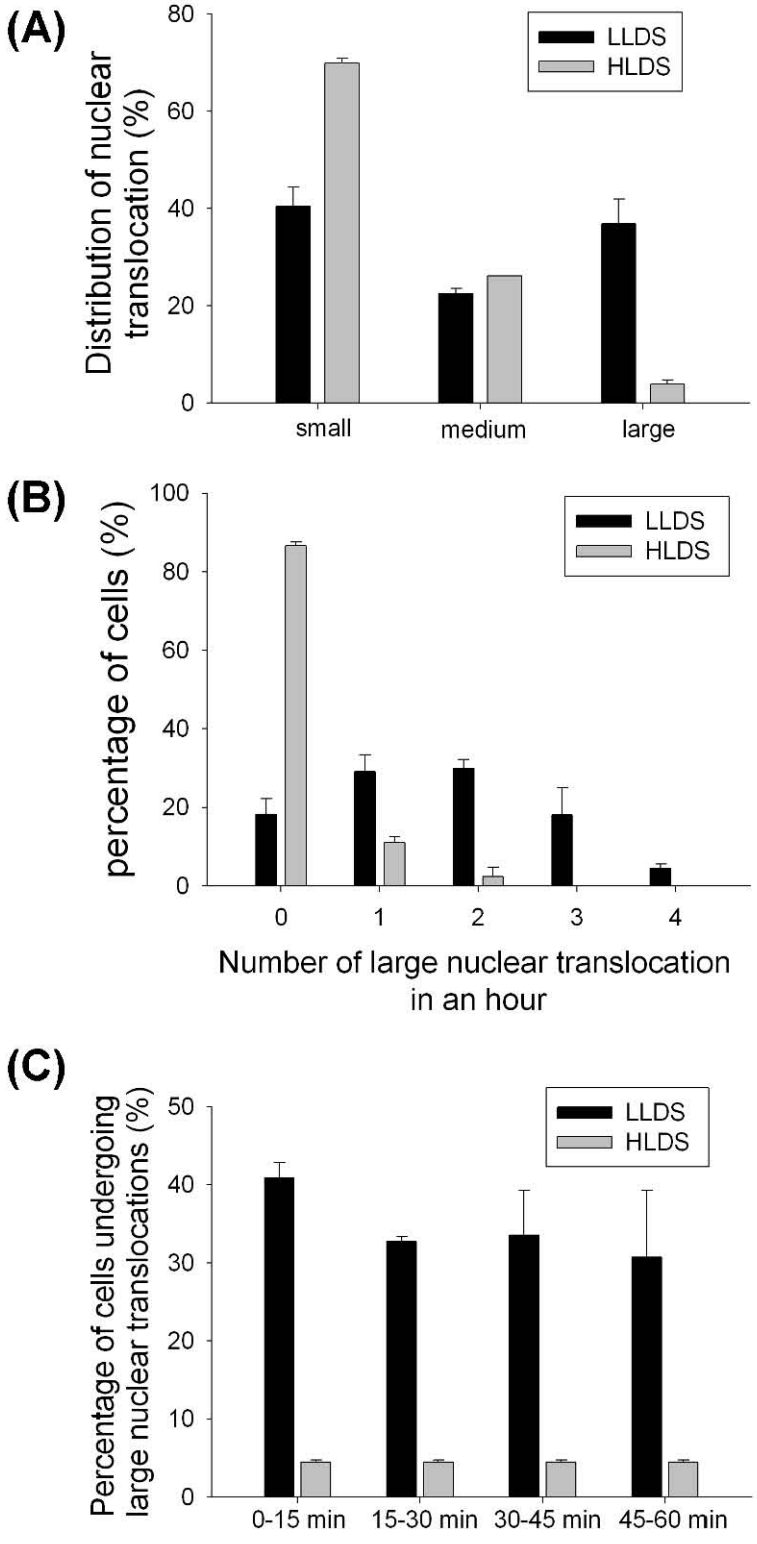
(A)
Distribution of nuclear translocation (%)
80
60
40
20
0
LLDS
HLDS
small
medium
large
(B)
percentage of cells (%)
100
80
60
40
20
0
LLDS
HLDS
0
1
2
3
4
Number of large nuclear translocation in an hour
(C)
Percentage of cells undergoing large nuclear translocations (%)
50
40
30
20
10
0
LLDS
HLDS
0-15 min
15-30 min
30-45 min
45-60 min

Figure 3.3

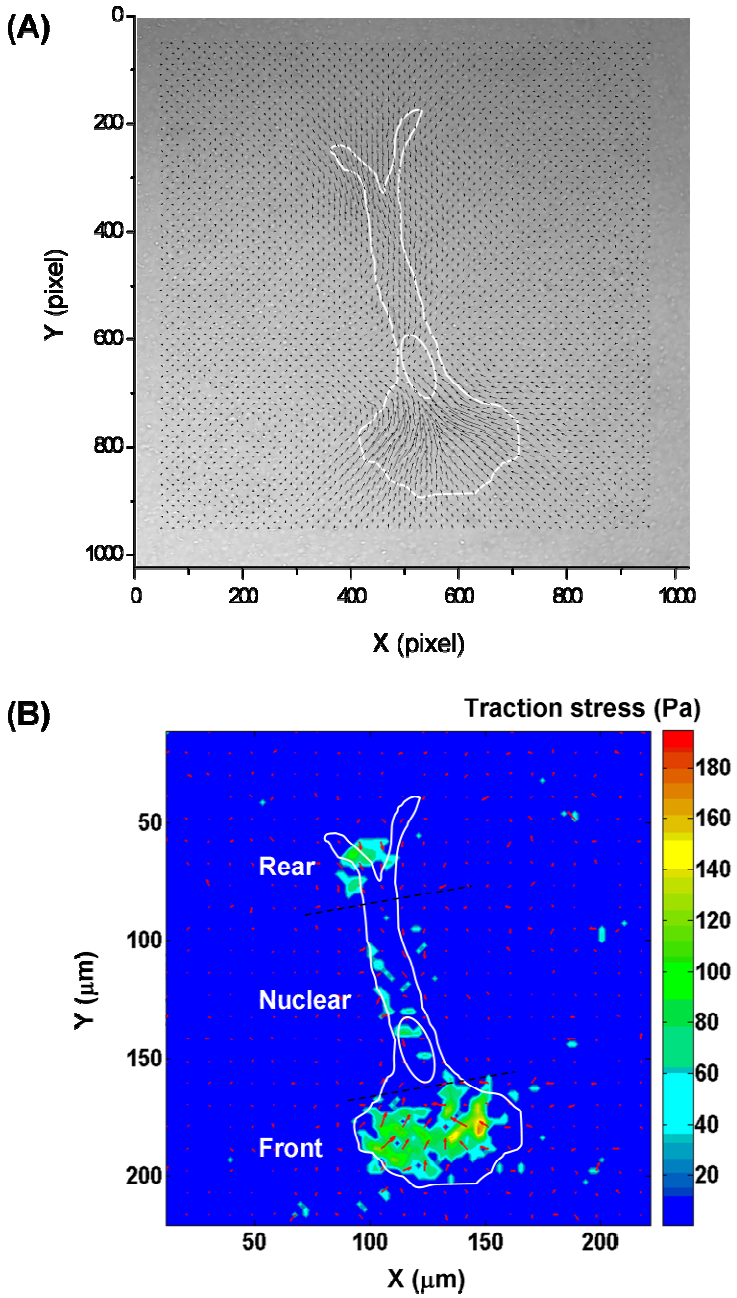
(A)
Y (pixel)
X (pixel)
0
200
400
600
800
1000
(B)
Traction stress (Pa)
180
160
140
120
100
80
60
40
20
Rear
Nuclear
Front
Y (μm)
X (μm)
50
100
150
200

Figure 3.4

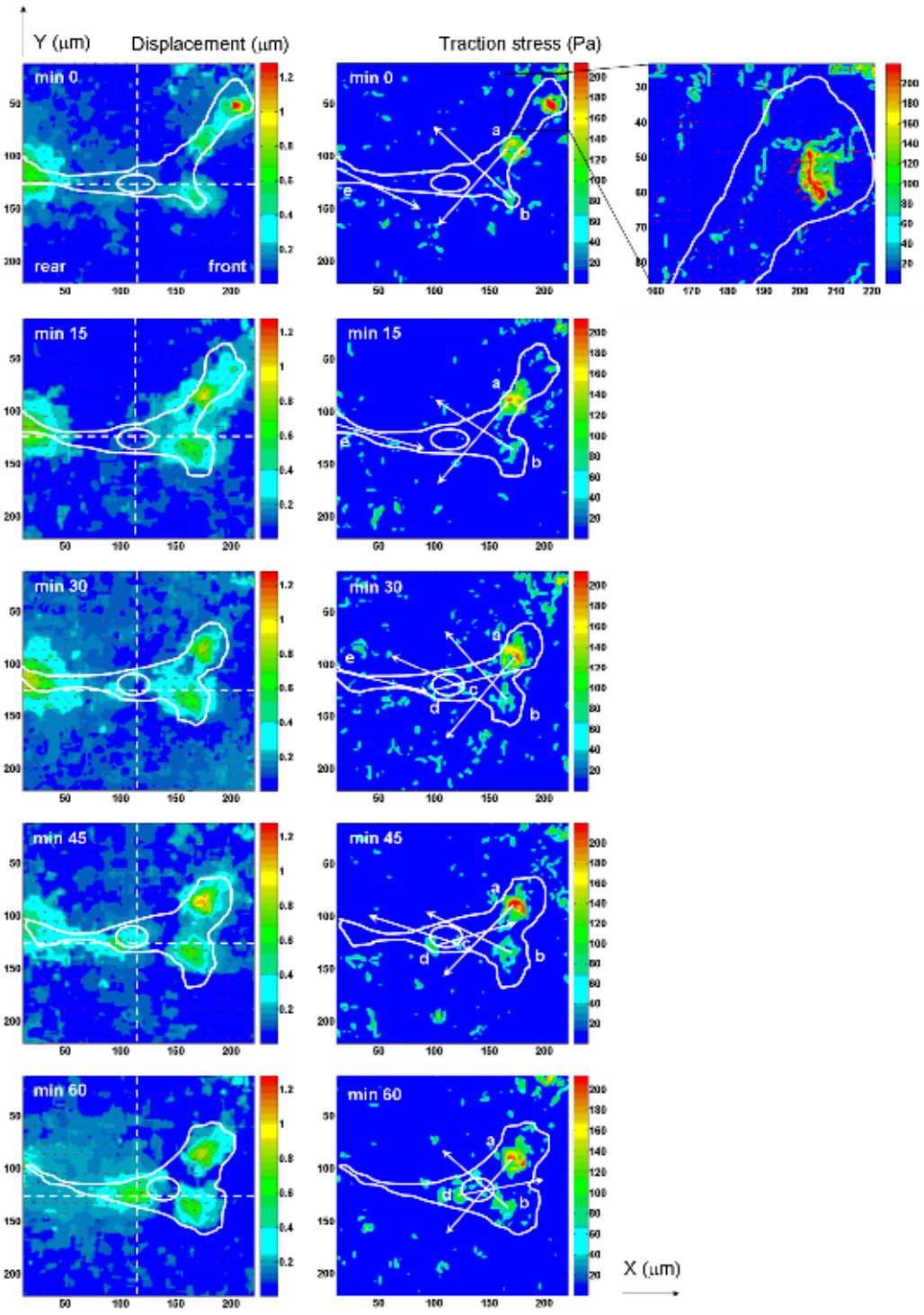
Y (μm)
Displacement (μm)
Traction stress (Pa)
min 0
rear
front
min 15
min 30
min 45
min 60
a
b
d
e
X (μm)

Figure 3.5

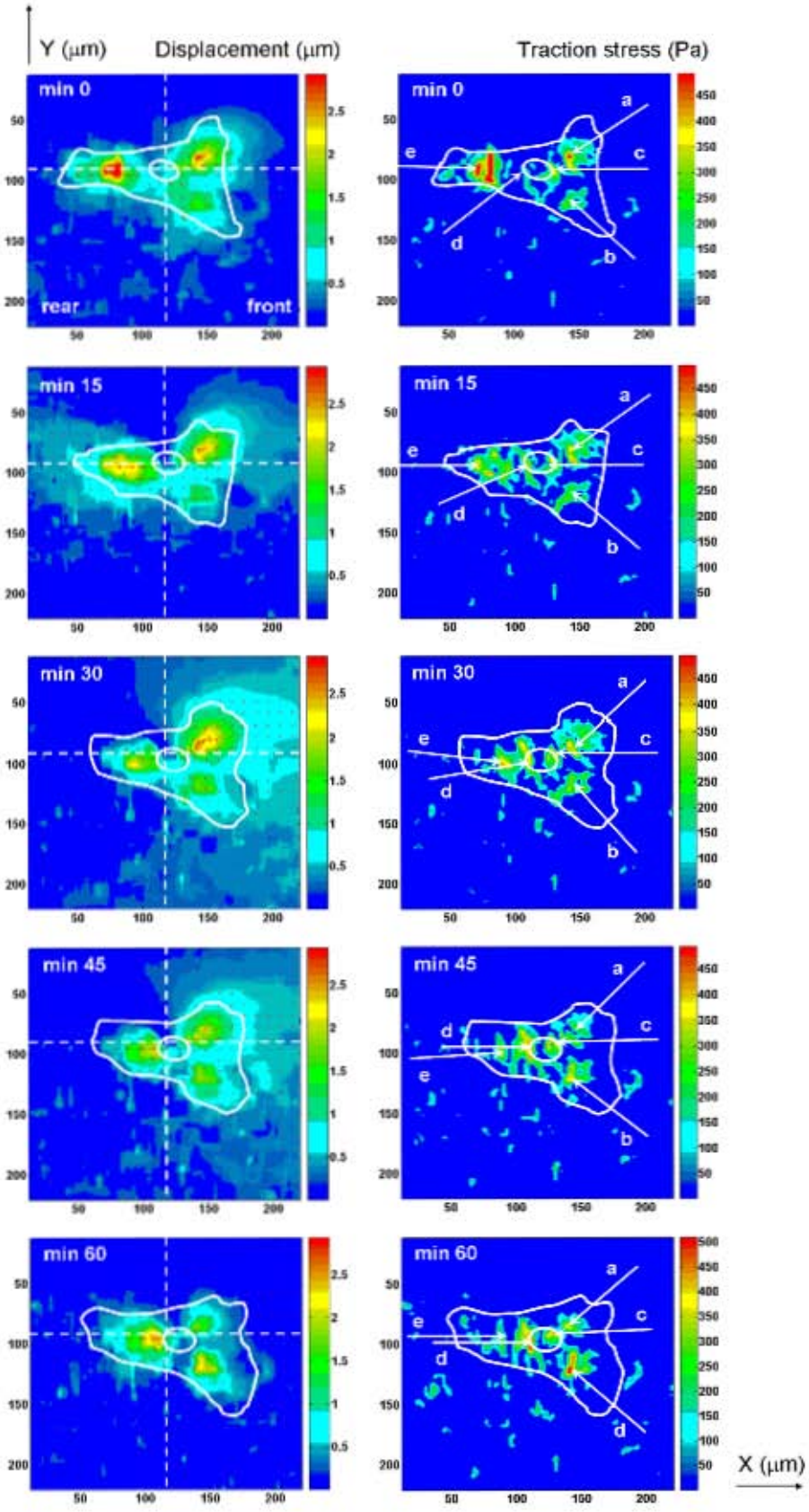
Y (μm)
Displacement (μm)
Traction stress (Pa)
min 0
min 15
min 30
min 45
min 60
rear
front
a
b
c
d
e
X (μm)

Figure 3.6

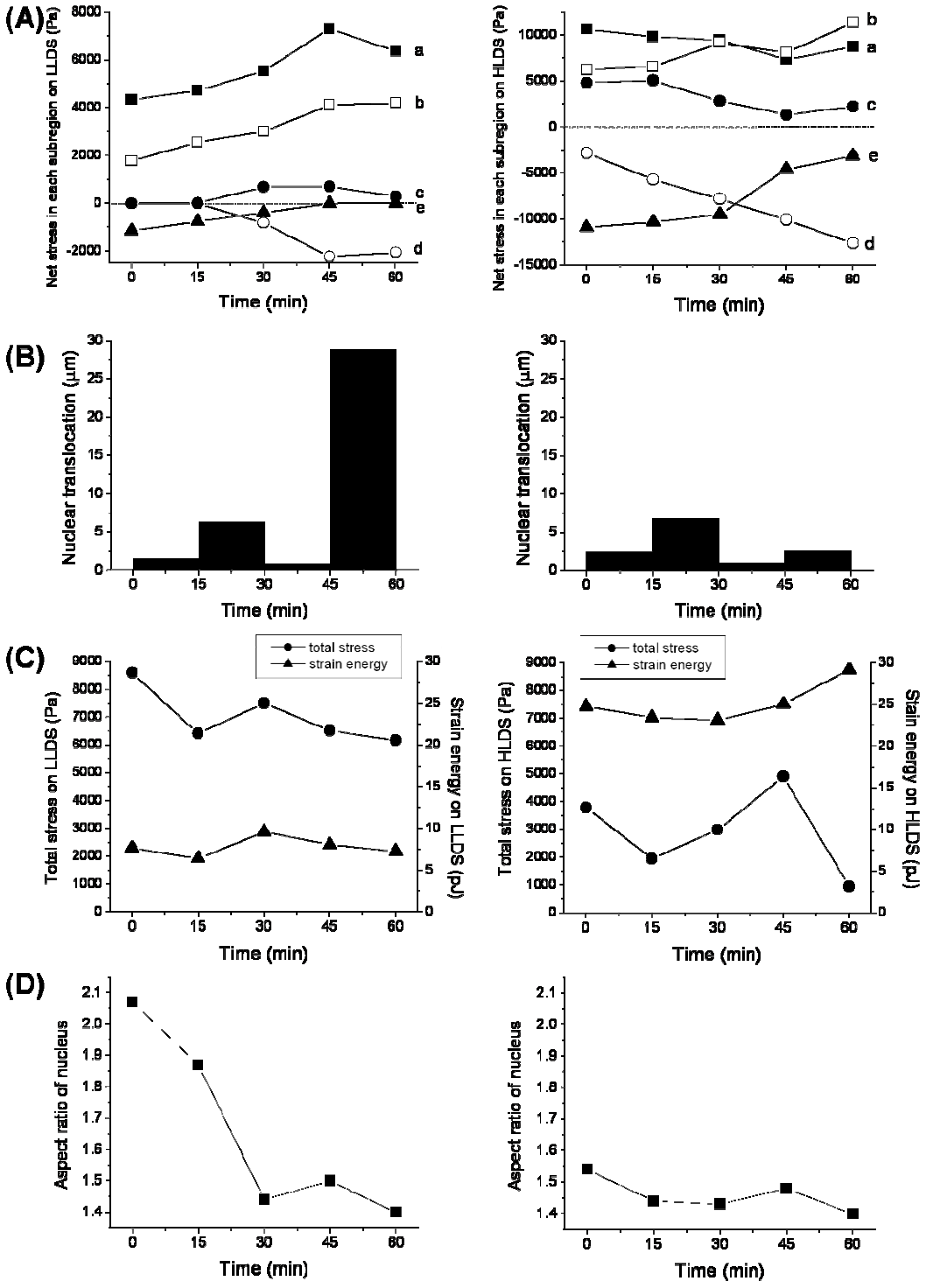
(A)
Net stress in each subregion on LLDS (Pa)
Time (min)
a
b
c
d
e
Net stress in each subregion on HLDS (Pa)
Time (min)
(B)
Nuclear translocation (μm)
Time (min)
Nuclear translocation (μm)
Time (min)
(C)
total stress
strain energy
Total stress on LLDS (Pa)
Strain energy on LLDS (pJ)
Time (min)
total stress
strain energy
Total stress on HLDS (Pa)
Stain energy on HLDS (pJ)
Time (min)
(D)
Aspect ratio of nucleus
Time (min)
Aspect ratio of nucleus
Time (min)

Figure 3.7

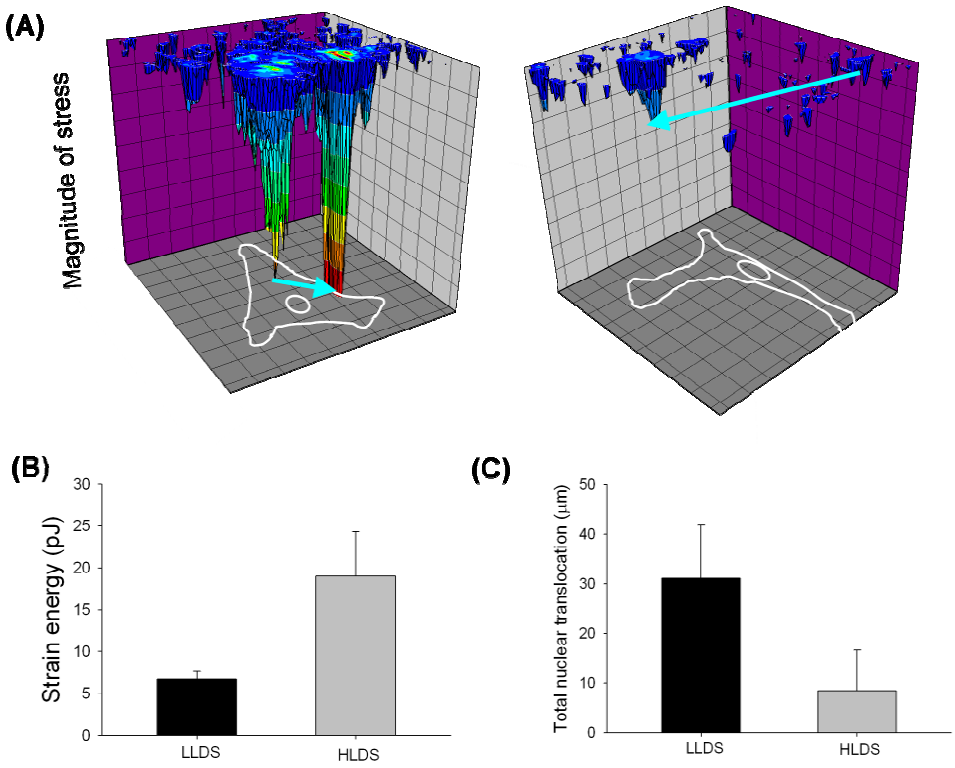
(A)
Magnitude of stress
(B)
Strain energy (pJ)
30
25
20
15
10
5
0
LLDS
HLDS
(C)
Total nuclear translocation (μm)
50
40
30
20
10
0
LLDS
HLDS

Figure 3.8

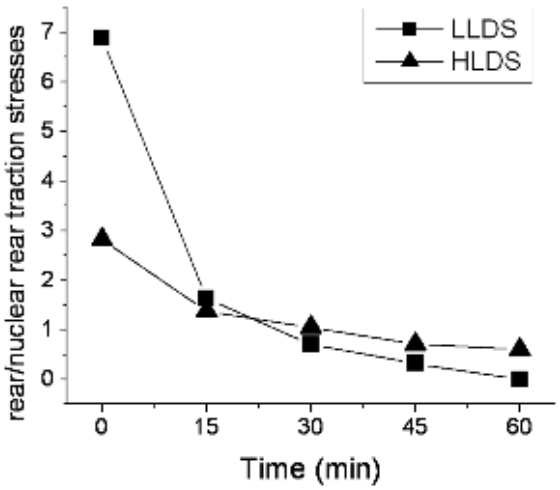
LLDS
HLDS
rear/nuclear rear traction stresses
0
1
2
3
4
5
6
7
0
15
30
45
60
Time (min)

Figure 3.9

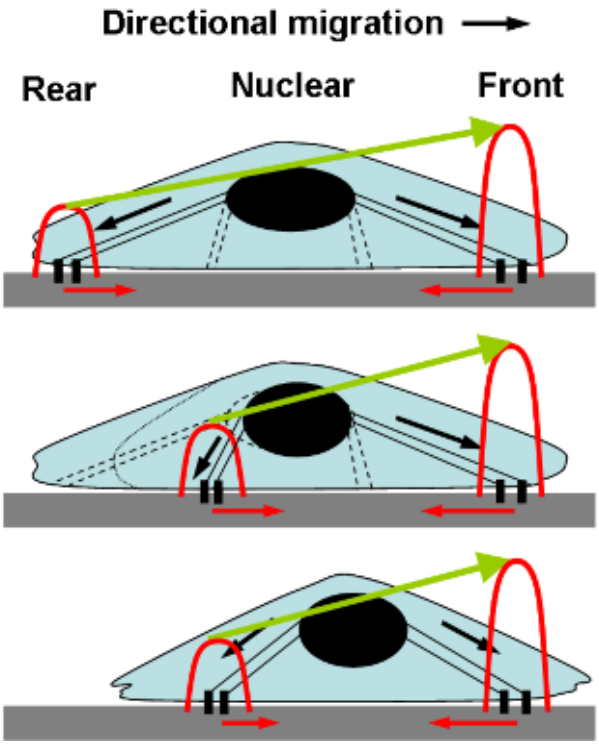

Figure 3.10

Cell number on LLDS	Maximal net stress at rear (σ_{rear} : Pa)	Maximal net stress at nuclear rear ($\sigma_{nuclear}$: Pa)	Ratio of σ_{rear} / $\sigma_{nuclear}$
1	5.3×10^{2}	1.1×10^{3}	0.48
2	4.9×10^{2}	6.1×10^{2}	0.80
3	1.4×10^{3}	1.0×10^{3}	1.4
Mean	8.1×10^{2}	9.0×10^{2}	0.89
SD	5.1×10^{2}	2.6×10^{2}	0.46
Cell number on HLDS			
1	1.2×10^{4}	1.7×10^{4}	0.70
2	4.8×10^{3}	8.1×10^{3}	0.59
3	2.5×10^{4}	2.1×10^{4}	1.2
Mean	1.4×10^{4}	1.5×10^{4}	0.83
SD	1.0×10^{4}	6.6×10^{3}	0.32

Table 3. 1 The maximal rear stresses and maximal nuclear rear stresses for 3 individual cells on LLDS and HLDS.

Chapter 4

En masse versus single cell migration

Preface

This chapter is in preparation for submission as:

Pan, Z., K. Ghosh, V. Hung, L. Macri, R.A.F. Clark, and M.H. Rafailovich. Cell density modulates cell migration: *en masse* versus single cell migration.

Original contribution: Data for Figure 4.2(B), 4.3, 4.5 - 4.8

In collaboration: Data for Figure 4.1, 4.2(A), 4.4

4.1 Introduction

To maximize cell migration is a major design objective for development of effective tissue-engineered constructs. It has been well-known that both optimal bioactivity and mechanics are required to achieve desired results (1, 2). Much knowledge of the mechanism of cell migration has been accumulated through previous observations reported by various research investigators (2-7). Most of these studies are based on single cells, which are fundamentally important and relatively easy to handle. However, during many physiological processes such as embryonic development and wound repair, it is *en masse* cells' behavior instead of single cells' (8). Thus it raises a

new question – whether multi-cells and single cells work in the same way. We studied *en masse* versus single cell migration in this chapter to explore whether cell density is another factor to modulate cell migration in a tissue-engineered environment.

In this study, both single and *en masse* cell migration on HA/FNfds hydrogel surfaces were time-lapse imaged and quantitatively analyzed as functions of substrate stiffness and adhesiveness. *En masse* cell migration was evaluated using agarose droplet migration assay. The results indicated that migrating cells respond differentially to substrate properties depending on whether they move as unicellular or multicellular units, with the preferential phenotype being mediated greatly by the size and distribution of focal adhesions. Since the differences in focal adhesion patterning predicted distinct cell-substrate interactions (9-11), substrate deformations generated by *en masse* cells were also measured to investigate whether the *en masse* migrating cells influence the behavior of neighboring cells by altering local substrate mechanics.

4.2 Materials and Methods

4.2.1 Preparation of hydrogel substrates

HA/FNfd hydrogel substrate were synthesized as reported previously (12). Briefly, RGD-containing C domain were coupled to the crosslinker poly(ethylene glycol) diacrylate (PEGDA) (Nektar Therapeutics, Huntsville, AL) in PBS to form PEGDA-C conjugates with different bulk densities. Then these conjugates were mixed with 1.25%(w/v) thiol-functionalized HA (HA-DTPH) in serum free-DMEM (SF-DMEM, Sigma, St. Louis, MO) at volume ratio of 1:4 to obtain HA/FNfd hydrogels that were

seeded in 35-mm tissue culture dishes. Final concentration of HA-DTPH was always 1%(w/v) in the hydrogels. The stiffness of these hydrogels was modulated by altering the concentration of PEGDA solutions from 4.5% to 1.5% and 0.75% (w/v) which resulted in crosslinking ratio from 2:1 to 6:1 and 12:1 and shear storage moduli of 4270 Pa, 550 Pa and 95 Pa, respectively, as measured by oscillatory shear rheometry (13).

4.2.2 Cell culture

Primary AHDFs were obtained from a 31 years old Caucasian Female (CF-31, Clonetics, San Diego, CA) were used between passages 5 and 13. The cells were routinely cultured in Dulbecco's Modified Eagle's Medium (DMEM), supplemented with 10% fetal bovine serum and 1% Penicillin, Streptomycin and L-glutamine, in a 37 °C, 5% CO_2, 95% humidity incubator (Napco Scientific Company, Tualatin, OR).

4.2.3 Agarose droplet migration assay

After reaching 80-95 % confluence, cells were detached using 0.05% Trypsin. Then full-DMEM was used to stop trypsinization. After rinsed once using 2%(w/v) bovine serum albumin (BSA) in SF-DMEM, cells were resuspended in 0.2% agarose solution in SF-DMEM to obtain a final cell concentration of $1.5x10^7$ cells/ml. 1.25 μl agarose droplets with cells were gently placed onto HA/FNfd hydrogel in 24-well dishes. After the dishes were covered and incubated at 4 ^oC for 20 minutes to allow the agarose droplets to set, SF-DMEM with 30 ng/ml recombinant platelet derived growth factor-BB (PDGF) (ZymoGenetics, Seattle, WA) was added carefully. Then, the

samples were incubated at 37 ^{o}C for 18 hours before staining and imaging. Each experimental group contained five replicates.

The cells were fixed with 3.7 % formaldehyde in PBS and left for 10 minutes at room temperature. Afterwards they were stained with filtered 0.1 % crystal violet in 200 mM boric acid (pH 8.0) at room temperature for another 10 minutes. The cells were then rinsed carefully and thoroughly with PBS to remove background dye from plate. 0.5 ml of PBS was then added to prevent drying.

Samples were imaged using a Nikon SMX800 zoom stereomicroscope (Japan) with a Diagnostic Instruments Spot RT camera Attachment (Sterling Heights, MI). Images were captured and analyzed with Spot 3.0 software. Migration area was determined by outlining the boundaries of the fibroblast migration and the agarose droplet. The area of migration (in square pixels) was then determined by the formula *Total Area - Area of Droplet*. In addition, ANOVA tests were run on the data to determine whether the variations between conditions were random.

4.2.4 Time-lapse measurement of cell migration

A low density of cells (~500 /cm^2) and agarose droplets with cells were respectively seeded onto HA/FNfd hydrogel in 35 mm cell culture dishes at the same time. After added serum-free DMEM with 30 ng/ml PDGF and incubated at 37 °C for 6/14/25 hours, time-lapse phase images of the cells were recorded every 15 min for up to 60 min with a MetaMorph®-operated CoolSNAP™ HQ camera (Universal Imaging Corporation, Downingtown, PA) attached to a Nikon Diaphot-TMD inverted

microscope fitted with a 37 ^{o}C stage incubator and a 10x objective lens. Using MetaMorph software, migration speed was determined from the time-lapse images by tracking the distance covered by the center of a cell nucleus over every 15 minutes in one hour. The sample size *n* used was 5~10 cells/field x 5 fields/replicate x 3 replicates and 10~20 cells/field x 3 fields/droplet x 3 droplets, respectively, for single cells and *en masse* cells. Only single cells without cell-cell contact were chosen to measure single cell migration speed. Only cells migrating on the edge of droplet were tracked for evaluation of *en masse* cell migration.

4.2.5 Visualization of focal adhesions and actin cytoskeleton

Since immunofluorescent staining of vinculin-containing focal adhesions was difficult to perform in cells plated on the hydrogels (owing to non-specific absorption of antibodies within hydrogels that led to a high fluorescence background), we coated glass cover slip in 24-well dishes with 30 μg/ml FN solution overnight at room temperature, and then blocked non-specific binding using 2% (w/v) BSA at room temperature for 2 hours. Each dish was rinsed three times with PBS before an agarose droplet with cells was seeded on the center of each glass cover slip. After the droplets were refrigerated at 4 ºC for 10 minutes and added serum-free DMEM with 30 ng/ml PDGF, they were incubated at 37 ^{o}C for different incubation time, 6/15/24 hours, respectively. The cells were then fixed with 4% paraformaldehyde in PBS for 15 minutes, permeabilized with 0.4% Triton in PBS for 5 minutes, and blocked with 2% BSA in PBS for 30 minutes at room temperature. Focal adhesions were visualized by

immunostaining for vinculin, where anti-vinculin primary antibody (Sigma, V9131) was incubated with cells at 1:600 dilution for 1 hour at room temperature , followed by incubation with Oregon Green 488 goat anti-mouse secondary antibody (Invitrogen, O11033) at a 1:800 dilution for 1 hour. Then F-actin cytoskeleton was stained by TRITC-phalloidin (Alexa Fluor 546, Invitrogen, A22283). After washing, cells were kept in PBS at 4 ^{o}C before imaging. Then a Leica TCS SP2 laser scanning confocal microscope Leica Microsystems) with a 40x oil objective lens was used to image cells on the edge of droplets. The number and size of vinculin-containing focal adhesions were quantified using ImageJ (NIH).

4.2.6 Substrate deformation quantification using DISC

In order to measure substrate deformation generated by en masse cell migration, fluorescent beads (40 nm diameter, Molecular Probes, Eugene, OR) were sonicated and suspended uniformly at a concentration of 5%(w/v) in HA solution prior to gelation and served as trackers. Agarose droplets with cells were seeded onto HA/FNfd hydrogel in 35 mm cell culture dishes under the same conditions as cell migration experiments. After 6/15/24 hours' incubation at 37 ^{o}C, distribution of fluorescent beads and cells in the field of interest were captured by Leica TCS SP2 laser scanning confocal microscope with a 20x water objective lens and a DIC lens, respectively, before and after separating cells from the substrate by the treatment with trypsin+EDTA. Using optimized DISC technique (14), the displacements of the substrate surface can be quantitatively determined by comparing the distribution

change of the embedded beads. In order to highlight the local displacement generated by cells on the edge of droplets, radial displacements produced by the droplet were removed following the diffusion gradient.

4.3 Result and Discussion

4.3.1 *En masse* versus single cell migration as function of substrate stiffness and adhesiveness

Using agarose droplet migration assay, micro-sized agarose droplets with high cell concentration (1.5 x 10^7 cells/ml) were seeded on hydrogel substrates with different stiffness and ligand density. After 18 hours' incubation at 37 ^{o}C, *en masse* cell migration was evaluated by the out-migrating area covered by cells migrating out of the agarose droplet. As shown in Fig. 4.1(A), *en masse* cells migrate much better with increasing stiffness. As the crosslinking ratio changed from 12:1 to 6:1 and 2:1, en masse cell migration increased up to 260 % and 560 % of that on 12:1 substrate, which showed completely different trend from single cell migration with the same conditions and incubation time as shown in Fig. 4.1(B). Besides, on stiff substrates with the same crosslinking ratio of 2:1, *en masse* cell migration didn't show significant difference as the density of C domain increased from 0.05 μM to 0.26μM and 0.52 μM, while single cell migrated much slower with higher ligand densities (substrate adhesiveness), as shown in Fig. 4.2.

These results clearly showed that *en masse* cells demonstrated different responses to their microenvironment from single cell. Particularly, the substrate mechanics itself

can dramatically regulate *en masse* cell behavior. When cells move as multicellular units, they are more sensitive to the substrate stiffness rather than the adhesiveness.

4.3.2 *En masse* cell migration as function of incubation time (cell density)

Since cell density is the only difference between en masse and single cells, in order to understand *en masse* cell behavior, time-lapse experiment was performed to study *en masse* cell migration from the same agarose droplet after different incubation time (6/15/24 hours) which resulted in different cell densities as well as single cell migration (Fig. 4.3). When cells radially migrate out, the farther they migrate from the agarose droplet, the lower cell density becomes. Fig. 4.4(A) is a schematic of cells migrating outward from the agarose droplet with r_x, r_y and s shown the distance from the nucleus of the cell to the nuclei of neighboring cells and the distance from the droplet. The average distance s is plotted as function of incubation time in Fig. 4.4(B), where the slope decreased with longer incubation implying slower migration. This is consistent with the results of time-lapse measurement in Fig. 4.3(B), where it is noticed that after 24 hours en masse cell migration speed get closer to single cell migration. r_x and r_y are also plotted vs. average migration speed at these three time points as shown in Fig. 4.4(C). It is clear that when cells get away from each other, they move slower.

4.3.3 Focal adhesion distribution change along with different incubation time (cell density)

Our results demonstrated that cell density is another important parameter to modulate

cell migration besides substrate properties. How cell density influence cell behavior is not clear yet. A lot of previous studies have investigated cadherin-mediated cell-cell contacts (15, 16), the dynamic interactions between cadherins and cytoskeleton (17, 18), and the coordinated interplay between cell-cell and cell-substratum adhesion (19). All these partly provide evidence that cell density may influence cell behavior by altering cell-cell contacts. However, no matter what the cell-cell interactions may be, the cell migration is essentially dependent on cell-substrate interactions. And therefore, we performed further studies on the cell-substrate adhesions.

Vinculin-positive focal adhesions were stained and imaged together with F-actin cytoskeleton after different incubation time (showing different cell densities) as shown in Fig. 4.5. In this figure, we can see that both the distribution of focal adhesion and the organization of actin cytoskeleton changed significantly with different cell densities. By quantifying the distribution of vinculin-positive focal adhesions, we noticed that although the total number of focal adhesion is pretty consistent (Fig. 4.6(A)), the front to rear ratio dramatically decreased with longer incubation time and lower cell density. After 24 hours' incubation as cells almost become single ones, their front to rear ratio of focal adhesion is close to 1 as shown in Fig. 4.6(B), which means the polarity of cells get impaired and they are almost balanced as unicellular units. At the same time, the size of focal adhesion increased almost 3 times from beginning as shown in Fig. 4.6(C). Since the size of focal adhesion controls the formation of actin stress fibers and consequent cell contractility (20), the results indicated larger cellular traction forces applied through each focal

adhesion and stronger cell adhesion. Combined with the mechanical results of single cell migration, the decreased polarity and the stronger cell adhesion together also explained why *en masse* cells migrate slower as their density gets lower.

4.3.4 Substrate deformation generated by *en masse* migrating cells

Although it is difficult to directly measure the traction forces generated by *en mass* cells, the substrate deformation induced by them can be quantified with DISC technique. And since the cell migration are relatively slow process (hours) and cellular traction forces are very small (nN), the hydrogel can be assumed as elastic substrates. Thus, the cellular traction forces applied on the surface can be qualitatively represented by the hydrogel deformation.

As shown in Fig. 4.7, with longer incubation time, cells generated larger displacements on the hydrogel, indicating that the hydrogel support stronger cell adhesion. This is consistent with the results of focal adhesion distribution. Further more, we noticed an interesting phenomenon by comparing the cell location with substrate deformation: cells behind prefer to follow the direction of pioneer cells, which is probably by tracking the deformation generated by the pioneer ones. Actually, this may also help to explain why cells migrate more radially on hydrogel than on glass. A large amount of cells beneath the droplet attaching on the hydrogel apply large forces which generate radial displacement around the droplet and induce cell migration along all the directions, while cells can not generate displacement on rigid substrate like glass at all and they migrate more randomly once they leave the droplet.

Similar measurement was performed on softer substrate with crosslink ratio of 6:1. As shown in Fig. 4.8, the maximal displacement generated on this soft substrate is a little smaller that that on stiffer substrate with crosslink ratio of 2:1, although single cells can produce larger deformation on softer substrate (see Fig. 2.2(A)). We also noticed that this displacement is generated by much fewer cells. In other words, fewer cells can migrate outward from the droplet onto the soft substrate probably due to the weakness of the substrate which has smaller yield point (13). In previous studies on single cells, we have known that cells can sense and response to the mechanics of the substrate. They apply larger traction forces on stronger substrate, while they limit their traction forces on weak substrate. All together, our results imply that *en masse* cells migrate more poorly on softer hydrogels is because these substrates can not support large traction forces generated by as many cells as on stiffer substrates.

4.4 Conclusion

In this study, we demonstrated that cell density is another crucial parameter to determine cell migration besides substrate properties. Compared with single cells, e*n masse* cell migration is more sensitive to substrate mechanics than adhesiveness. And for dermal fibroblasts, cell density modulates cell migration by influencing cell-substrate interactions. By measuring the substrate deformation generated by *en masse* cells, we also noticed that the *en masse* migrating cells influence the behavior of neighboring cells by altering local substrate mechanics. Cells behind can track the migration of pioneer cells by detecting the displacement generated by those cells on

the flexible substrate. At the same time, the substrate has to be strong enough to support large traction forces applied by multicellular adhesion. In summary, we have showed that the mechanotransduction between cells and ECM plays a critical role in *en masse* cell migration as well as in single cell migration. Considering the importance of *en masse* cell migration in many physiological processes such as embryonic development and wound repair, the mechanical property of tissue engineered constructions has to been carefully designed for each specific application.

4.5 References

1. Palecek, S. P., J. C. Loftus, M. H. Ginsberg, D. A. Lauffenburger, and A. F. Horwitz. 1997. Integrin-ligand binding properties govern cell migration speed through cell-substratum adhesiveness. Nature 385:537-540.
2. Lo, C. M., H. B. Wang, M. Dembo, and Y. L. Wang. 2000. Cell movement is guided by the rigidity of the substrate. Biophys. J. 79:144-152.
3. Schmidt, C. E., A. F. Horwitz, D. A. Lauffenburger, and M. P. Sheetz. 1993. Integrin cytoskeletal interactions in migrating fibroblasts are dynamic, asymmetric, and regulated. J. Cell Biol. 123:977-991.
4. Lauffenburger, D. A., and A. F. Horwitz. 1996. Cell migration: A physically integrated molecular process. Cell 84:359-369.
5. Sheetz, M. P., D. P. Felsenfeld, and C. G. Galbraith. 1998. Cell migration: Regulation of force on extracellular-matrix-integrin complexes. Trends Cell Biol. 8:51-54.
6. Dembo, M., and Y. L. Wang. 1999. Stresses at the cell-to-substrate interface during locomotion of fibroblasts. Biophys. J. 76:2307.
7. Elson, E. L., S. F. Felder, P. Y. Jay, M. S. Kolodney, and C. Pasternak. 1999. Forces in cell locomotion. In Cell Behaviour: Control and Mechanism of Motility. Portland Press Ltd, London. 299-314.
8. Clark, R. A. F. The Molecular and Celluar Biology of Wound Repair. Plenum Press, New York and London.

9. Wang, N., J. P. Butler, and D. E. Ingber. 1993. Mechanotransduction across the Cell-Surface and through the Cytoskeleton. Science 260:1124-1127.

10. Galbraith, C. G., and M. P. Sheetz. 1998. Forces on adhesive contacts affect cell function. Curr. Opin. Cell Biol. 10:566-571.

11. Balaban, N. Q., U. S. Schwarz, D. Riveline, P. Goichberg, G. Tzur, I. Sabanay, D. Mahalu, S. Safran, A. Bershadsky, L. Addadi, and B. Geiger. 2001. Force and focal adhesion assembly: a close relationship studied using elastic micropatterned substrates. Nat. Cell Biol. 3:466-472.

12. Ghosh, K., X. D. Ren, X. Z. Shu, G. D. Prestwich, and R. A. F. Clark. 2006. Fibronectin functional domains coupled to hyaluronan stimulate adult human dermal fibroblast responses critical for wound healing. Tissue Eng. 12:601-613.

13. Ghosh, K., X. Z. Shu, R. Mou, J. Lombardi, G. D. Prestwich, M. H. Rafailovich, and R. A. F. Clark. 2005. Rheological characterization of in situ cross-linkable hyaluronan hydrogels. Biomacromolecules 6:2857-2865.

14. Guan, E., S. Smilow, M. Rafailovich, and J. Sokolov. 2004. Determining the mechanical properties of rat skin with digital image speckle correlation. Dermatology 208:112-119.

15. Derycke, L. D. M., and M. E. Bracke. 2004. N-cadherin in the spotlight of cell-cell adhesion, differentiation, embryogenesis, invasion and signalling. Int. J. Dev. Biol. 48:463-476.

16. Ko, K. S., P. D. Arora, V. Bhide, A. Chen, and C. A. G. McCulloch. 2001.

Cell-cell adhesion in human fibroblasts requires calcium signaling. J. Cell Sci. 114:1155-1167.

17. Mary, S., S. Charrasse, M. Meriane, F. Comunale, P. Travo, A. Blangy, and C. Gauthier-Rouviere. 2002. Biogenesis of N-cadherin-dependent cell-cell contacts in living fibroblasts is a microtubule-dependent kinesin-driven mechanism. Mol. Biol. Cell 13:285-301.

18. Ganz, A., M. Lambert, A. Saez, P. Silberzan, A. Buguin, R. M. Mege, and B. Ladoux. 2006. Traction forces exerted through N-cadherin contacts. Biol. Cell 98:721-730.

19. MonierGavelle, F., and J. L. Duband. 1997. Cross talk between adhesion molecules: Control of N-cadherin activity by intracellular signals elicited by beta 1 and beta 3 integrins in migrating neural crest cells. J. Cell Biol. 137:1663-1681.

20. Goffin, J. M., P. Pittet, G. Csucs, J. W. Lussi, J. J. Meister, and B. Hinz. 2006. Focal adhesion size controls tension-dependent recruitment of alpha-smooth muscle actin to stress fibers. J. Cell Biol. 172:259-268.

4.6 Figure Captions

Figure 4. 1 *En masse* versus single cell migration as function of crosslinking ratio of the substrate (substrate stiffness).

Figure 4. 2 *En masse* versus single cell migration as function of bulk density of C domain in the substrate (substrate adhesiveness).

Figure 4. 3 Time-lapse measurement of *en masse* versus single cell migration as function of incubation time (cell density). (A) Phase contrast images of *en masse* cell migration from the same agarose droplet after different incubation time, 6/15/24 hours, respectively, which resulted in different cell densities on the edge. (B) Time-lapse measured *en masse* versus single cell migration speed after different incubation time.

Figure 4. 4 The distance from cells on the edge to the agarose droplet and distance between cells as function of incubation time (cell density) (A) A schematic of cells migrating outward from the agarose droplet with r_x, r_y and s shown the distance from the nucleus of the cell on the edge to the nuclei of neighboring cells and the distance to the droplet. (B) Average distance of the cells on the edge to the droplet after different incubation time. (C) Average distance from the nucleus of the cell on the edge to the nuclei of neighboring cells as function of cell migration speed after different incubation time.

Figure 4. 5 Fluorescence imaging of vinculin-containing focal adhesions distribution (green) and actin cytoskeleton organization (red) as function of incubation time (cell

density).

Figure 4. 6 Quantification of the distribution of focal adhesions as function of incubation time (cell density). The total number (A), the front to rear ratio (B) and the average size (C) of focal adhesions after different incubation time.

Figure 4. 7 Local displacements generated by *en masse* cells migrating outward from the agarose droplet as function of incubation time. The phase contrast images (left column) recorded the location of cells, and related displacement maps (right column) were obtained using DISC technique with color bar unit: μm.

Figure 4. 8 Local displacements generated by *en masse* cells migrating outward from the agarose droplet as function of substrate stiffness. The phase contrast images (left column) recorded the location of cells, and related displacement maps (right column) were obtained using DISC technique with color bar unit: μm.

4.7 Figures

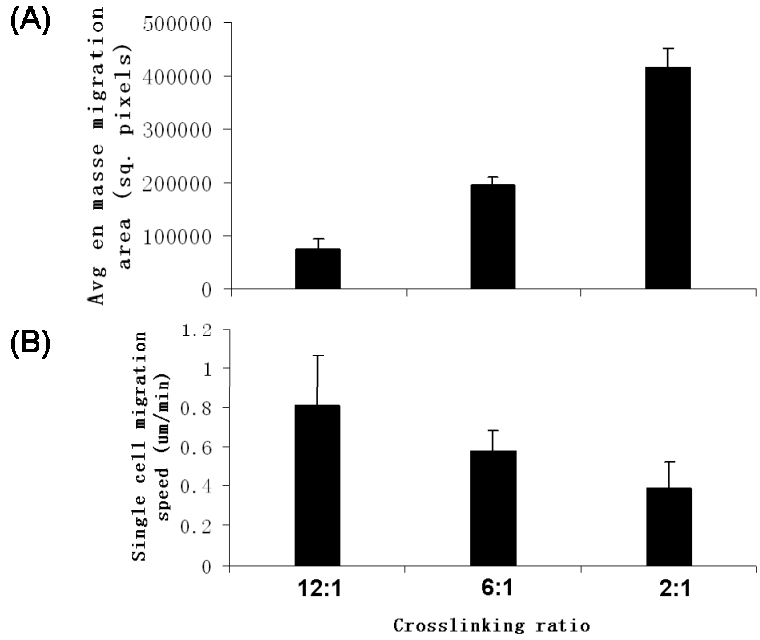

Figure 4.1

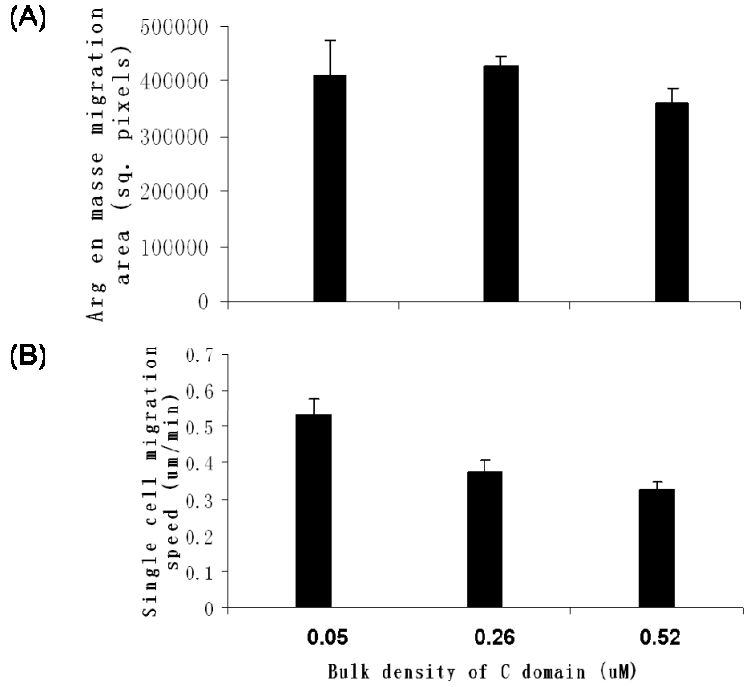
(A)
Arg en masse migration area (sq. pixels)
500000
400000
300000
200000
100000
0
(B)
Single cell migration speed (um/min)
0.7
0.6
0.5
0.4
0.3
0.2
0.1
0
0.05
0.26
0.52
Bulk density of C domain (uM)

Figure 4.2

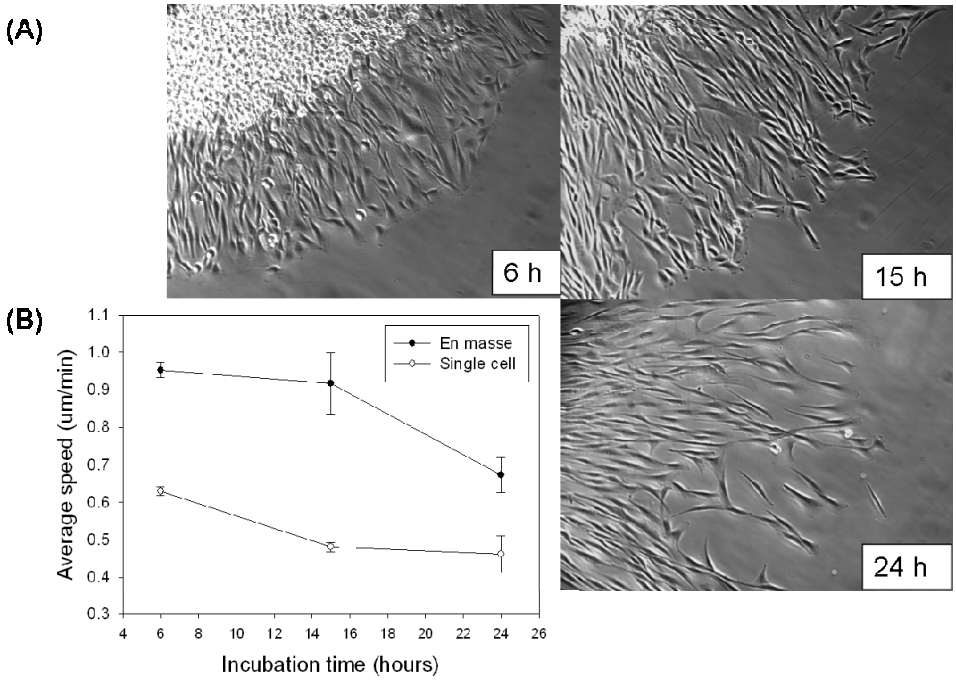
(A)
6 h
15 h
24 h
(B)
Average speed (um/min)
Incubation time (hours)
En masse
Single cell
1.1
1.0
0.9
0.8
0.7
0.6
0.5
0.4
0.3
4
6
8
10
12
14
16
18
20
22
24
26

Figure 4.3

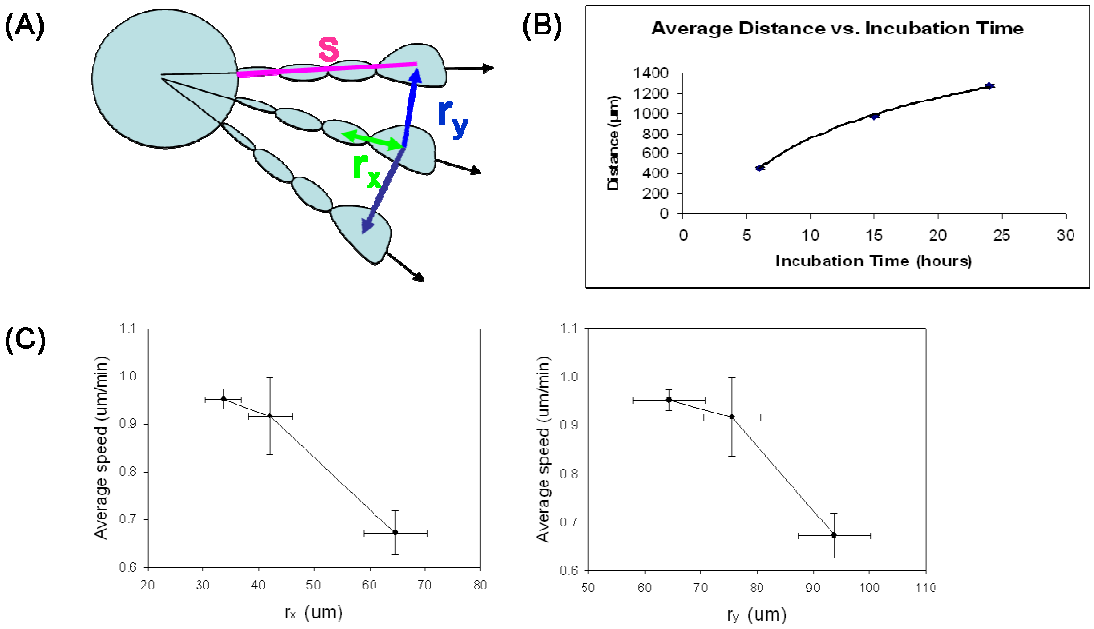
(A)
S
r_y
r_x
(B)
Average Distance vs. Incubation Time
Distance (µm)
1400
1200
1000
800
600
400
200
0
0
5
10
15
20
25
30
Incubation Time (hours)
(C)
Average speed (um/min)
1.1
1.0
0.9
0.8
0.7
0.6
20
30
40
50
60
70
80
r_x (um)
Average speed (um/min)
1.1
1.0
0.9
0.8
0.7
0.6
50
60
70
80
90
100
110
r_y (um)

Figure 4.4

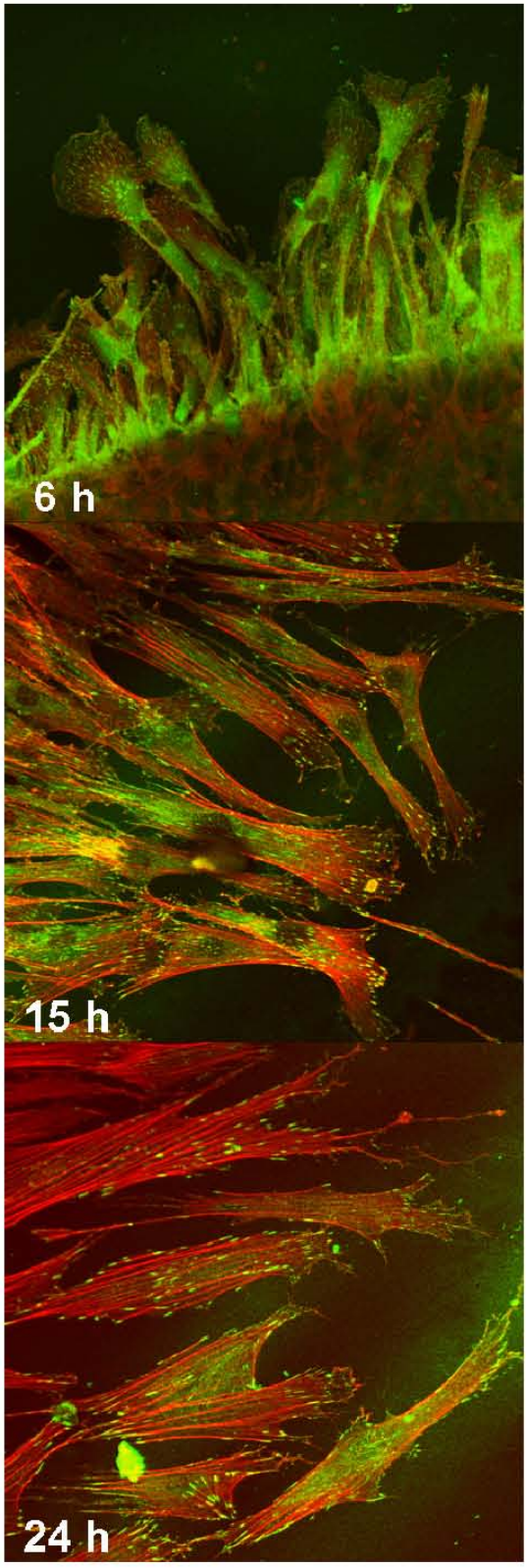

Figure 4.5

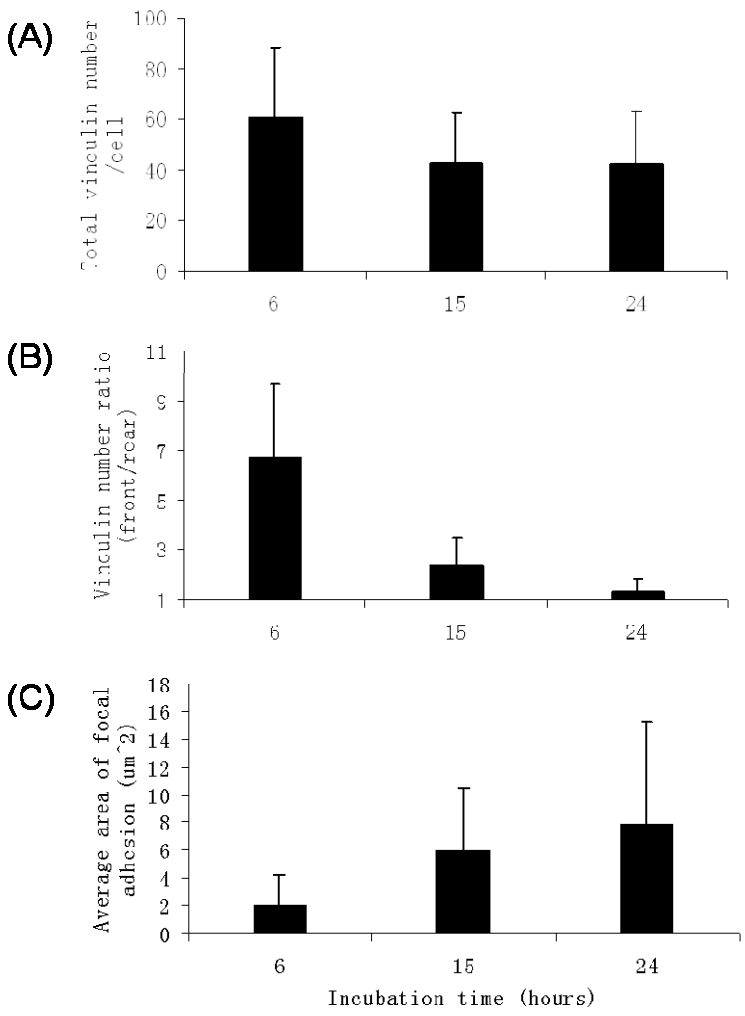
(A)
Total vinculin number /cell
100
80
60
40
20
0
6
15
24
(B)
Vinculin number ratio (front/rear)
11
9
7
5
3
1
6
15
24
(C)
Average area of focal adhesion (um^2)
18
16
14
12
10
8
6
4
2
0
6
15
24
Incubation time (hours)

Figure 4.6

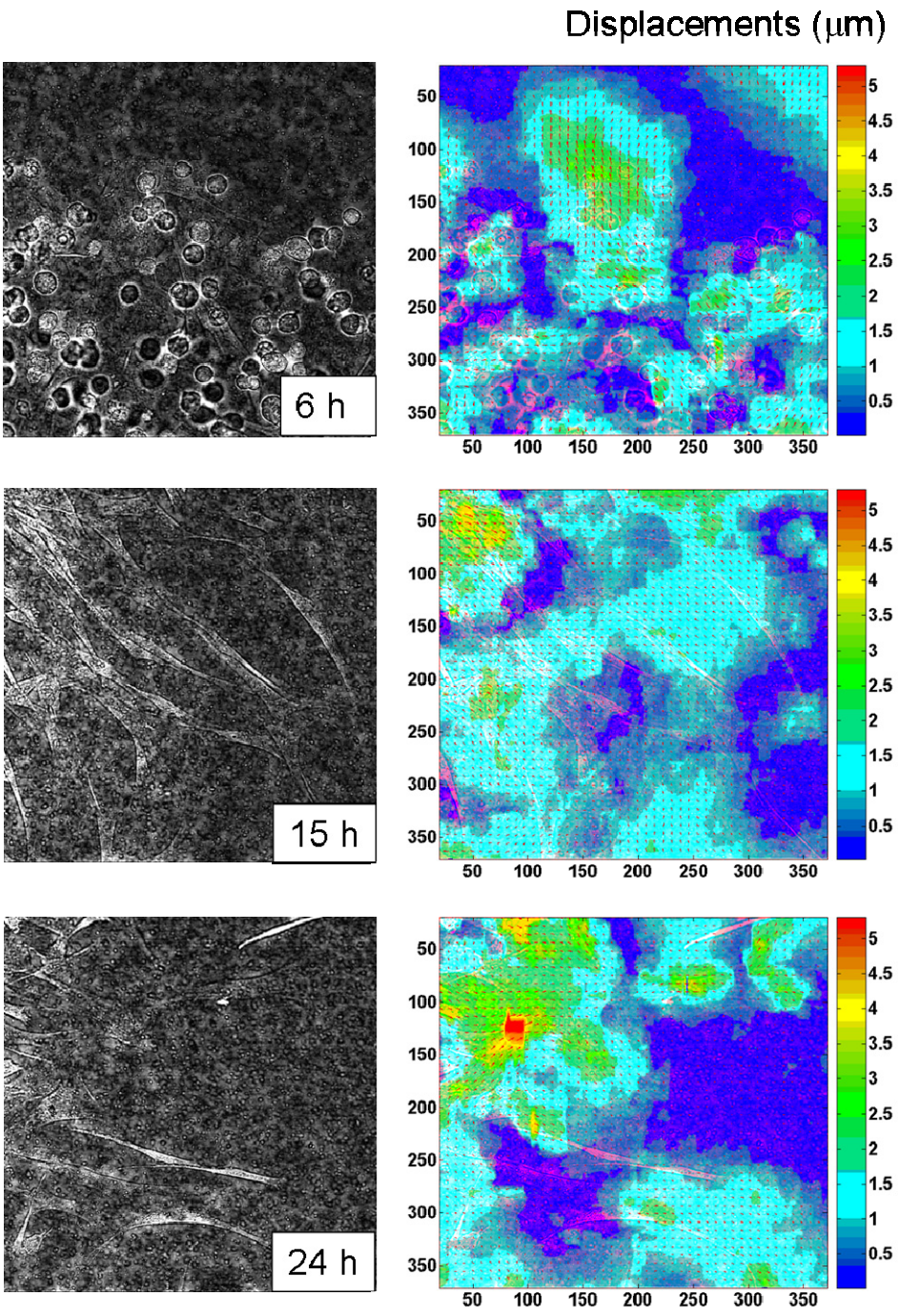
Displacements (μm)
6 h
15 h
24 h
50
100
150
200
250
300
350
5
4.5
4
3.5
3
2.5
2
1.5
1
0.5

Figure 4.7

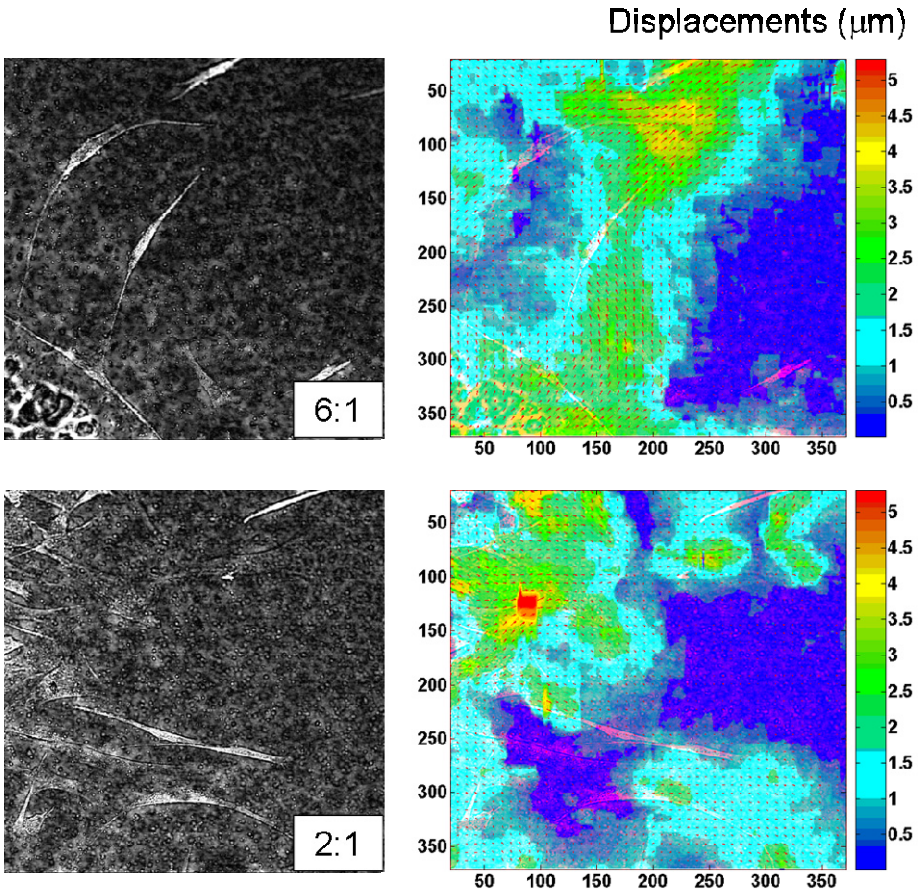
Displacements (μm)
6:1
2:1
50
100
150
200
250
300
350
5
4.5
4
3.5
3
2.5
2
1.5
1
0.5

Figure 4.8

Chapter 5

Adverse effects of titanium dioxide nanoparticles on human dermal fibroblasts and how to protect cells

Preface

This chapter has been reproduced from:

Pan, Z., W. Lee, L. Slutsky, R.A.F. Clark, N. Pernodet, and M.H. Rafailovich. 2009. Adverse effects of titanium dioxide nanoparticles on human dermal fibroblasts and how to protect cells. Small. 5: 511-520,

with permission from Wiley-VCH.

Original contribution: Data for Figure 5.1, 5.3 – 5.8, 5.11, 5.12

In collaboration: Data for Figure 5.2, 5.9, 5.10

5.1 Introduction

Nanotechnology has been dramatically advanced in recent years. Due to their unique size-related properties such as high quantum yield and large surface area to volume ratio, nanomaterials have shown emerging applications in electronics, biology, and medicine (1). As a result, the biomedical use of nanomaterials is being explored in broad areas such as nano-imaging, drug delivery, biosensors and cancer phototherapy

(2-8). However, size effects of nanomaterials may also cause higher toxicity because of their larger surface area, enhanced chemical reactivity and easier cell penetration (9-11). Recently, it has been shown that scale alone could have adverse effects on cell function (12, 13). Pernodet et al. (12) have shown that the presence of Au particles, which is considered as an inert material for living cells, was sufficient to induce aberrant actin formation and interfere with cell migration. Hence it is to be expected when the particles are chemically active, that size effects can also exacerbate the adverse effects. Actually, for those materials possessing nanostructure-dependent properties, such as chemical, mechanical, electrical, optical, magnetic, biological properties, which make them more important for commercial use, the same properties may potentially lead to adverse effects that differ from the bulk properties of these materials. Therefore, the safety issue of nanomaterials, especially those used for consumer applications, has attracted increasing attention (9).

Here, we focused on TiO_2, which is a naturally occurring mineral and known to be biologically inert and non-toxic at the micro-scale in both human and animals (14-16). TiO_2 has been widely used in industry as an additive ranging from paint, food colorant to cosmetics and drugs. The most common use of TiO_2 is as an additive in cosmetics where its high absorbance for UV radiation is used to increase the SPF factors of sunscreens. The same property also makes TiO_2 an important component of food packaging where it is added to prevent damage from UV and increase shelf life. However, once it absorbs UV light, TiO_2, as a well-known photocatalyst, also catalyzes the generation of reactive oxygen species (ROS). This property makes TiO_2

a favorite component for antibacterial applications (17), as well a major component in solar power cells, where sunlight is converted to electricity (18). As is pointed out by Dunford et al. (19), the same property can also make TiO_2 a potentially hazardous material since ROS products in turn are known to cause genetic damage and other adverse effects in living tissue (20). The ability of TiO_2 to photocatalyze the production of ROS products is further enhanced when the particles are ground to nanometer dimensions, thereby increasing the surface area and the electron flux. For example, it was shown that they can cause inflammatory reactions in both animals and humans when ground into particles smaller than 20 nm (21-23).

Many studies reported that cells cultured in the presence of TiO_2 nanoparticles showed a dramatic decrease in growth rate with exposure to concentrations larger than 0.1 mg/ml (24). Most of these reports directly correlated the cytotoxicity of TiO_2 nanoparticles to induced oxidative damage (25). But, since most of the experiments were conducted in the dark, the source of the oxidative process was not immediately apparent. In order to understand the mechanism in more details, and especially to determine if something could be done to prevent the damage, in vitro experiments were performed with different types of TiO_2 nanoparticles here. And since most of the previous experiments were performed with transformed cell lines which have been shown to be more sensitive to nanoparticle damage than normal primary cells, we chose to use human dermal fibroblasts from primary culture. The skin is the primary barrier against contact penetration in cosmetic products, hence it was important to understand the effects which are specific to these cells with different particles which

are commonly encountered in cosmetic formulations. In particular, Lee et al. (26) recently showed that it was possible to graft a dense polymer coating onto the TiO_2 particles which can trap the photoelectron and suppress ROS production. We therefore performed a detailed study in order to determine how these particles also behaved in vitro when they came in contact with live cell cultures.

5.2 Materials and Methods

5.2.1 TiO_2 particle characterization

Dry TiO_2 powder was used as SEM sample to evaluate the particle size, shape and suspended status. In order to image individual particles clearly, the powder was dispersed in ethanol and spread on a carbon coated TEM grid. The crystallographic structures of these two different types of TiO_2 particles, rutile and anatase, were confirmed with X-ray diffraction. Additionally, different types of TiO_2 particles were suspended in PBS and loaded in 96-well dish prior to the fluorescence measurement, which was performed with a FLEXstation^{TM} benchtop scanning fluorometer (Molecular Devices).

5.2.2 Cell culture and function studies

Primary dermal fibroblasts obtained from a 31 years old Caucasian female (Clonetics) were used between passages 5 and 13. The cells were routinely cultured in full-DMEM which is supplemented with 10% fetal bovine serum and 1% Penicillin, Streptomycin and L-glutamine (P/S/G), in a 37°C, 5% CO_2, 95% humidity incubator

(Napco Scientific). TiO_2 media was prepared by dispersing the nanoparticles in the same full-DMEM at different concentrations. Before using, the TiO2 media was sonicated for ~30 minutes and stirred for at least 5 minutes to achieve homogeneous distribution. The experimental samples were prepared by culturing cells in these TiO_2 media at different concentrations for certain incubation time, with the media changed every 2-3 days.

Immunofluorescence images of cells were taken with a 40× oil lens on a Leica TCS SP2 laser scanning confocal microscope (Leica Microsystems) after the cells were stained by Alexa Fluor 488 phalloidin and propidium iodide for actin and nuclei, respectively. With MetaMorph software (Universal Imaging), the area of cells on these confocal images can be readily measured.

For cell counting, cells were seeded in 24-well dishes with an initial density of 2500 cells/well. After being cultured with full-DMEM or TiO_2 media for certain incubation time, cells were rinsed 3 times with PBS to remove any suspended particles and dead cells. Then the remaining adherent cells were detached with typsin and counted with a hemacytometer. Each experimental group contained at least 3 replicates to obtain the average cell number under each condition.

Quantification of cellular traction forces was achieved with digital image speckle correlation (DISC) technique combined with finite element method (FEM) as previously reported (27). After two days' exposure to the media without/with TiO_2 nanoparticles, the control and the experimental cells were reseeded onto HA/FNfd hydrogels with fluorescent beads in DMEM and kept in 37 ^{o}C incubator for 6 hours.

The images before and after cell detachment were recorded with a 63×, NA 0.9 water objective on a Leica TCS SP2 laser scanning confocal microscope (Leica Microsystems). Then the deformations generated by cell attachment on the hydrogel surface were quantified with DISC technique and the cellular traction stresses were calculated with FEM.

Cell migration was evaluated with agarose droplet assay. The agarose gel was prepared by diluting 2% (w/v) agarose stock solution with DMEM to the final concentration of 0.2 % (w/v). Then the 0.2 % (w/v) agarose was added to the cell pellets and the cell were re-suspended to 1.5×10^7 cells/ml. 1.25 µl droplets of such cell suspension were carefully loaded on the prepared HA/FNfd hydrogel surfaces in a 24-well dish. After that, the whole dish was placed at 4 ^{o}C for 20 minutes to allow the agarose droplet to gel before 400 µl of DMEM with 30 ng/ml PDGF being added into each well. After 18 hours incubation at 37 ^{o}C, the cells were fixed with 3.7% formaldehyde, stained with 0.1% crystal violet and rinsed 3 times with PBS for easy visualization under a stereomicroscope. To quantify cell migration, the area of agarose droplets and the area covered by the leading edges of the out-migrating cells were measured with SPOTCam software. The cell migration area was defined as the area of the outward cell migration minus the area of agarose droplets.

Collagen gel contraction is typically used to mimic the process of wound healing. Here, we measured the extent of gel contraction to evaluate the ability of cells to contract collagen matrix. Cells were suspended in prepared collagen solution (1.8 mg/ml purified collagen, 2% BSA, 30 µg/ml hFibronectin, 100 ng/ml PDGF in

DMEM with P/S/G) at 3×10^5 cells/ml. And the cell/collagen gels were loaded into a BSA coated 24-well dish with 0.6 ml/well. After pre-incubation for 2 hours to gel the mixture, collagen gels were gently detached by slight tapping on the wells and 500 μl DMEM with 2% BSA and 100ng/ml PDGF were added. Then after another 2 hours' incubation, the phase images of gels were taken and analyzed by measuring the gel size. The contracted ratio was defined as the ratio of the contracted area (which is the original gel size minus the final gel size) to the original gel size.

For Western blotting, whole cell lysate was prepared by scraping cells in lysis buffer with protease inhibitors and PMSF, and then mixed with 4×SDS-PAGE buffer (0.25 M Tris, pH 6.8, 8% SDS, 40% glycerol, 0.02% Bromophenol Blue with 80 mM DTT) at a volume ratio of 3:1. After the mixture was boiled at 100 ^{o}C for 3 minutes, the protein from the same number of cells, both the control and the experimental ones, was separated by SDS-PAGE and electrophoretically transferred to nitrocellulose membrane. Blots were probed with the anti-actin antibody, Act(C-11), goat polyconal IgG (Santa Cruz Biotechnology). The primary antibodies were then detected with the secondary antibodies, rabbit anti goat IgG(H+L) (ImmunoPure Antibody, Pierce Biotechnology), followed by enhanced chemiluminesence (SuperSignal West Dura Extended Duration Substrate, Pierce Biotechnology). The picture of the bands was taken with a ChemiImager^{TM} Ready camera (Alpha Innetech Corporation) and their densities were quantified with ChemiImager v5.5 (Alpha Innetech Corporation).

5.2.3 TEM

In order to monitor how TiO_2 nanoparticles penetrate cells and where they stay in cells, cells exposed to nanoparticles with different incubation time were fixed as following and imaged with TEM. The fresh samples were rinsed 3 times with PBS and fixed for 30 minutes in modified Karnovsky fixative, using 2.5 % (v/v) glutaraldehyde and 2 % (w/v) paraformaldehyde in 0.1 M cacodylate buffer PH 7.2-7.4 with 2.5 mM calcium chloride. The samples were then rinsed 3 times with cacodylate wash buffer for ~5 minutes. After that, the samples were post-fixed in 2 % Osmic acid for 15 minutes and stained in saturated aqueous solution of Uranyl acetate for 15 minutes. The dehydration process was performed in a graded series of 30%, 50%, 70%, 95% ethanol and 2 times in 100% ethanol, for 15 minutes each. Then the samples were infiltrated with a 50/50 mixture of 100% ethanol and Spurr's plastic. After discarding the mixture 1 hour later, 100% Spurr's was added to infiltrate the cells for another 1 hour. The samples were kept in vacuum oven at 60 ^{o}C overnight after changing the Suprr's. Finally, the samples were cut into light gold colored ultra-thin sections with a microtome and stained on the grid with uranyl acetate and lead oxid, each for 5 minutes. After being washed thoroughly with distilled water, TEM samples of cells were dried and then imaged under JEOL (model 1200EX) transmission electron microscopy. We analyzed the images by characterizing the penetration, the distribution, the specific location of nanoparticles and quantifying the size of vesicles and particle cluster at different time point for different types of the nanoparticles.

5.2.4 Particle coating

Rutile TiO_2 nanoparticles were coated by chemically grafting a dense antioxidant/anionic and hydrophobic polymer molecules directly onto the surface. This technique has been recently reported (26). Briefly, antioxidant formed from grape seed extracts (Oligomeric Proanthocyanidins) and anionic polymer- Poly [Methyl Vinyl Ether/maleic Acid] were mixed at a 1:1 ratio and dissolved in a 22:1 water /denatured ethanol solution using a lightening mixer at 25°C. After the solution became homogeneous, a new mixture was prepared that composed of 30% (w/w) of the antioxidant/anionic polymer solution, 22% (w/w) DI water, 43% (w/w) titanium dioxide and 5% (w/w) hydrophobic polymer (Triethoxysilylethyl Polydimethylsiloxyethayl Dimethicone, Shin-Etu Chemical Co., Ltd). The entire slurry was then sonicated for 30 minutes with medium intensity at 25°C with an Ultrasonic probe (Sonicor Instrument Co.) at 20 KHz. In order to precipitate the particles and remove the excess polymers, the resultant mixture, which was a thick colloidal suspension, was then centrifuged for 15 minutes at 9000 rpm and washed with DI water. The washing procedure was repeated three times in order to ensure that all unattached materials were removed. The product was then dried at 110 °C under vacuum for 16-20 hours.

5.2.5 Flow cytometry

Both the control and the experimental cells were carefully rinsed more than 3 times to remove all the floating particles in the experimental media and detached with

typsin-EDTA. After stopping trypsin with full-DMEM, the cells were rinsed twice using DMEM with 0.2% BSA to be separated well. Then the cells were suspended and fixed in 1% paraformaldehyde in PBS for 20 minutes. After being rinsed twice using PBS and resuspended in PBS at the concentration of 1×10^6 cells/ml, the sample solutions were ready for flow cytometry which performed with a BD FACSCalibur™ benchtop flow cytometer.

5.2.6 Measurement of hydrogen peroxide

The cellular level of hydrogen peroxide was measured with the aid of the fluorogenic probe, Amplex red, as described by Eu et al.(28) with certain modifications. Briefly, both the control and experimental cells exposed to different type TiO_2 nanoparticles were washed, suspended in 200 µl of ice-cold distilled water, and sonicated for 3 minutes with a 9 second pulse with 1 second off. Then, in order to avoid the influence of fluorescence from TiO_2 nanoparticles, all the samples were spinned and only 100 µl of clear supernatant was added to 1 ml of the reaction buffer (10 µM Amplex red,10mM Tris–HCl (pH 7.4), and 1 U/ml horseradish peroxidase) and mixed carefully. The mixture was transferred into 96-well dish and incubated at 37 °C for 5 minutes before the fluorescence measurement. Fluorescence of the reaction buffer and the sample solution was measured with a FLEXstation™ benchtop scanning fluorometer (Molecular Devices) with excitation and emission at 560 and 590 nm, respectively.

5.3 Results and Discussion

5.3.1 TiO_2 nanoparticle characterization

In Fig. 5.1 we show SEM and TEM micrographs of the TiO_2 particles that we used. The uncoated rutile particles tend to agglomerate into large spheres several microns in diameter. From Fig. 5.1(A) it is clear that the spheres are composed of smaller particles. In order to image them directly, we dispersed the spheres in ethanol and then spread a droplet of the solution on a carbon coated TEM grid. The TEM image is shown in Fig. 5.1(B) where we see that the particles are oblate, but of uniform size and shape. The average width of the particles is 15.0 ± 3.5 nm, and they are elongated with an aspect ratio of ~ 3.92. In commercial products, the aggregates are difficult to compound in formulations, and hence micro-sized talc is frequently added acts as a dispersant. The talc particles are hard and angular, which allows them to break the aggregates and disperse the particles more uniformly. This can be seen in the SEM image of anatase TiO_2 particles as shown in Fig. 5.1(C). And Fig. 5.1(D) is the TEM image of these anatase TiO_2 particles with talc, where it is clearer that they have different shapes from rutile particles and much larger sizes, 200 ± 13 nm. The crystallographic structures of these two different types of TiO_2 particles were confirmed by X-ray diffraction (Fig. 5.1 (E)).

These particles in either rutile or anatase phase, are commonly used in consumer products. Hence in this paper, we compared both ultra fine rutile TiO_2 (US Cosmetics) nanoparticles and dispersed anatase TiO_2 (US Cosmetics) nanoparticles, both of

which are regarded as a biocompatible material in the absence of photoactivation. Although people usually think smaller nanoparticles are easier to penetrate cells and induce higher damages, we found that the phase is a more crucial factors rather then the size or shape, which is consistent with previous reports (24).

In this study, we also noticed that the TiO2 particles are naturally fluorescent with a broad band excitation in the range from UV to optical. The fluorescence spectrum is also very broad with no apparent peak in intensity in the observed region. On one hand, the effect can perturb studies where one is counting specific florescence from a particular stain, such as measurements detecting apoptosis, metabolism, and ROS. On the other hand, if we do not use staining, this can be a useful tool for detecting nanoparticles associated with cells.

5.3.2 Rutile TiO_2 nanoparticles

In order to determine the effects of nanoparticle exposure on cell conformation we incubated human dermal fibroblasts with the rutile particles shown in Fig. 5.1(A) and (B). The confocal images of cells with stained actin (green) and nuclei (red) are shown in Fig. 5.2(A). From the figure we can see that after 6 days' incubation, the introduction of rutile TiO_2 particles caused a large decrease in the cell area, as compared to the control sample. Closer examination of the image also indicates that the morphology of the cells is affected. The control cells are triangulated and well spread on the surface, while the cells exposed to TiO_2 have become elongated and appear to detach from the surface. This is also shown graphically in Fig. 5.2(B) where

we plot the cell area averaged over several hundred cells which were incubated with 0.4 mg/ml and 0.8 mg/ml of particles for 6 days. From the figure we can see that the cell area of the experimental samples is on average 1/4 and 1/5, respectively, that of the control sample incubated at the same time without particles. In Fig. 5.2(A), we can also see that in analogy with the findings of Pernodet et al.(12) on the same cell model, the decrease in area is also associated with a change in the actin fibers, where they become thinner and less extended.

Since actin is implicated in many cell functions and behaviors, such as cell division, we also measured the proliferation at these particle concentrations. The cell numbers after 6 days of incubation are plotted in Fig. 5.2(B). From the figure we can see that the cell counts are drastically reduced, and the cells, though still alive, have nearly stopped dividing. Most previous toxicity studies (13) have focused on cell death, but here we show that for low concentration the cells can survive, but the question arises, as to their ability to perform essential functions.

As we know, dermal fibroblasts play a central role in the wound healing process. In the initial process, they migrate into the wound site and the tissue repair begins when they contract the collagen fibers so that the keratinocytes can differentiate and form the subsequent layers of the skin tissue. These functions are comprised of two separate processes, cell migration and collagen contraction, both depending on the ability of the cells to exert traction forces on the substrate. In order to study whether nanoparticles influence cell functions, we first exposed cells to 0.4 mg/ml TiO_2 nanoparticles for two days and then compared their functions with normal control

cells.

We first measured the effect on traction forces exerted by the cells using the techniques described previously (27). We used a synthetic hydrogel compose of crosslinked functionalized hyaluronic acid (HA) and fibronectin functional domains (FNfds) as the flexible substrate which was impregnated with fluorescent beads. Digital image speckle correlation (DISC) technique combined with finite element method (FEM) was then used to measure the traction stress intensity and distribution on the surfaces. The results are shown in Fig. 5.3(A), for a representative cell. We can see that in the absence of nanoparticles, the cells are well spread on the hydrogel, and robust traction forces are exerted along the periphery. The hydrogel used here was relatively stiff and good cell adhesion and triangulation was previously reported (29). When the nanoparticles are added, even though the cells prefer these surfaces, the cell area is reduced and the cells become elongated. Elongation can also be associated with cell migration. This was previously described by Ghosh et al. (27) when cells were plated on softer surfaces where large traction forces only appeared behind the leading edge and cells migrate faster. Here we see that despite the elongated appearance, only weak traction forces are exerted.

The cell migration was then measured in a separate set of experiments where an agarose droplet cell migration assay was done. Here we defined the migration area as the difference between the total area that cells covered after 18 hours' migration and the area of agarose droplet. And the results are shown in Fig. 5.3(B). In the inset phase images, the black rings delineate the periphery of the migrating circles of cells and the

white rings show the area of agarose droplets, where we can clearly see that the migration is far smaller for cells exposed to 0.4mg/ml TiO_2 than for the unexposed cells. Using the migration area to evaluate the cell mobilities, we can see that the TiO_2 exposure reduced migration by ~ 59 %.

The ability of cells to contract collagen matrix was also studied. The same number of normal cells and cells incubated with 0.4mg/ml of TiO_2 particles were cultured in collagen gels for 4 hours. The optical images of the gels are shown as the inset of Fig. 5.3(C), where we can clearly see that the collagen gels contacted by the normal cells are significantly smaller than those contracted by cells exposed to TiO_2. The collagen contraction ratios averaged over 3 samples are plotted in Figure 5.3(C). The contraction of cells exposed to TiO_2 was less than 80% of the control sample.

Since the TiO_2 particles can be excited with 488 nm radiation and their emission spectrum is wide, the particles are also apparent in the confocal microscope images, especially those obtained using Hg lamp florescence. Due to the resolution of microscopy, the fluorescence observed is from large particle clusters. In order to visualize how the particles entered the cell and where they are sequestered, we performed transmission electron microscopy on cells incubated with 0.4 mg/ml rutile TiO_2 nanoparticles. We first imaged cells incubated with the TiO_2 nanoparticles for two days, the same time scale used for migration and contraction studies. A typical image is shown in Fig. 5.4(A). In these images, we can clearly see the TiO_2 particles, which are more electron dense than the surrounding cell environment. After two days, even though the cells seem to have ingested a relatively large amount of particles, we

know from the previous experiments, that they have still retained the ability to perform most functions. Most of the particles seem to be confined inside vesicles, distributed across the cytoplasm, but which do not cross into the nucleus. A higher magnification image of the vesicles was also obtained and shown in Fig. 5.4(B). Here we see that the particles that comprise the clusters surrounded by the vesicle membrane. In previous study, Pernodet et al.(12) also showed Au nanoparticles capsulated in single vesicles of dermal fibroblasts, In that case, the vesicles were only partially filled with particles and the membranes of the vesicles were intact. Here it appears that many more particles are stuffed in each vesicle, thereby possible leading to rupture. The boundary with the nuclear membrane is also visible in Fig. 5.4(B). Here we see that one of vesicles that is close to the nucleus does not have an intact enclosure, and the particles have begun to leak out. Several individual particles shown in the circle might be able to cross the nuclear membrane.

Another instance is shown in Fig. 5.4(C) where we can see a vesicle containing a very large cluster of particles, impinging upon the nucleus. The vesicle membrane surrounding the cluster appears ruptured, in the upper corner a segment of particles has pierced through the membrane, and in the back portion facing away from the nucleus the membrane is completely frayed. The nuclear membrane is distorted, but remains distinct from the vesicle membrane and is intact (see the dashed line). A small particle cluster though is seen to have become lodged inside the membrane (see the arrow), but has not penetrated into the nucleus.

In order to determine how the particles entered the cell, we also performed a series

of TEM cross sections corresponding to a time sequence incubation as shown in Fig. 5.5(A). We can see that after 30 minutes, some particles are attached to the cell membrane, but very few have penetrated inside the cells. Closer examination of the particles on the membrane indicates that some are lodged on the membrane, but no evidence of endocytosis is observed for the isolated particles. Larger clusters can also be seen on the membrane, but no evidence of penetration as clusters is observed. Closer examination of the images shows individual particles are already lodged inside large otherwise empty vesicles. In Fig. 5.5(B) we plot the mean size of both vesicles and clusters as a function of incubation time. We find that at the time point of 30 minutes, the size of vesicles is fairly uniform with a mean diameter of ~ 286 nm which is much larger than the individual particle size. After 1 hour, larger clusters are seen to form inside the vesicles, and individual particles are observed at the membrane. With time up to 5 hours, the amount of individual particles at the membrane increases, and clusters are also observed with indented cell membrane which is in process of endocytosis. At the same time, the size of the clusters in the vesicle increases dramatically. From Fig. 5.5(B) we can see that the cluster size approaches ~ 77 % that of the mean vesicle size after 5 hours, and both the vesicle size and the cluster size do not increase significantly after that time. We can therefore define an occupancy factor as the ratio of cluster to vesicle size. We then plot occupancy factor versus incubation time in Fig. 5.5(C) where we see that it increases rapidly in the first 5 hours and then levels off in the next 43 hours. In this case, as more particles enter the cells, more vesicles are created and then filled. The cluster

size is limited by the vesicle size. Any further increase in cluster size, probably leads to the rupture of the vesicle. This can be seen in the TEM images of the particle clusters shown in Fig. 5.4(C), where the size of the vesicle filled with clusters is almost ten times of the average size.

5.3.3 Anatase TiO_2 nanoparticles

Anatase TiO_2 is known to be even more photoactive than rutile. In Fig. 5.6(A) we show confocal images of cells incubated with anatase TiO_2 particles at different concentrations for 3 days. Comparison with Fig. 5.2 we can see that anatase particles with even lower concentration and shorter incubation time can produce far more damage to the cells than rutile particles. Closer examination indicated that even the cells incubated with 0.1mg/ml of anatase particles had broken actin and nanoparticles surrounding the nuclear membrane. Cells incubated at the higher concentrations had nearly no visible actin fibers, and the membranes appear to have ruptured. To further confirm that the damage to actin cytoskeleton was caused by anatase TiO_2 nanoparticles rather than micro-sized talc particles, another control sample with equal amount talc was examined, where we can see that cells cultured in media with talc still grew well after 3 days and showed clear and strong actin fibers. These results are consistent with survival cell number after being cultured for 7 days in the presence of anatase TiO_2 nanoparticles at different concentration. As shown in the bar graph of Fig. 5.6(B), only cells incubated with 0.1 mg /ml or less survived and were able to proliferate. Cells cultured with a concentration of 0.3 mg/ml or higher failed to grow.

Cell numbers were significantly decreased after exposure to high concentration of anatase TiO_2 nanoparticles.

The dramatic damage induced by anatase TiO_2 nanoparticles to actin was confirmed by Western blot. Compared to the adverse influence of rutile particles, anatase particles show dramatic effect on the actin of cells after two days' incubation as shown in Fig. 5.7, which would severely impair cell functions.

Fig. 5.8 shows TEM images of microtomed sections from cells exposed to 0.4 mg/ml anatase TiO_2 nanoparticles. From Fig. 5.8(A) we can see that the anatase particles caused huge holes to form in the cell cytoplasm, which may be the remnants of vesicles that were filled with particles. Although more damages were found outside of the nuclei, we also noticed that some vesiculated nuclei (Fig. 5.8(B)). This would raise more issues, such as whether these nanoparticles could directly harm DNA molecules and induce further damage at gene level. Previous studies about the effects of TiO_2 nanoparticles on DNA have already shown that DNA would be partially decomposed when exposed to UV radiation (30). Here, the TEM images confirmed that this phenomenon is not neglectable, because it is possible for nanoparticles to get into the nuclei of nomal tissue cells under certain conditions.

5.3.4 Coated TiO_2 nanoparticles

The first step in the penetration process appears to be adhesion of the particles to the cell membrane. Hence we proposed that if the adhesion mechanism was somehow impeded, the penetration of the particles into the cells would be greatly reduced. Lee

et al.(26) have recently shown that it was possible to chemically graft a dense charged polymer layer onto the TiO_2 particles using sonochmeical methods. This layer was able to trap electrons emitted by the particles and form a dense polymer brush with an approximate grafting density of one chain per 0.6 nm. It is known that very stretched brushes do not adhere to surfaces, since entropic hindrance prevents further distortion of the brush, resulting in hard core repulsion. We therefore postulated that this effect may also prevent the coated particles from adhering to the cell surface membranes.

In order to probe this hypothesis, we first coated the rutile TiO_2 using Lee's technique (26). The SEM and TEM micrographs of coated rutile TiO_2 nanoparticles are shown in Fig 5.9. We then added the coated rutile TiO_2 nanoparticles to cell culture media with different concentration at the same concentrations as the non-coated rutile particles. From Fig. 5.2(B) we have shown that cells incubated with non-coated rutile TiO_2 particles have a much slower proliferation rate than the control sample. Cells incubated with coated particles are almost indistinguishable from the control samples for all times. In Fig. 5.10(A), cell counts after eleven days incubation are still comparable to the control. Corresponding Hg lamp fluorescent images of the cells demonstrate particles in the media, but they do not appear to be in or on the cells (Fig. 5.10(B)).

In order to further determine whether there are less coated particles either inside or on the cell, flow cytometry was performed on the cells exposed to different types of TiO_2 particles. Since TiO_2 particles have natural florescence, no additional staining was required. The results are shown in Fig. 5.11 for cells incubated with 0.4 mg/ml

rutile, anatase, and coated rutile particles for two days. Optical images of the cells prior to injection into the flow cytometer show that the particle uptake is significantly larger for cells incubated with anatase particles than with rutile ones, while nearly no uptake is observed for cells incubated with the coated rutile particles. Since the cells were washed many times, the emission could only come from particles attached to the cells. In flow cytometry studies, distinct peaks of high fluorescent intensity were observed with cells incubated with uncoated rutile or anatase particles, but not from cells incubated with coated TiO_2 (Fig. 5.11). These latter cells had an emission spectrum almost identical to cells not incubated with particles at all. Since the particle concentration in the cells is proportional to the intensity of the emission, we can estimate by the median value that the uptake of anatase particles is roughly three or nine times that of the uncoated and coated rutile particles for the same incubation time and concentration, which is consistent with the larger damage observed.

Since nanoparticles are also known to induce oxidative stress, we assayed the ROS production, hydrogen peroxide (H_2O_2), of cells incubated under the same conditions as those used in flow cytometry test. H_2O_2 produced by the cells incubated with coated rutile particles was comparable to the control sample as shown in Fig. 5.12. The H_2O_2 levels were significantly elevated by ~ 24 % and ~ 70 % for the cells incubated with rutile and anatase nanoparticles respectively, which are consistent with the particle uptake and the damages induced by these particles. Since all the studies here are performed without UV exposure, these results indicate that nanoparticle attachement and penetration may be the reason for cells to produce oxidative stress

and induce ROS production.

5.4 Conclusion

In this study, we showed that both rutile and anatase TiO_2 nanoparticles impair cell functions, with the latter being more potent at producing damage. Exposure to nanoparticles decreases cell area, proliferation, mobility, and ability to contract collagen. These TiO_2 nanoparticles particles can easily penetrate through cell membranes and are sequestered inside vesicles. In time vesicles fill up and eventually rupture. Particles that were coated with a polymer brush did not adhere to cell membranes and hence did not penetrate cells, which decreased ROS formation and thus allowed normal cell functions. Considering the broad applications of these nanoparticles in personal health care products, the functionalized polymer coating can potentially play an important role in protecting cells and tissue from damage.

5.5 References

1. Ball, P. 2001. Roll up for the revolution. Nature 414:142-144.
2. Muldoon, L. L., M. Sandor, K. E. Pinkston, and E. A. Neuwelt. 2005. Imaging, distribution, and toxicity of superparamagnetic iron oxide magnetic resonance nanoparticles in the rat brain and intracerebral tumor. Neurosurgery 57:785-796.
3. Neuberger, T., B. Schopf, H. Hofmann, M. Hofmann, and B. von Rechenberg. 2005. Superparamagnetic nanoparticles for biomedical applications: Possibilities and limitations of a new drug delivery system. J. Magn. Magn. Mater. 293:483-496.
4. Kreuter, J. 1991. Nanoparticle-Based Drug Delivery Systems. J. Control. Release 16:169-176.
5. Jin, S., and K. M. Ye. 2007. Nanoparticle-mediated drug delivery and gene therapy. Biotechnol. Prog. 23:32-41.
6. Bellocq, N. C., S. H. Pun, G. S. Jensen, and M. E. Davis. 2003. Transferrin-containing, cyclodextrin polymer-based particles for tumor-targeted gene delivery. Bioconjugate Chem. 14:1122-1132.
7. Riboh, J. C., A. J. Haes, A. D. McFarland, C. R. Yonzon, and R. P. Van Duyne. 2003. A nanoscale optical biosensor: Real-time immunoassay in physiological buffer enabled by improved nanoparticle adhesion. J. Phys. Chem. B 107:1772-1780.

8. Kukowska-Latallo, J. F., K. A. Candido, Z. Y. Cao, S. S. Nigavekar, I. J. Majoros, T. P. Thomas, L. P. Balogh, M. K. Khan, and J. R. Baker. 2005. Nanoparticle targeting of anticancer drug improves therapeutic response in animal model of human epithelial cancer. Cancer Res. 65:5317-5324.

9. Colvin, V. L. 2003. The potential environmental impact of engineered nanomaterials. Nat. Biotechnol. 21:1166-1170.

10. Oberdorster, E. 2004. Manufactured nanomaterials (Fullerenes, C-60) induce oxidative stress in the brain of juvenile largemouth bass. Environ. Health Perspect. 112:1058-1062.

11. Foley, S., C. Crowley, M. Smaihi, C. Bonfils, B. F. Erlanger, P. Seta, and C. Larroque. 2002. Cellular localisation of a water-soluble fullerene derivative. Biochem. Biophys. Res. Commun. 294:116-119.

12. Pernodet, N., X. H. Fang, Y. Sun, A. Bakhtina, A. Ramakrishnan, J. Sokolov, A. Ulman, and M. Rafailovich. 2006. Adverse effects of citrate/gold nanoparticles on human dermal fibroblasts. Small 2:766-773.

13. Pan, Y., S. Neuss, A. Leifert, M. Fischler, F. Wen, U. Simon, G. Schmid, W. Brandau, and W. Jahnen-Dechent. 2007. Size-dependent cytotoxicity of gold nanoparticles. Small 3:1941-1949.

14. Bernard, B. K., M. R. Osheroff, A. Hofmann, and J. H. Mennear. 1990. Toxicology and Carcinogenesis Studies of Dietary Titanium Dioxide-Coated Mica in Male and Female Fischer 344 Rats. J. Toxicol. Environ. Health 29:417-429.

15. Chen, J. L., and W. E. Fayerweather. 1988. Epidemiologic-Study of Workers Exposed to Titanium-Dioxide. J. Occup. Environ. Med. 30:937-942.

16. Hart, G. A., and T. W. Hesterberg. 1998. In vitro toxicity of respirable-size particles of diatomaceous earth and crystalline silica compared with asbestos and titanium dioxide. J. Occup. Environ. Med. 40:29-42.

17. Cho, M., H. Chung, W. Choi, and J. Yoon. 2004. Linear correlation between inactivation of E-coli and OH radical concentration in TiO2 photocatalytic disinfection. Water Res. 38:1069-1077.

18. Carp, O., C. L. Huisman, and A. Reller. 2004. Photoinduced reactivity of titanium dioxide. Prog. Solid State Chem. 32:33-177.

19. Dunford, R., A. Salinaro, L. Z. Cai, N. Serpone, S. Horikoshi, H. Hidaka, and J. Knowland. 1997. Chemical oxidation and DNA damage catalysed by inorganic sunscreen ingredients. FEBS Lett. 418:87-90.

20. Long, T. C., J. Tajuba, P. Sama, N. Saleh, C. Swartz, J. Parker, S. Hester, G. V. Lowry, and B. Veronesi. 2007. Nanosize titanium dioxide stimulates reactive oxygen species in brain microglia and damages neurons in vitro. Environ. Health Perspect. 115:1631-1637.

21. Ophus, E. M., L. Rode, B. Gylseth, D. G. Nicholson, and K. Saeed. 1979. Analysis of Titanium Pigments in Human-Lung Tissue. Scand. J. Work Environ. Health 5:290-296.

22. Lindenschmidt, R. C., K. E. Driscoll, M. A. Perkins, J. M. Higgins, J. K. Maurer, and K. A. Belfiore. 1990. The Comparison of a Fibrogenic and 2

Nonfibrogenic Dusts by Bronchoalveolar Lavage. Toxicol. Appl. Pharmacol. 102:268-281.

23. Oberdorster, G., J. Ferin, and B. E. Lehnert. 1994. Correlation between Particle-Size, in-Vivo Particle Persistence, and Lung Injury. Environ. Health Perspect. 102:173-179.

24. Sayes, C. M., R. Wahi, P. A. Kurian, Y. P. Liu, J. L. West, K. D. Ausman, D. B. Warheit, and V. L. Colvin. 2006. Correlating nanoscale titania structure with toxicity: A cytotoxicity and inflammatory response study with human dermal fibroblasts and human lung epithelial cells. Toxicol. Sci. 92:174-185.

25. Gurr, J. R., A. S. S. Wang, C. H. Chen, and K. Y. Jan. 2005. Ultrafine titanium dioxide particles in the absence of photoactivation can induce oxidative damage to human bronchial epithelial cells. Toxicology 213:66-73.

26. Lee, W. A., N. Pernodet, B. Q. Li, C. H. Lin, E. Hatchwell, and M. H. Rafailovich. 2007. Multicomponent polymer coating to block photocatalytic activity of TiO2 nanoparticles. Chem. Commun.:4815-4817.

27. Ghosh, K., Z. Pan, E. Guan, S. R. Ge, Y. J. Liu, T. Nakamura, X. D. Ren, M. Rafailovich, and R. A. F. Clark. 2007. Cell adaptation to a physiologically relevant ECM mimic with different viscoelastic properties. Biomaterials 28:671-679.

28. Eu, J. P., L. M. Liu, M. Zeng, and J. S. Stamler. 2000. An apoptotic model for nitrosative stress. Biochemistry 39:1040-1047.

29. Ghosh, K., X. D. Ren, X. Z. Shu, G. D. Prestwich, and R. A. F. Clark. 2006.

Fibronectin functional domains coupled to hyaluronan stimulate adult human dermal fibroblast responses critical for wound healing. Tissue Eng. 12:601-613.

30. Hidaka, H., S. Horikoshi, N. Serpone, and J. Knowland. 1997. In vitro photochemical damage to DNA, RNA and their bases by an inorganic sunscreen agent on exposure to UVA and UVB radiation. J. Photochem. Photobiol. A-Chem. 111:205-213.

5.6 Figure Captions

Figure 5. 1 Microscopy images of different types of TiO_2 particles used in this study. (A) SEM images of micro-sized clusters of rutile TiO_2 particles. (B) TEM images of rutile TiO_2 nanoparticles and particle size distribution. (C) SEM images of clusters of anatase TiO_2 particles with talc particles used as dispersant (inset: magnified image of an anatase cluster showing individual particles). (D) TEM images of anatase TiO_2 nanoparticles and particle size distribution.

Figure 5. 2 (A) Confocal images of human dermal fibroblasts incubated for 6 days with different concentrations of rutile TiO_2 nanoparticles. (B) Cell area and number as a function of nanoparticle concentrations.

Figure 5. 3 Cells were incubated with 0.4 mg/ml rutile TiO_2 nanoparticles for 2 days and then assayed for the following functions: (A) traction stresses exerted by cells on a hydrogel after 6 hours' incubation; (B) cell migration area out of an agarose droplet after 18 hours' incubation; (C) contraction of collagen gels after 4 hours' incubation.

Figure 5. 4 TEM images of cells incubated with 0.4 mg/ml rutile TiO_2 nanoparticles for 2 days. (A) A typical cell with nanoparticle clusters confined in vesicles. (B) Vesicles filled with nanoparticles (the red circle shows individual particles leaking out from the vesicles). (C) A vesicle with ruptured membrane (the dashed shows the

nuclear membrane and the arrow shows a small particle cluster lodged inside the nuclear membrane).

Figure 5. 5 A time sequence study of cells incubated with 0.4 mg/ml rutile TiO_2 nanoparticles. (A) TEM images, (B) vesicles size and particle cluster size, and (C) occupancy factor as a function of incubation time.

Figure 5. 6 (A) Confocal images of cells incubated with different concentrations of anatase TiO_2 nanoparticles for 3 days. (B) Cell number as a function of nanoparticle concentrations.

Figure 5. 7 Western blot results of actin from the same number of cells incubated with 0.4 mg/ml rutile or anatase TiO_2 nanopartilces for 2 days compared with those exposed to no particles or just talc particles at the same concentration.

Figure 5. 8 TEM images of cells incubated with 0.4 mg/ml anatase TiO_2 nanoparticles for 2 days. (A) Typical cells with huge holes induced by anatase particles. (B) most damage is distributed in the cytoplasm (left) and some vesiculated nuclei are also observed (right).

Figure 5. 9 Microscopy images of coated rutile TiO_2 particles. (A) SEM images, and (B) TEM images of coated rutile TiO_2 nanoparticles and particle size distribution.

Figure 5. 10 (A) Cell numbers after being incubated with different concentrations of coated TiO_2 nanoparticles for 11 days. (B) Hg lamp fluorescent images of cells incubated with coated TiO_2 nanoparticles.

Figure 5. 11 Flow cytometry results showing different particle uptake of cells after being incubated with 0.4 mg/ml rutile, anatase, and coated TiO_2 nanoparticles for 2 days. The phase contrast images of cells with attached particles were taken prior to the flow cytometry analysis.

Figure 5. 12 H_2O_2 generated and released by the cells incubated with 0.4 mg/ml rutile, anatase, and coated TiO_2 nanoparticles for 2 days compared with the control cells exposed to no particles.

5.7 Figures

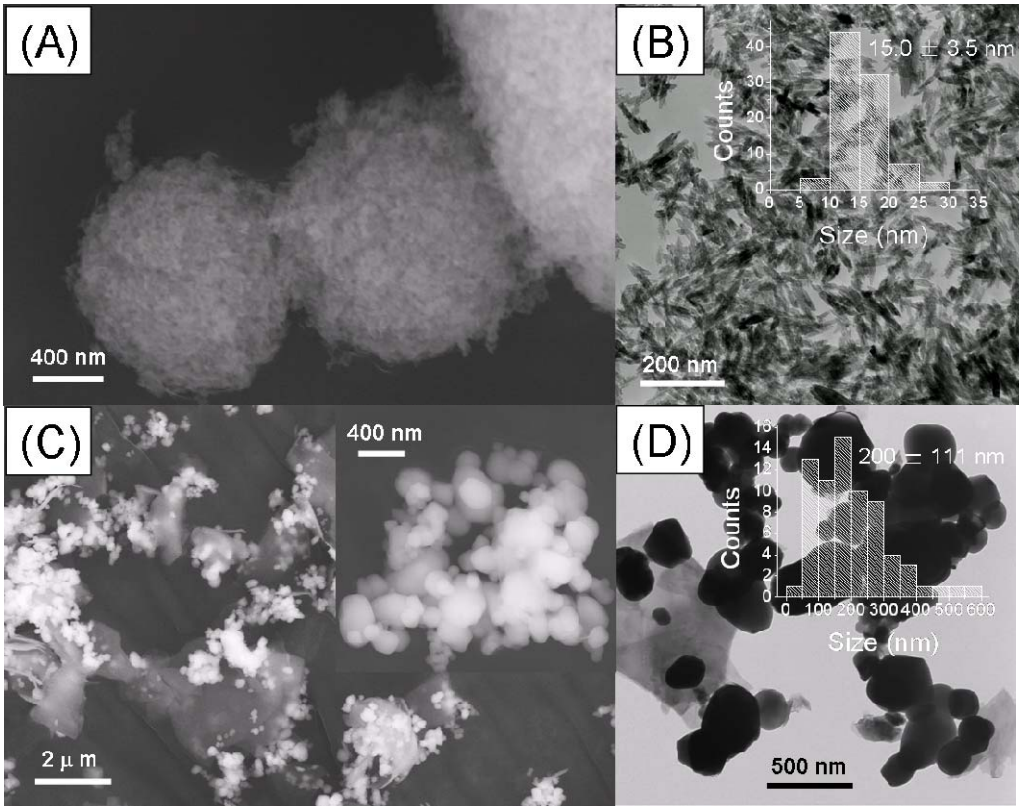

Figure 5.1

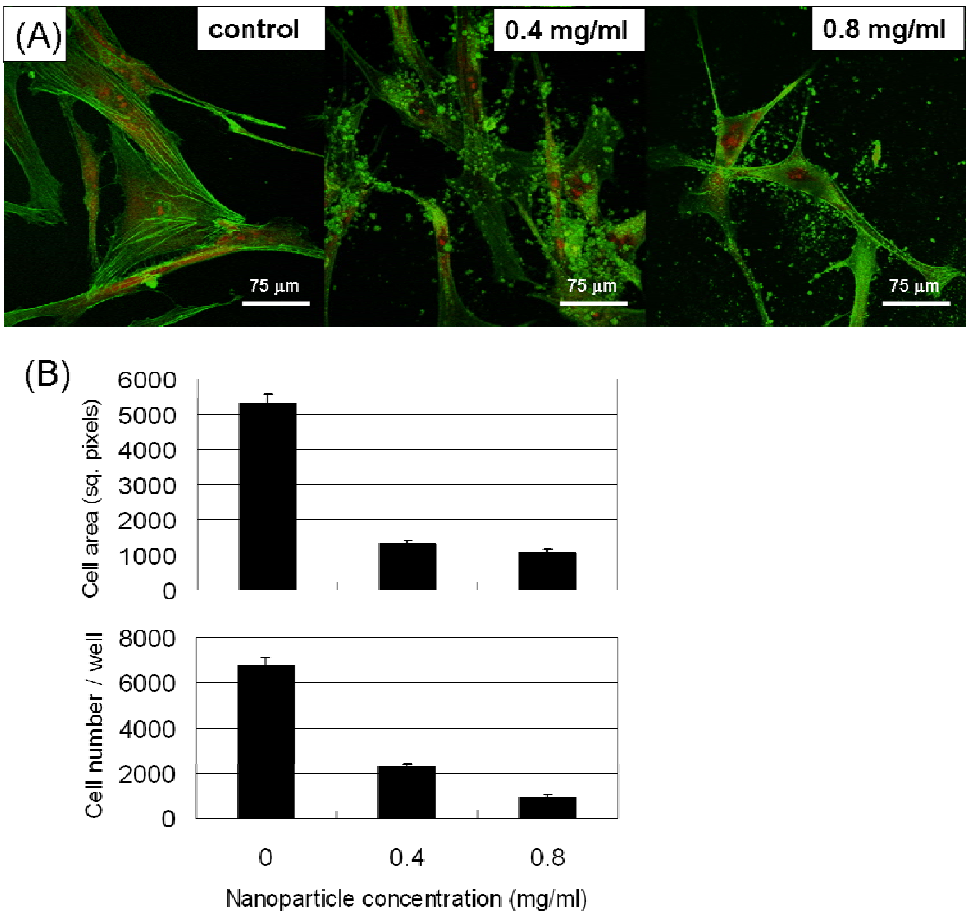
(A)
control
0.4 mg/ml
0.8 mg/ml
75 µm
75 µm
75 µm
(B)
Cell area (sq. pixels)
6000
5000
4000
3000
2000
1000
0
Cell number / well
8000
6000
4000
2000
0
0
0.4
0.8
Nanoparticle concentration (mg/ml)

Figure 5.2

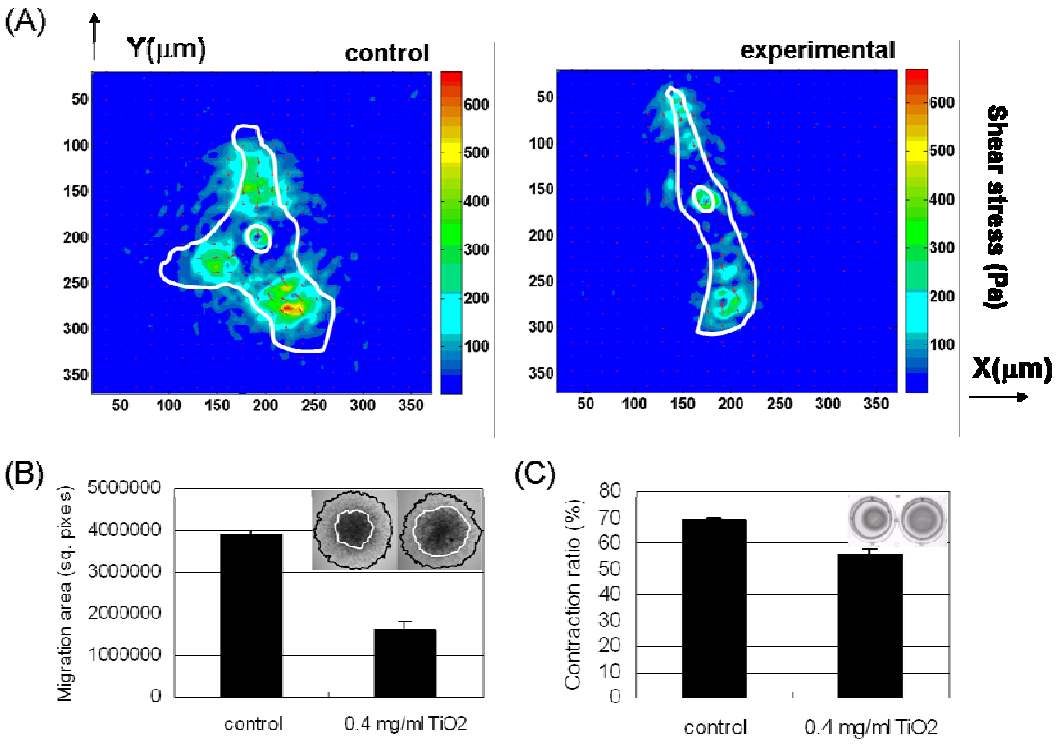
(A)
Y(μm)
control
experimental
Shear stress (Pa)
X(μm)
(B)
Migration area (sq. pixes)
control
0.4 mg/ml TiO2
(C)
Contraction ratio (%)
control
0.4 mg/ml TiO2

Figure 5.3

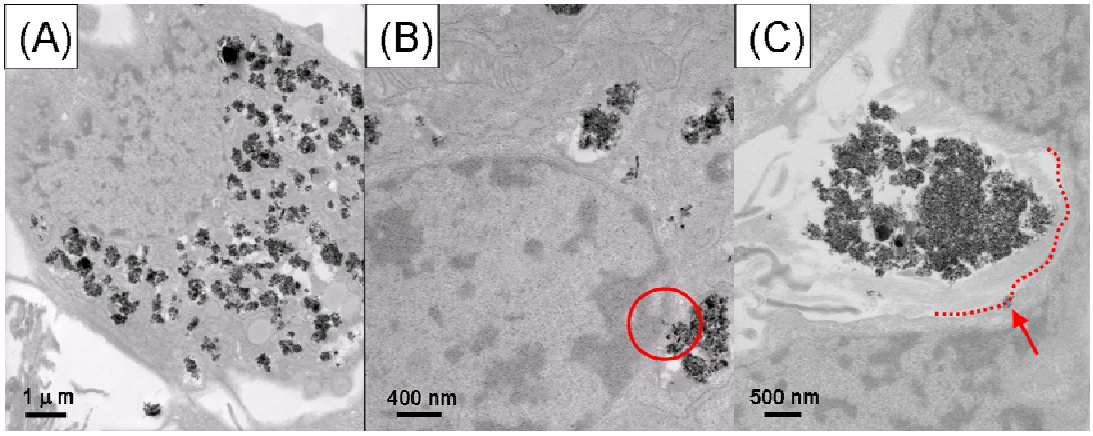

Figure 5.4

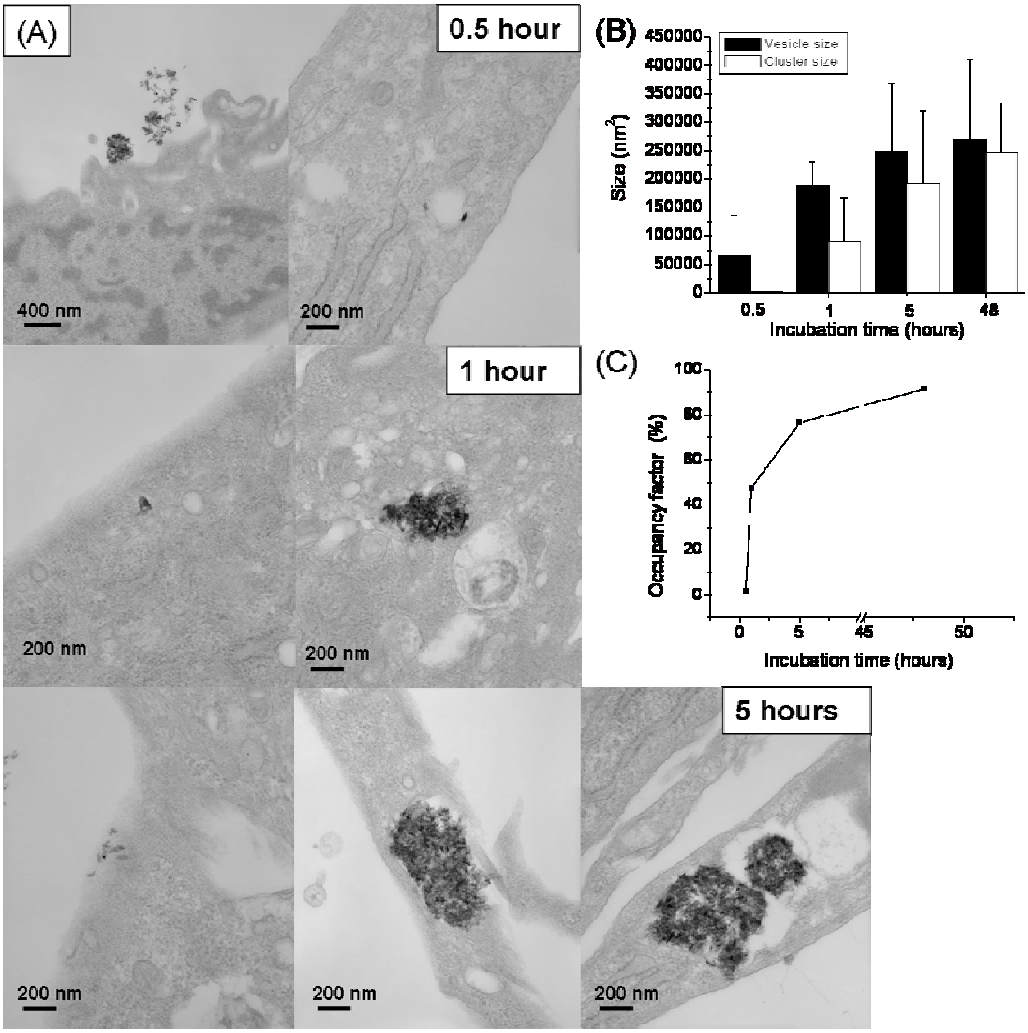
(A)
0.5 hour
400 nm
200 nm
(B)
Vesicle size
Cluster size
Size (nm²)
450000
400000
350000
300000
250000
200000
150000
100000
50000
0
0.5
1
5
48
Incubation time (hours)
1 hour
200 nm
200 nm
(C)
Occupancy factor (%)
100
80
60
40
20
0
0
5
45
50
Incubation time (hours)
5 hours
200 nm
200 nm
200 nm

Figure 5.5

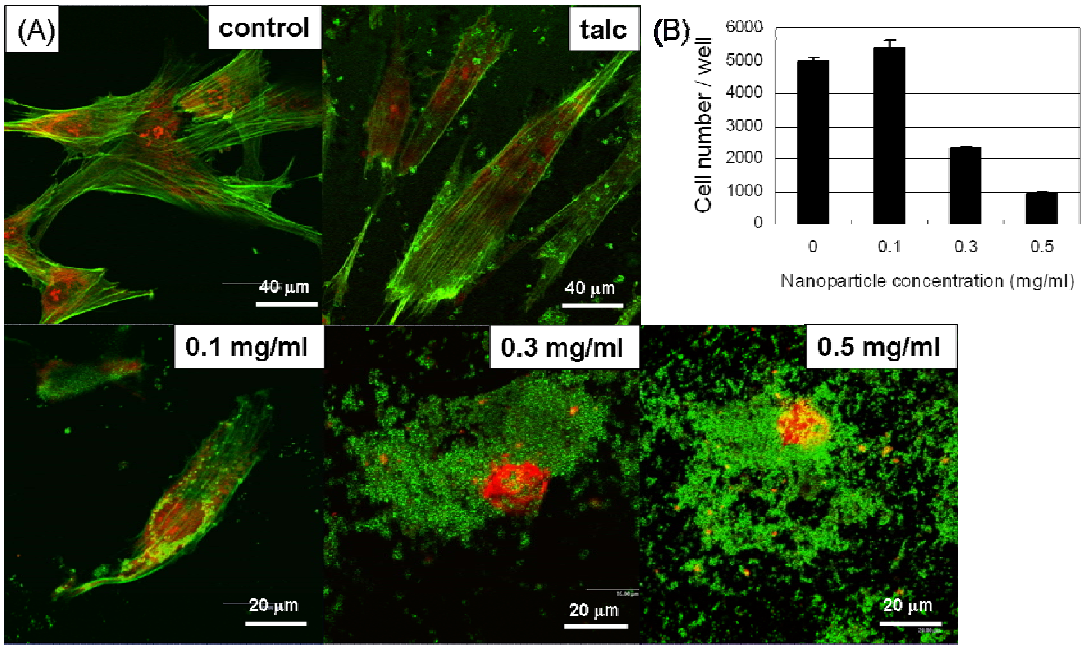
(A)
control
talc
40 μm
40 μm
0.1 mg/ml
0.3 mg/ml
0.5 mg/ml
20 μm
20 μm
20 μm
(B)
Cell number / well
6000
5000
4000
3000
2000
1000
0
0
0.1
0.3
0.5
Nanoparticle concentration (mg/ml)

Figure 5.6

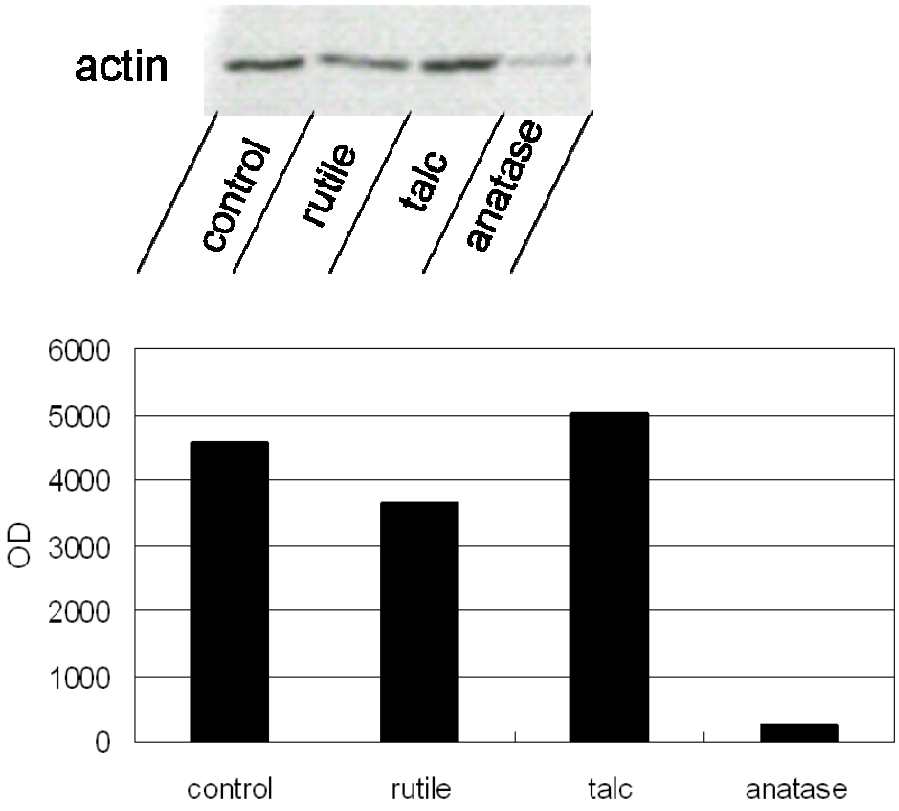
actin
control
rutile
talc
anatase
6000
5000
4000
3000
2000
1000
0
OD
control
rutile
talc
anatase

Figure 5.7

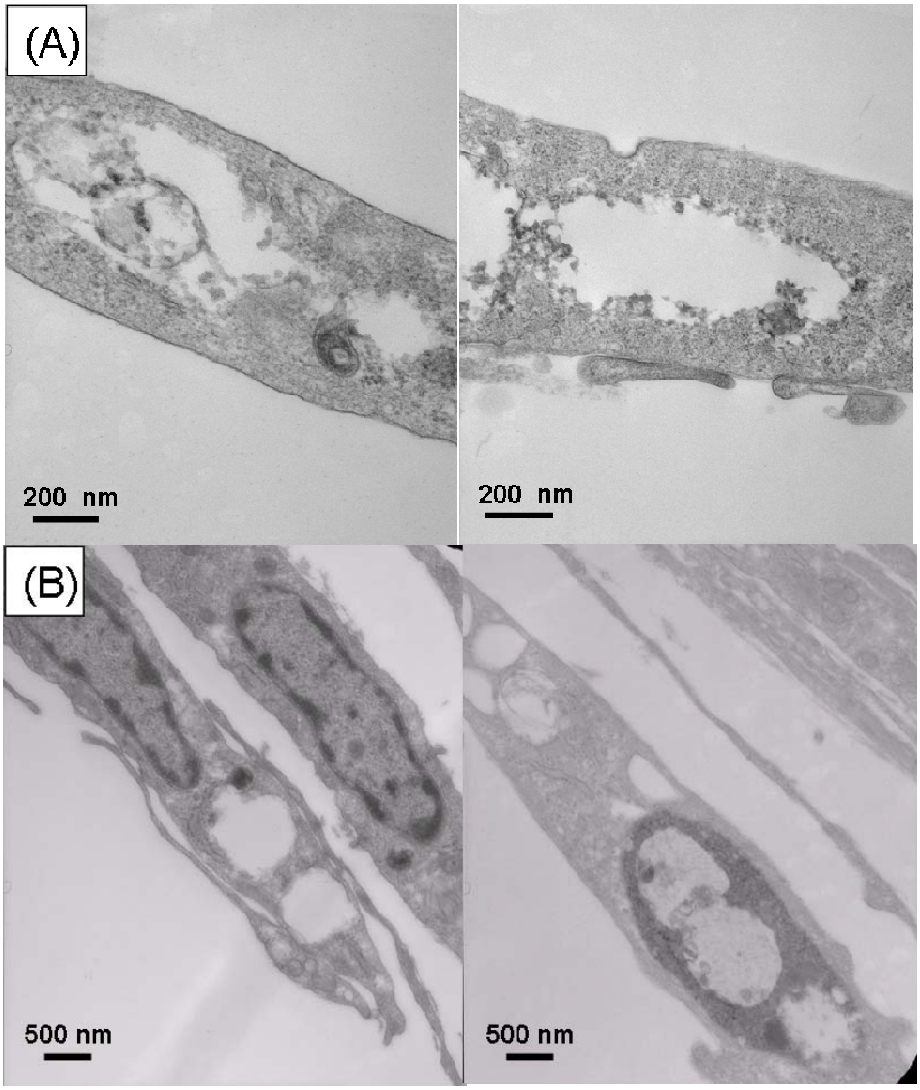

Figure 5.8

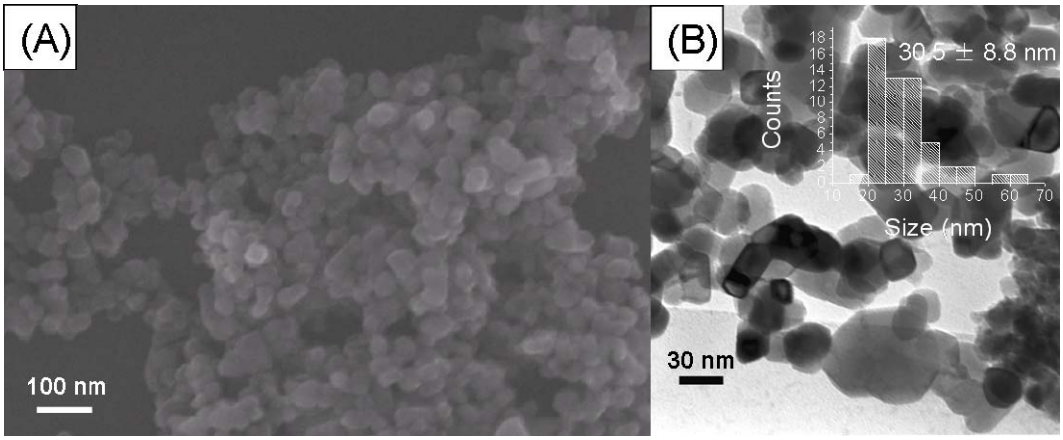

Figure 5.9

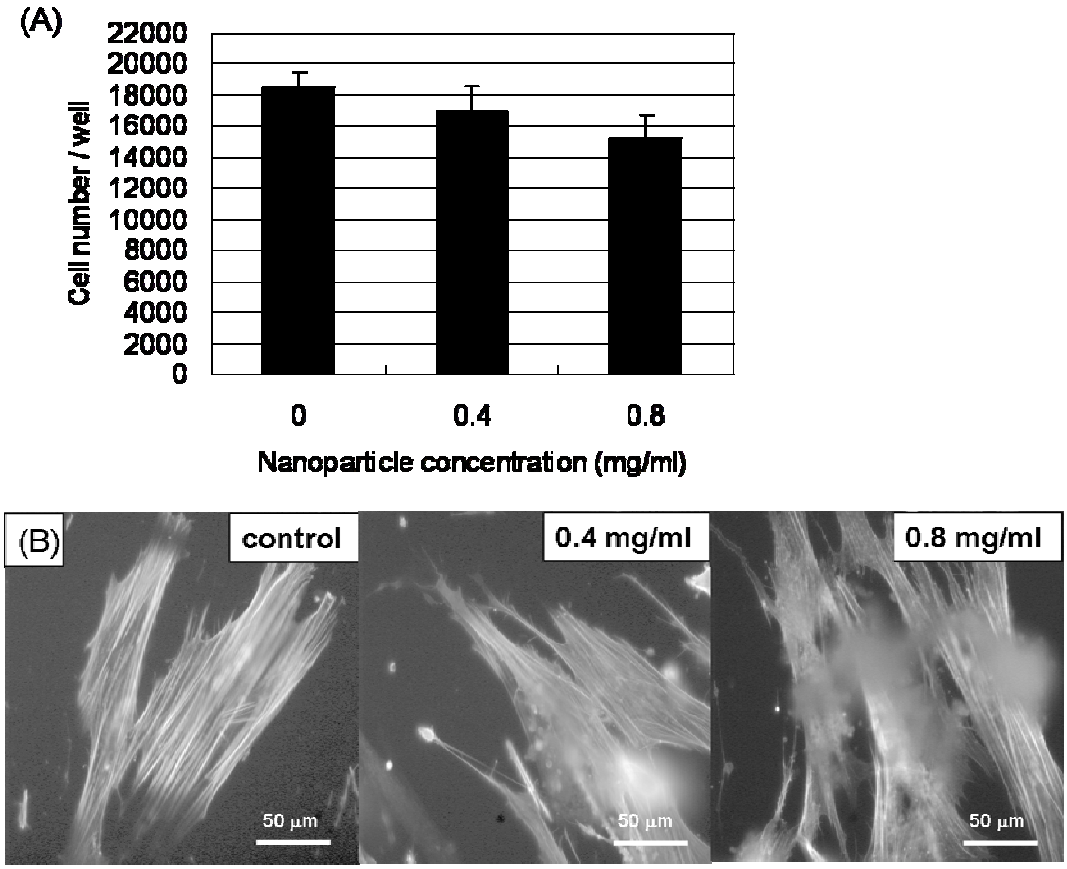
(A)
Cell number / well
22000
20000
18000
16000
14000
12000
10000
8000
6000
4000
2000
0
0
0.4
0.8
Nanoparticle concentration (mg/ml)
(B)
control
0.4 mg/ml
0.8 mg/ml
50 μm
50 μm
50 μm

Figure 5.10

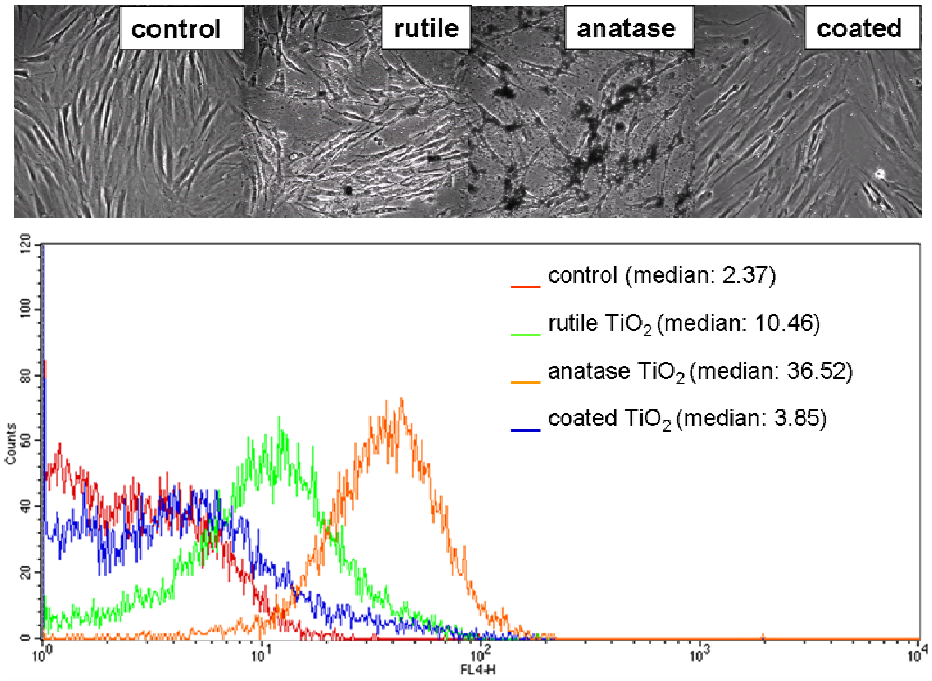
control
rutile
anatase
coated
control (median: 2.37)
rutile TiO2 (median: 10.46)
anatase TiO2 (median: 36.52)
coated TiO2 (median: 3.85)
Counts
FL4-H

Figure 5.11

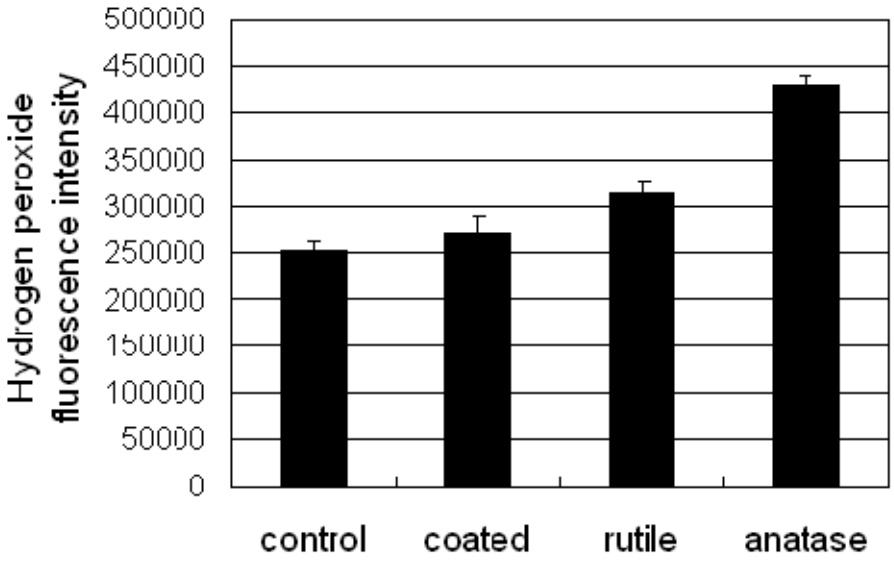
Hydrogen peroxide fluorescence intensity
500000
450000
400000
350000
300000
250000
200000
150000
100000
50000
0
control
coated
rutile
anatase

Figure 5.12

References

Chapter 1

1. Langer, R., and J. P. Vacanti. 1993. Tissue Engineering. Science 260:920-926.
2. Freed, L. E., G. Vunjaknovakovic, R. J. Biron, D. B. Eagles, D. C. Lesnoy, S. K. Barlow, and R. Langer. 1994. Biodegradable Polymer Scaffolds for Tissue Engineering. Bio-Technology 12:689-693.
3. Rosso, F., A. Giordano, M. Barbarisi, and A. Barbarisi. 2004. From cell-ECM interactions to tissue engineering. J. Cell. Physiol. 199:174-180.
4. Hubbell, J. A. 1995. Biomaterials in Tissue Engineering. Bio-Technology 13:565-576.
5. Lee, K. Y., and D. J. Mooney. 2001. Hydrogels for tissue engineering. Chem. Rev. 101:1869-1879.
6. Yang, S. F., K. F. Leong, Z. H. Du, and C. K. Chua. 2001. The design of scaffolds for use in tissue engineering. Part 1. Traditional factors. Tissue Eng. 7:679-689.
7. Yang, S. F., K. F. Leong, Z. H. Du, and C. K. Chua. 2002. The design of scaffolds for use in tissue engineering. Part II. Rapid prototyping techniques. Tissue Eng. 8:1-11.
8. Drury, J. L., and D. J. Mooney. 2003. Hydrogels for tissue engineering: scaffold design variables and applications. Biomaterials 24:4337-4351.
9. Shin, H., S. Jo, and A. G. Mikos. 2003. Biomimetic materials for tissue engineering. Biomaterials 24:4353-4364.

10. Lutolf, M. P., and J. A. Hubbell. 2005. Synthetic biomaterials as instructive extracellular microenvironments for morphogenesis in tissue engineering. Nat. Biotechnol. 23:47-55.

11. Pham, Q. P., U. Sharma, and A. G. Mikos. 2006. Electrospinning of polymeric nanofibers for tissue engineering applications: A review. Tissue Eng. 12:1197-1211.

12. Discher, D. E., P. Janmey, and Y. L. Wang. 2005. Tissue cells feel and respond to the stiffness of their substrate. Science 310:1139-1143.

13. Pelham, R. J., and Y. L. Wang. 1997. Cell locomotion and focal adhesions are regulated by substrate flexibility. Proc. Natl. Acad. Sci. U. S. A. 94:13661.

14. Balaban, N. Q., U. S. Schwarz, D. Riveline, P. Goichberg, G. Tzur, I. Sabanay, D. Mahalu, S. Safran, A. Bershadsky, L. Addadi, and B. Geiger. 2001. Force and focal adhesion assembly: a close relationship studied using elastic micropatterned substrates. Nat. Cell Biol. 3:466-472.

15. Wang, N., J. P. Butler, and D. E. Ingber. 1993. Mechanotransduction across the Cell-Surface and through the Cytoskeleton. Science 260:1124-1127.

16. Couchman, J. R., and A. Woods. 1999. Syndecan-4 and integrins: combinatorial signaling in cell adhesion. J. Cell Sci. 112:3415-3420.

17. Woods, A., R. L. Longley, S. Tumova, and J. R. Couchman. 2000. Syndecan-4 binding to the high affinity heparin-binding domain of fibronectin drives focal adhesion formation in fibroblasts. Arch. Biochem. Biophys. 374:66-72.

18. Engler, A., L. Bacakova, C. Newman, A. Hategan, M. Griffin, and D. Discher.

2004. Substrate compliance versus ligand density in cell on gel responses. Biophys. J. 86:617-628.

19. Georges, P. C., and P. A. Janmey. 2005. Cell type-specific response to growth on soft materials. Journal of Applied Physiology 98:1547-1553.

20. Engler, A. J., S. Sen, H. L. Sweeney, and D. E. Discher. 2006. Matrix elasticity directs stem cell lineage specification. Cell 126:677-689.

21. Galbraith, C. G., and M. P. Sheetz. 1998. Forces on adhesive contacts affect cell function. Curr. Opin. Cell Biol. 10:566-571.

22. Choquet, D., D. P. Felsenfeld, and M. P. Sheetz. 1997. Extracellular matrix rigidity causes strengthening of integrin-cytoskeleton linkages. Cell 88:39.

23. Ridley, A. J., M. A. Schwartz, K. Burridge, R. A. Firtel, M. H. Ginsberg, G. Borisy, J. T. Parsons, and A. R. Horwitz. 2003. Cell migration: Integrating signals from front to back. Science 302:1704-1709.

24. Wehrle-Haller, B., and B. A. Imhof. 2003. Actin, microtubules and focal adhesion dynamics during cell migration. Int. J. Biochem. Cell Biol. 35:39-50.

25. Sheetz, M. P., D. P. Felsenfeld, and C. G. Galbraith. 1998. Cell migration: Regulation of force on extracellular-matrix-integrin complexes. Trends Cell Biol. 8:51-54.

26. Alenghat, F. J., and D. E. Ingber. 2002. Mechanotransduction: All Signals Point to Cytoskeleton, Matrix, and Integrins. Science's STKE 119:pe6.

27. Elson, E. L., S. F. Felder, P. Y. Jay, M. S. Kolodney, and C. Pasternak. 1999. Forces in cell locomotion. In Cell Behaviour: Control and Mechanism of

Motility. Portland Press Ltd, London. 299-314.

28. Truskey, G. A., and J. S. Pirone. 1990. The Effect of Fluid Shear-Stress Upon Cell-Adhesion to Fibronectin-Treated Surfaces. J. Biomed. Mater. Res. 24:1333-1353.

29. Garcia, A. J., P. Ducheyne, and D. Boettiger. 1997. Quantification of cell adhesion using a spinning disc device and application to surface-reactive materials. Biomaterials 18:1091-1098.

30. Berk, D., and E. Evans. 1991. Detachment of Agglutinin-Bonded Red-Blood-Cells .3. Mechanical Analysis for Large Contact Areas. Biophys. J. 59:861-872.

31. Evans, E., D. Berk, and A. Leung. 1991. Detachment of Agglutinin-Bonded Red-Blood-Cells .1. Forces to Rupture Molecular-Point Attachments. Biophys. J. 59:838-848.

32. Evans, E., D. Berk, A. Leung, and N. Mohandas. 1991. Detachment of Agglutinin-Bonded Red-Blood-Cells .2. Mechanical Energies to Separate Large Contact Areas. Biophys. J. 59:849-860.

33. Knight, A. E., C. Veigel, C. Chambers, and J. E. Molloy. 2001. Analysis of single-molecule mechanical recordings: application to acto-myosin interactions. Prog. Biophys. Mol. Biol. 77:45-72.

34. Chesla, S. E., P. Selvaraj, and C. Zhu. 1998. Measuring two-dimensional receptor-ligand binding kinetics by micropipette. Biophys. J. 75:1553-1572.

35. Willemsen, O. H., M. M. E. Snel, A. Cambi, J. Greve, B. G. De Grooth, and C.

G. Figdor. 2000. Biomolecular interactions measured by atomic force microscopy. Biophys. J. 79:3267-3281.

36. Yip, C. M. 2001. Atomic force microscopy of macromolecular interactions. Curr. Opin. Struct. Biol. 11:567-572.

37. Ingber, D. E. 2003. Mechanosensation through integrins: Cells act locally but think globally. Proc. Natl. Acad. Sci. U. S. A. 100:1472.

38. Harris, A. K., P. Wild, and D. Stopak. 1980. Silicone-rubber substrata - New wrinkle in the study of cell locomotion. Science 208:177-179.

39. Dembo, M., T. Oliver, A. Ishihara, and K. Jacobson. 1996. Imaging the traction stresses exerted by locomoting cells with the elastic substratum method. Biophys. J. 70:2008-2022.

40. Oliver, T., K. Jacobson, and M. Dembo. 1998. Design and use of substrata to measure traction forces exerted by cultured cells. In Molecular Motors and the Cytoskeleton, Pt B. 497-521.

41. Dembo, M., and Y. L. Wang. 1999. Stresses at the cell-to-substrate interface during locomotion of fibroblasts. Biophys. J. 76:2307.

42. Oliver, T., M. Dembo, and K. Jacobson. 1999. Separation of propulsive and adhesive traction stresses in locomoting keratocytes. J. Cell Biol. 145:589-604.

43. Butler, J. P., I. M. Tolic-Norrelykke, B. Fabry, and J. J. Fredberg. 2002. Traction fields, moments, and strain energy that cells exert on their surroundings. Am. J. Physiol.-Cell Physiol. 282:C595.

44. Ghosh, K., Z. Pan, E. Guan, S. R. Ge, Y. J. Liu, T. Nakamura, X. D. Ren, M. Rafailovich, and R. A. F. Clark. 2007. Cell adaptation to a physiologically relevant ECM mimic with different viscoelastic properties. Biomaterials 28:671-679.

45. Guan, E., S. Smilow, M. Rafailovich, and J. Sokolov. 2004. Determining the mechanical properties of rat skin with digital image speckle correlation. Dermatology 208:112-119.

46. Ghosh, K., X. D. Ren, X. Z. Shu, G. D. Prestwich, and R. A. F. Clark. 2006. Fibronectin functional domains coupled to hyaluronan stimulate adult human dermal fibroblast responses critical for wound healing. Tissue Eng. 12:601-613.

47. Clark, R. A. F. 1996. The Molecular and Celluar Biology of Wound Repair. Plenum Press, New York.

48. Clark, R. A. F., K. Ghosh, and M. G. Tonnesen. 2007. Tissue engineering for cutaneous wounds. J. Invest. Dermatol. 127:1018-1029.

49. Clark, R. A. F., F. B. Lin, D. Greiling, J. Q. An, and J. R. Couchman. 2004. Fibroblast invasive migration into fibronectin/fibrin gels requires a previously uncharacterized dermatan sulfate-CD44 proteoglycan. J. Invest. Dermatol. 122:266-277.

50. Mitchison, T. J., and L. P. Cramer. 1996. Actin-based cell motility and cell locomotion. Cell 84:371-379.

51. Geiger, B., and A. Bershadsky. 2001. Assembly and mechanosensory function

of focal contacts. Curr. Opin. Cell Biol. 13:584-592.

52. Lauffenburger, D. A., and A. F. Horwitz. 1996. Cell migration: A physically integrated molecular process. Cell 84:359-369.

Chapter 2

1. Geiger, B., and A. Bershadsky. 2001. Assembly and mechanosensory function of focal contacts. Curr. Opin. Cell Biol. 13:584-592.

2. Schmidt, C. E., A. F. Horwitz, D. A. Lauffenburger, and M. P. Sheetz. 1993. Integrin cytoskeletal interactions in migrating fibroblasts are dynamic, asymmetric, and regulated. J. Cell Biol. 123:977-991.

3. Huttenlocher, A., M. H. Ginsberg, and A. F. Horwitz. 1996. Modulation of cell migration by integrin-mediated cytoskeletal linkages and ligand-binding affinity. J. Cell Biol. 134:1551-1562.

4. Palecek, S. P., J. C. Loftus, M. H. Ginsberg, D. A. Lauffenburger, and A. F. Horwitz. 1997. Integrin-ligand binding properties govern cell migration speed through cell-substratum adhesiveness. Nature 385:537-540.

5. Dimilla, P. A., K. Barbee, and D. A. Lauffenburger. 1991. Mathematical-Model for the Effects of Adhesion and Mechanics on Cell-Migration Speed. Biophys. J. 60:15-37.

6. Lo, C. M., H. B. Wang, M. Dembo, and Y. L. Wang. 2000. Cell movement is guided by the rigidity of the substrate. Biophys. J. 79:144-152.

7. Engler, A., L. Bacakova, C. Newman, A. Hategan, M. Griffin, and D. Discher.

2004. Substrate compliance versus ligand density in cell on gel responses. Biophys. J. 86:617-628.

8. Discher, D. E., P. Janmey, and Y. L. Wang. 2005. Tissue cells feel and respond to the stiffness of their substrate. Science 310:1139-1143.

9. Georges, P. C., and P. A. Janmey. 2005. Cell type-specific response to growth on soft materials. Journal of Applied Physiology 98:1547-1553.

10. Ghosh, K., X. D. Ren, X. Z. Shu, G. D. Prestwich, and R. A. F. Clark. 2006. Fibronectin functional domains coupled to hyaluronan stimulate adult human dermal fibroblast responses critical for wound healing. Tissue Eng. 12:601-613.

11. Greiling, D., and R. A. F. Clark. 1997. Fibronectin provides a conduit for fibroblast transmigration from collagenous stroma into fibrin clot provisional matrix. J. Cell Sci. 110:861-870.

12. Clark, R. A. F. The Molecular and Celluar Biology of Wound Repair. Plenum Press, New York and London.

13. Ghosh, K., Z. Pan, E. Guan, S. R. Ge, Y. J. Liu, T. Nakamura, X. D. Ren, M. Rafailovich, and R. A. F. Clark. 2007. Cell adaptation to a physiologically relevant ECM mimic with different viscoelastic properties. Biomaterials 28:671-679.

14. Ghosh, K., X. Z. Shu, R. Mou, J. Lombardi, G. D. Prestwich, M. H. Rafailovich, and R. A. F. Clark. 2005. Rheological characterization of in situ cross-linkable hyaluronan hydrogels. Biomacromolecules 6:2857-2865.

15. Wang, R. X., R. A. F. Clark, D. F. Mosher, and X. D. Ren. 2005. Fibronectin's central cell-binding domain supports focal adhesion formation and rho signal transduction. J. Biol. Chem. 280:28803-28810.

16. Clark, R. A. F., J. Q. An, D. Greiling, A. Khan, and J. E. Schwarzbauer. 2003. Fibroblast migration on fibronectin requires three distinct functional domains. J. Invest. Dermatol. 121:695-705.

17. Guan, E., S. Smilow, M. Rafailovich, and J. Sokolov. 2004. Determining the mechanical properties of rat skin with digital image speckle correlation. Dermatology 208:112-119.

18. Palecek, S. P., A. Huttenlocher, A. F. Horwitz, and D. A. Lauffenburger. 1998. Physical and biochemical regulation of integrin release during rear detachment of migrating cells. J. Cell Sci. 111:929-940.

19. Dembo, M., and Y. L. Wang. 1999. Stresses at the cell-to-substrate interface during locomotion of fibroblasts. Biophys. J. 76:2307.

20. Pelham, R. J., and Y. L. Wang. 1999. High resolution detection of mechanical forces exerted by locomoting fibroblasts on the substrate. Mol. Biol. Cell 10:935-945.

21. Harris, A. K., P. Wild, and D. Stopak. 1980. Silicone-rubber substrata - New wrinkle in the study of cell locomotion. Science 208:177-179.

22. Santas, A. J., J. A. Peterson, J. L. Halbleib, S. E. Craig, M. J. Humphries, and D. M. P. Peters. 2002. Alternative splicing of the IIICS domain in fibronectin governs the role of the heparin II domain in fibrillogenesis and cell spreading.

J. Biol. Chem. 277:13650-13658.

23. Mostafavi-Pour, Z., J. A. Askari, J. D. Whittard, and M. J. Humphries. 2001. Identification of a novel heparin-binding site in the alternatively spliced IIICS region of fibronectin: roles of integrins and proteoglycans in cell adhesion to fibronectin splice variants. Matrix Biol. 20:63-73.

Chapter 3

1. Lauffenburger, D. A., and A. F. Horwitz. 1996. Cell migration: A physically integrated molecular process. Cell 84:359-369.

2. Mitchison, T. J., and L. P. Cramer. 1996. Actin-based cell motility and cell locomotion. Cell 84:371-379.

3. Sheetz, M. P., D. P. Felsenfeld, and C. G. Galbraith. 1998. Cell migration: Regulation of force on extracellular-matrix-integrin complexes. Trends Cell Biol. 8:51-54.

4. Geiger, B., and A. Bershadsky. 2001. Assembly and mechanosensory function of focal contacts. Curr. Opin. Cell Biol. 13:584-592.

5. Smilenov, L. B., A. Mikhailov, R. J. Pelham, E. E. Marcantonio, and G. G. Gundersen. 1999. Focal adhesion motility revealed in stationary fibroblasts. Science 286:1172-1174.

6. Wehrle-Haller, B., and B. A. Imhof. 2003. Actin, microtubules and focal adhesion dynamics during cell migration. Int. J. Biochem. Cell Biol. 35:39-50.

7. Beningo, K. A., and Y. L. Wang. 2002. Flexible substrata for the detection of

cellular traction forces. Trends Cell Biol. 12:79-84.

8. Dembo, M., T. Oliver, A. Ishihara, and K. Jacobson. 1996. Imaging the traction stresses exerted by locomoting cells with the elastic substratum method. Biophys. J. 70:2008-2022.

9. Dembo, M., and Y. L. Wang. 1999. Stresses at the cell-to-substrate interface during locomotion of fibroblasts. Biophys. J. 76:2307.

10. Pelham, R. J., and Y. L. Wang. 1999. High resolution detection of mechanical forces exerted by locomoting fibroblasts on the substrate. Mol. Biol. Cell 10:935-945.

11. Tan, J. L., J. Tien, D. M. Pirone, D. S. Gray, K. Bhadriraju, and C. S. Chen. 2003. Cells lying on a bed of microneedles: An approach to isolate mechanical force. Proc. Natl. Acad. Sci. U. S. A. 100:1484-1489.

12. Buguin, A., P. Chavrier, B. Ladoux, O. du Roure, A. Saez, and P. Silberzan. 2005. An array of microfabricated pillars to study cell migration. M S-Med. Sci. 21:765-767.

13. Pelham, R. J., and Y. L. Wang. 1997. Cell locomotion and focal adhesions are regulated by substrate flexibility. Proc. Natl. Acad. Sci. U. S. A. 94:13661.

14. Munevar, S., Y. L. Wang, and M. Dembo. 2001. Distinct roles of frontal and rear cell-substrate adhesions in fibroblast migration. Mol. Biol. Cell 12:3947-3954.

15. du Roure, O., A. Saez, A. Buguin, R. H. Austin, P. Chavrier, P. Siberzan, and B. Ladoux. 2005. Force mapping in epithelial cell migration. Proc. Natl. Acad.

Sci. U. S. A. 102:2390-2395.

16. Harris, A. K., P. Wild, and D. Stopak. 1980. Silicone-rubber substrata - New wrinkle in the study of cell locomotion. Science 208:177-179.

17. Ghosh, K., Z. Pan, E. Guan, S. R. Ge, Y. J. Liu, T. Nakamura, X. D. Ren, M. Rafailovich, and R. A. F. Clark. 2007. Cell adaptation to a physiologically relevant ECM mimic with different viscoelastic properties. Biomaterials 28:671-679.

18. Ghosh, K., X. D. Ren, X. Z. Shu, G. D. Prestwich, and R. A. F. Clark. 2006. Fibronectin functional domains coupled to hyaluronan stimulate adult human dermal fibroblast responses critical for wound healing. Tissue Eng. 12:601-613.

19. Palecek, S. P., J. C. Loftus, M. H. Ginsberg, D. A. Lauffenburger, and A. F. Horwitz. 1997. Integrin-ligand binding properties govern cell migration speed through cell-substratum adhesiveness. Nature 385:537-540.

20. Engler, A., L. Bacakova, C. Newman, A. Hategan, M. Griffin, and D. Discher. 2004. Substrate compliance versus ligand density in cell on gel responses. Biophys. J. 86:617-628.

21. Ghosh, K., X. Z. Shu, R. Mou, J. Lombardi, G. D. Prestwich, M. H. Rafailovich, and R. A. F. Clark. 2005. Rheological characterization of in situ cross-linkable hyaluronan hydrogels. Biomacromolecules 6:2857-2865.

22. Clark, R. A. F., J. Q. An, D. Greiling, A. Khan, and J. E. Schwarzbauer. 2003. Fibroblast migration on fibronectin requires three distinct functional domains.

J. Invest. Dermatol. 121:695-705.

23. Guan, E., S. Smilow, M. Rafailovich, and J. Sokolov. 2004. Determining the mechanical properties of rat skin with digital image speckle correlation. Dermatology 208:112-119.

24. Munevar, S., Y. L. Wang, and M. Dembo. 2001. Traction force microscopy of migrating normal and H-ras transformed 3T3 fibroblasts. Biophys. J. 80:1744-1757.

25. Palecek, S. P., A. Huttenlocher, A. F. Horwitz, and D. A. Lauffenburger. 1998. Physical and biochemical regulation of integrin release during rear detachment of migrating cells. J. Cell Sci. 111:929-940.

26. Dahl, K. N., A. J. Engler, J. D. Pajerowski, and D. E. Discher. 2005. Power-law rheology of isolated nuclei with deformation mapping of nuclear substructures. Biophys. J. 89:2855-2864.

27. Ingber, D. E. 2003. Mechanosensation through integrins: Cells act locally but think globally. Proc. Natl. Acad. Sci. U. S. A. 100:1472.

28. Maniotis, A. J., C. S. Chen, and D. E. Ingber. 1997. Demonstration of mechanical connections between integrins cytoskeletal filaments, and nucleoplasm that stabilize nuclear structure. Proc. Natl. Acad. Sci. U. S. A. 94:849-854.

29. Ridley, A. J., M. A. Schwartz, K. Burridge, R. A. Firtel, M. H. Ginsberg, G. Borisy, J. T. Parsons, and A. R. Horwitz. 2003. Cell migration: Integrating signals from front to back. Science 302:1704-1709.

30. Ji, Y., K. Ghosh, X. Z. Shu, B. Q. Li, J. C. Sokolov, G. D. Prestwich, R. A. F. Clark, and M. H. Rafailovich. 2006. Electrospun three-dimensional hyaluronic acid nanofibrous scaffolds. Biomaterials 27:3782-3792.

Chapter 4

1. Palecek, S. P., J. C. Loftus, M. H. Ginsberg, D. A. Lauffenburger, and A. F. Horwitz. 1997. Integrin-ligand binding properties govern cell migration speed through cell-substratum adhesiveness. Nature 385:537-540.
2. Lo, C. M., H. B. Wang, M. Dembo, and Y. L. Wang. 2000. Cell movement is guided by the rigidity of the substrate. Biophys. J. 79:144-152.
3. Schmidt, C. E., A. F. Horwitz, D. A. Lauffenburger, and M. P. Sheetz. 1993. Integrin cytoskeletal interactions in migrating fibroblasts are dynamic, asymmetric, and regulated. J. Cell Biol. 123:977-991.
4. Lauffenburger, D. A., and A. F. Horwitz. 1996. Cell migration: A physically integrated molecular process. Cell 84:359-369.
5. Sheetz, M. P., D. P. Felsenfeld, and C. G. Galbraith. 1998. Cell migration: Regulation of force on extracellular-matrix-integrin complexes. Trends Cell Biol. 8:51-54.
6. Dembo, M., and Y. L. Wang. 1999. Stresses at the cell-to-substrate interface during locomotion of fibroblasts. Biophys. J. 76:2307.
7. Elson, E. L., S. F. Felder, P. Y. Jay, M. S. Kolodney, and C. Pasternak. 1999. Forces in cell locomotion. In Cell Behaviour: Control and Mechanism of

Motility. Portland Press Ltd, London. 299-314.

8. Clark, R. A. F. The Molecular and Celluar Biology of Wound Repair. Plenum Press, New York and London.

9. Wang, N., J. P. Butler, and D. E. Ingber. 1993. Mechanotransduction across the Cell-Surface and through the Cytoskeleton. Science 260:1124-1127.

10. Galbraith, C. G., and M. P. Sheetz. 1998. Forces on adhesive contacts affect cell function. Curr. Opin. Cell Biol. 10:566-571.

11. Balaban, N. Q., U. S. Schwarz, D. Riveline, P. Goichberg, G. Tzur, I. Sabanay, D. Mahalu, S. Safran, A. Bershadsky, L. Addadi, and B. Geiger. 2001. Force and focal adhesion assembly: a close relationship studied using elastic micropatterned substrates. Nat. Cell Biol. 3:466-472.

12. Ghosh, K., X. D. Ren, X. Z. Shu, G. D. Prestwich, and R. A. F. Clark. 2006. Fibronectin functional domains coupled to hyaluronan stimulate adult human dermal fibroblast responses critical for wound healing. Tissue Eng. 12:601-613.

13. Ghosh, K., X. Z. Shu, R. Mou, J. Lombardi, G. D. Prestwich, M. H. Rafailovich, and R. A. F. Clark. 2005. Rheological characterization of in situ cross-linkable hyaluronan hydrogels. Biomacromolecules 6:2857-2865.

14. Guan, E., S. Smilow, M. Rafailovich, and J. Sokolov. 2004. Determining the mechanical properties of rat skin with digital image speckle correlation. Dermatology 208:112-119.

15. Derycke, L. D. M., and M. E. Bracke. 2004. N-cadherin in the spotlight of

cell-cell adhesion, differentiation, embryogenesis, invasion and signalling. Int. J. Dev. Biol. 48:463-476.

16. Ko, K. S., P. D. Arora, V. Bhide, A. Chen, and C. A. G. McCulloch. 2001. Cell-cell adhesion in human fibroblasts requires calcium signaling. J. Cell Sci. 114:1155-1167.

17. Mary, S., S. Charrasse, M. Meriane, F. Comunale, P. Travo, A. Blangy, and C. Gauthier-Rouviere. 2002. Biogenesis of N-cadherin-dependent cell-cell contacts in living fibroblasts is a microtubule-dependent kinesin-driven mechanism. Mol. Biol. Cell 13:285-301.

18. Ganz, A., M. Lambert, A. Saez, P. Silberzan, A. Buguin, R. M. Mege, and B. Ladoux. 2006. Traction forces exerted through N-cadherin contacts. Biol. Cell 98:721-730.

19. MonierGavelle, F., and J. L. Duband. 1997. Cross talk between adhesion molecules: Control of N-cadherin activity by intracellular signals elicited by beta 1 and beta 3 integrins in migrating neural crest cells. J. Cell Biol. 137:1663-1681.

20. Goffin, J. M., P. Pittet, G. Csucs, J. W. Lussi, J. J. Meister, and B. Hinz. 2006. Focal adhesion size controls tension-dependent recruitment of alpha-smooth muscle actin to stress fibers. J. Cell Biol. 172:259-268.

Chapter 5

1. Ball, P. 2001. Roll up for the revolution. Nature 414:142-144.

2. Muldoon, L. L., M. Sandor, K. E. Pinkston, and E. A. Neuwelt. 2005. Imaging, distribution, and toxicity of superparamagnetic iron oxide magnetic resonance nanoparticles in the rat brain and intracerebral tumor. Neurosurgery 57:785-796.

3. Neuberger, T., B. Schopf, H. Hofmann, M. Hofmann, and B. von Rechenberg. 2005. Superparamagnetic nanoparticles for biomedical applications: Possibilities and limitations of a new drug delivery system. J. Magn. Magn. Mater. 293:483-496.

4. Kreuter, J. 1991. Nanoparticle-Based Drug Delivery Systems. J. Control. Release 16:169-176.

5. Jin, S., and K. M. Ye. 2007. Nanoparticle-mediated drug delivery and gene therapy. Biotechnol. Prog. 23:32-41.

6. Bellocq, N. C., S. H. Pun, G. S. Jensen, and M. E. Davis. 2003. Transferrin-containing, cyclodextrin polymer-based particles for tumor-targeted gene delivery. Bioconjugate Chem. 14:1122-1132.

7. Riboh, J. C., A. J. Haes, A. D. McFarland, C. R. Yonzon, and R. P. Van Duyne. 2003. A nanoscale optical biosensor: Real-time immunoassay in physiological buffer enabled by improved nanoparticle adhesion. J. Phys. Chem. B 107:1772-1780.

8. Kukowska-Latallo, J. F., K. A. Candido, Z. Y. Cao, S. S. Nigavekar, I. J. Majoros, T. P. Thomas, L. P. Balogh, M. K. Khan, and J. R. Baker. 2005. Nanoparticle targeting of anticancer drug improves therapeutic response in

animal model of human epithelial cancer. Cancer Res. 65:5317-5324.

9. Colvin, V. L. 2003. The potential environmental impact of engineered nanomaterials. Nat. Biotechnol. 21:1166-1170.

10. Oberdorster, E. 2004. Manufactured nanomaterials (Fullerenes, C-60) induce oxidative stress in the brain of juvenile largemouth bass. Environ. Health Perspect. 112:1058-1062.

11. Foley, S., C. Crowley, M. Smaihi, C. Bonfils, B. F. Erlanger, P. Seta, and C. Larroque. 2002. Cellular localisation of a water-soluble fullerene derivative. Biochem. Biophys. Res. Commun. 294:116-119.

12. Pernodet, N., X. H. Fang, Y. Sun, A. Bakhtina, A. Ramakrishnan, J. Sokolov, A. Ulman, and M. Rafailovich. 2006. Adverse effects of citrate/gold nanoparticles on human dermal fibroblasts. Small 2:766-773.

13. Pan, Y., S. Neuss, A. Leifert, M. Fischler, F. Wen, U. Simon, G. Schmid, W. Brandau, and W. Jahnen-Dechent. 2007. Size-dependent cytotoxicity of gold nanoparticles. Small 3:1941-1949.

14. Bernard, B. K., M. R. Osheroff, A. Hofmann, and J. H. Mennear. 1990. Toxicology and Carcinogenesis Studies of Dietary Titanium Dioxide-Coated Mica in Male and Female Fischer 344 Rats. J. Toxicol. Environ. Health 29:417-429.

15. Chen, J. L., and W. E. Fayerweather. 1988. Epidemiologic-Study of Workers Exposed to Titanium-Dioxide. J. Occup. Environ. Med. 30:937-942.

16. Hart, G. A., and T. W. Hesterberg. 1998. In vitro toxicity of respirable-size

particles of diatomaceous earth and crystalline silica compared with asbestos and titanium dioxide. J. Occup. Environ. Med. 40:29-42.

17. Cho, M., H. Chung, W. Choi, and J. Yoon. 2004. Linear correlation between inactivation of E-coli and OH radical concentration in TiO2 photocatalytic disinfection. Water Res. 38:1069-1077.

18. Carp, O., C. L. Huisman, and A. Reller. 2004. Photoinduced reactivity of titanium dioxide. Prog. Solid State Chem. 32:33-177.

19. Dunford, R., A. Salinaro, L. Z. Cai, N. Serpone, S. Horikoshi, H. Hidaka, and J. Knowland. 1997. Chemical oxidation and DNA damage catalysed by inorganic sunscreen ingredients. FEBS Lett. 418:87-90.

20. Long, T. C., J. Tajuba, P. Sama, N. Saleh, C. Swartz, J. Parker, S. Hester, G. V. Lowry, and B. Veronesi. 2007. Nanosize titanium dioxide stimulates reactive oxygen species in brain microglia and damages neurons in vitro. Environ. Health Perspect. 115:1631-1637.

21. Ophus, E. M., L. Rode, B. Gylseth, D. G. Nicholson, and K. Saeed. 1979. Analysis of Titanium Pigments in Human-Lung Tissue. Scand. J. Work Environ. Health 5:290-296.

22. Lindenschmidt, R. C., K. E. Driscoll, M. A. Perkins, J. M. Higgins, J. K. Maurer, and K. A. Belfiore. 1990. The Comparison of a Fibrogenic and 2 Nonfibrogenic Dusts by Bronchoalveolar Lavage. Toxicol. Appl. Pharmacol. 102:268-281.

23. Oberdorster, G., J. Ferin, and B. E. Lehnert. 1994. Correlation between

Particle-Size, in-Vivo Particle Persistence, and Lung Injury. Environ. Health Perspect. 102:173-179.

24. Sayes, C. M., R. Wahi, P. A. Kurian, Y. P. Liu, J. L. West, K. D. Ausman, D. B. Warheit, and V. L. Colvin. 2006. Correlating nanoscale titania structure with toxicity: A cytotoxicity and inflammatory response study with human dermal fibroblasts and human lung epithelial cells. Toxicol. Sci. 92:174-185.

25. Gurr, J. R., A. S. S. Wang, C. H. Chen, and K. Y. Jan. 2005. Ultrafine titanium dioxide particles in the absence of photoactivation can induce oxidative damage to human bronchial epithelial cells. Toxicology 213:66-73.

26. Lee, W. A., N. Pernodet, B. Q. Li, C. H. Lin, E. Hatchwell, and M. H. Rafailovich. 2007. Multicomponent polymer coating to block photocatalytic activity of TiO2 nanoparticles. Chem. Commun.:4815-4817.

27. Ghosh, K., Z. Pan, E. Guan, S. R. Ge, Y. J. Liu, T. Nakamura, X. D. Ren, M. Rafailovich, and R. A. F. Clark. 2007. Cell adaptation to a physiologically relevant ECM mimic with different viscoelastic properties. Biomaterials 28:671-679.

28. Eu, J. P., L. M. Liu, M. Zeng, and J. S. Stamler. 2000. An apoptotic model for nitrosative stress. Biochemistry 39:1040-1047.

29. Ghosh, K., X. D. Ren, X. Z. Shu, G. D. Prestwich, and R. A. F. Clark. 2006. Fibronectin functional domains coupled to hyaluronan stimulate adult human dermal fibroblast responses critical for wound healing. Tissue Eng. 12:601-613.

30. Hidaka, H., S. Horikoshi, N. Serpone, and J. Knowland. 1997. In vitro photochemical damage to DNA, RNA and their bases by an inorganic sunscreen agent on exposure to UVA and UVB radiation. J. Photochem. Photobiol. A-Chem. 111:205-213.